

On the Dynamics of Glassy Systems

by

Le Yan

A dissertation submitted in partial fulfillment

of the requirements for the degree of

Doctor of Philosophy

Department of Physics

New York University

September 2015

Matthieu Wyart

© Le Yan
All Rights Reserved, 2015

Dedication

To my mother.

Acknowledgements

First of all, I would like to thank my advisor, Matthieu Wyart, for his mentoring and guidance in science and in career. His deep insight into the physical world always enlightens me and leads to the right way to solve the scientific problems. I would like to thank Markus Müller, for his thoughtful direction in our collaboration on the spin glass project. I would like to thank my dissertation committee of Alexander Grosberg, David Pine, Paul Chaikin and Daniel Stein for their helpful suggestions on both science and career. I would also like to acknowledge all other principal investigators in the Center for Soft Matter Research at NYU, David Grier, Jasna Brujic, Marc Gershow and Alexandra Zidovska, for their discussions and comments that helped me make better science.

It was a great pleasure to work in the Center for Soft Matter Research, and I want to thank all current and former members for their support over the past four years. In particular, I want to thank, Gustavo Düring, Edan Lerner, Eric DeGiuli and Jie Lin in Wyart's group, Marco Baity-Jesi, Antoine Barizien and Alexis Front visited to the group, collaborations with whom are extremely pleasant and enthusiastic; Lang Feng, who introduced me to the Center; Payam Rowghanian, Jan Smrek, and Cato Sandford, who created a casual atmosphere in

the office room we shared and taught me a lot in language and culture; and Yin Zhang, Chen Wang, Wenhai Zheng, and Guolong Zhu, who continually “bothered” me with their research problems.

Last but not least, I am thankful to all my friends who helped me and encouraged me in my life at New York University, without whom I could not finish my Ph. D. study. Especially, I want to thank, Yanchao Xin, Hong Zhang, Shuang Li, and Yuqian Liu, who were my roommates and closest friends in New York; Tao Jiang, Lan Gong, and Hongliang Liu, who guided me as senior Ph. D. students; and Patrick Cooper, Daniel Foreman-Mackey, Victor Gorbenko, Shahab Kohani, Henrique Moyses, and Stefano Storace, who are my same-year fellows survived in the end.

Preface

Life is transient. What should we do in our limited time to make some differences? Some figures, like Euclid, are “alive” in people’s minds even after thousands of years, because their masterpieces keep inspiring and benefiting people. Knowledge of nature and ourselves is a wealth of all mankind, a contribution to which would surely make my life meaningful. That is my initial motivation for doing science.

Followed a typical education path, I became a Ph. D. student at New York University, standing at the gate to my research career dream and looking for questions that I could make use of my lifetime to work on. Fortunately, I met my second mentor (after my father as the first), Matthieu Wyart. He introduced me to the question of transients in nature – the dynamics of glassy systems.

“The flying arrow is motionless”, the famous paradox of ancient Greek philosopher Zeno, has a similar modern version in the physics of glasses: “the flowing liquid is solid”. Zeno’s paradox is deeply related to calculus and the concept of limit, nonetheless, the physics lying behind the glass connects to a long dynamical time scale. Below the time scale, a glass appears to be static and solid, while above, it flows as a sticky liquid, like honey. It is also a physical phenomenon closely related to life. Imagine you are stuck in a traffic jam: if you are in a hurry, staring at the second hand on your watch, you may probably curse the jammed traffic; but if you are relaxed, enjoying the music and the views, you may happily drive to your destination after momentary waitings. These dynamical systems characterized by long time scales are glassy systems.

In glassy materials, the dynamical time scale can be tuned by temperature and driving forces like gravity. For example, the wax flows more and more easily if one heats it up; the sandpile slides faster and faster when the bed of the dump truck is tilted more and more steeply. However, how the time scale depends on temperature and driving force may vary from system to system, and there are not yet universal rules like Newton's Laws to describe different dynamics. We are curious to know what determines the dynamical properties of the glassy systems from microscopic level; Is there any dynamical universality among systems that possess certain microscopic features? One prominent concept of dynamical systems is self-organization: the trend that the system spontaneously evolves to states where the dynamical time scale diverges. So the dynamical transitions are usually relevant in glassy systems. The dynamics in this situation become rich: phenomena of all different time scales accompanied with different sizes appear. For example, in the Earth crust as a glassy system, earthquakes varying in intensity from unnoticeable to devastating can happen. But how our nature spontaneously evolves to these critical states is still lack of a mathematical description.

I have studied these general questions in specific systems and models during my Ph. D. and conclude them in this dissertation. The dissertation may never be eternal, but to me, it is a first small but important step towards my scientific career, which, I hope, will leave some valuable thoughts that continually inspire and benefit others.

Abstract

Glassy systems are disordered systems characterized by extremely slow dynamics. Examples are supercooled liquids, whose dynamics slow down under cooling. The specific pattern of slowing-down depends on the material considered. This dependence is poorly understood, in particular, it remains generally unclear which aspects of the microscopic structures control the dynamics and other macroscopic properties. Attacking this question is one of the two main aspects of this dissertation. We have introduced a new class of models of supercooled liquids, which captures the central aspects of the correspondence between structure and elasticity on the one hand, the correlation of structure and thermodynamic and dynamic properties on the other. These models can also be resolved analytically, leading to theoretical insights into the question. Our results also shed new light on the temperature-dependence of the topology of covalent networks, in particular, on the rigidity transition that occurs when the valence is increased. Observations suggested the presence of a nearly critical range in the proximity of the rigidity threshold. Our work rules out the predominant explanation for this phenomenon by a “rigidity window” where the rigidity is barely satisfied.

Other questions appear in glassy systems at zero temperature, when the thermal activation time is infinitely long. In that situation, a glassy system can flow if an external driving force is imposed above some threshold. Near the threshold, the dynamics are critical. To describe the critical dynamics, one must understand how the system self-organizes into specific configurations.

The first example we will consider is the erosion of a river bed. Grains or pebbles are pushed by a fluid and roll on a disordered landscape made of the

static particles. Experiments support the existence of a threshold forcing, below which no erosion flux is observed. Near the threshold, the transient state takes very long and the flux converges very slowly toward its stationary value. In the field, this long transient state is called “armoring” and corresponds to the filling up of holes on the frozen landscape by moving particles. The dynamics near the threshold are relevant for geophysical applications – gravel river beds tend to spontaneously sit at the threshold where erosion stops, but are poorly understood. In this dissertation, we present a novel microscopic model to describe the erosion near threshold. This model makes new quantitative predictions for the erosion flux *vs* the applied forcing and predicts that the spatial repartition of the flux is highly non-trivial: it is power-law distributed in space with long range correlation in the flux direction, but no correlations in the perpendicular directions. We introduce a mean-field model to capture analytically some of these properties.

To study further the self-organization of driven glassy systems, we investigate, as our last example, the athermal dynamics of mean-field spin glasses. Like many of other glasses, such as electron glasses, random close packings, etc., the spin glass self-organizes into the configurations that are stable, but barely so. Such marginal stability appears with the presence of a pseudogap in soft excitations – a density of states vanishing as a power-law distribution at zero energy. How such pseudogaps appear dynamically as the systems are prepared and driven was not understood theoretically. We elucidate this question, by introducing a stochastic process mimicking the dynamics, and show that the emergence of a pseudogap is deeply related to very strong anti-correlations emerging among soft excitations.

Contents

Dedication	iv
Acknowledgements	v
Preface	vii
Abstract	ix
List of Figures	xiv
List of Appendices	xxvii
1 Introduction	1
1.1 Dynamics under cooling – glass transition	4
1.2 Rigidity of a structure	8
1.3 Non-equilibrium dynamical phase transition	15
1.4 Critical dynamics	19
1.5 Structure of the dissertation	23
2 Why glass elasticity affects the thermodynamics and fragility of super-cooled liquids	25

2.1	Introduction	26
2.2	Random Elastic Network Model	29
2.3	Numerical Results of the Model	33
2.4	Theory on Thermodynamics of the Model	39
2.5	Discussion	45
3	Evolution of Covalent Networks under Cooling: Contrasting the Rigidity Window and Jamming Scenarios	47
3.1	Introduction	48
3.2	Adaptive Elastic Network Model	50
3.3	Numerical Proofs of the Mean-field Rigidity Transition	53
3.4	A Simple Argument for the Mean-field Scenario	58
4	Adaptive Elastic Networks as Models of Supercooled Liquids	61
4.1	Introduction	62
4.2	Adaptive Network Model	66
4.3	Numerical Results of the Model	70
4.4	Theory of Thermodynamics	76
4.5	Conclusions	84
5	A Model for the Erosion Onset of a Granular Bed Sheared by a Viscous Fluid	86
5.1	Introduction	87
5.2	Erosion Model	89
5.3	Numerical Results on Dynamics of the Model	92
5.4	An Argument on the Scaling Relation	97
5.5	Mean-field Model on the Distribution of Local Currents	98

5.6	Potential Experimental Tests	99
6	Dynamics and Correlations among Soft Excitations in Marginally Stable Glasses	101
6.1	Introduction	102
6.2	Dynamics of Sherrington-Kirkpatrick Model	104
6.3	Multi-spin Stability Criterion	106
6.4	Fokker-Planck Description of the Dynamics	109
6.5	Emergence of Correlations	111
6.6	Conclusion	114
7	Outlooks	115
7.1	Intermediate Phase	115
7.2	Dynamical Transition at Finite Temperature	118
7.3	Universality of Critical Dynamics	120
8	Conclusion	125
	Appendices	128
	Bibliography	164

List of Figures

1.1	A phase diagram of static and dynamic phases of glassy systems. T is the temperature, f is the driving force.	2
1.2	Scatter plot of the jump of specific heat $\Delta C_p/\Delta S_m$ and the fragility m of different glassy materials. The dashed line is given by $m = 40\Delta C_p/\Delta S_m$, where ΔS_m is the entropy gain in melting of the same material. The plot is reproduced from Reference [5].	5
1.3	Scatter plot of boson peak intensity ratio R_1 and fragility m of different glasses. The plot is reproduced from Reference [33].	7
1.4	The fragility m (Left) and the jump of specific heat Δc_p (Right) of chalcogenides with coordination number r . The plots are reproduced from References [4, 35].	7
1.5	An illustration of the rigidity transition of a network by adding pairwise constraints from floppy (Left) to isostatic (Middle) and to self-stressed (Right).	9
1.6	Zoom-in illustration of a spring network with a spring of stiffness $k_{\langle i,j \rangle}$ connecting particle i and j	11

1.7	Particle trajectories (top view) of a granular bed erosion driven by water flow. The water is injected from the left to right, as indicated by the blue arrow. The plot is reproduced from Reference [83].	16
1.8	Pseudogap in distribution of local stabilities in various glassy systems. (a) Density of states $P(E)$ in Coulomb glasses, where the gap is centered at the Fermi level; (b) Distribution of local fields $P(\lambda)$ in spin glasses; (c) Distribution of contact forces $p(f)$ and (d) distribution of contact gaps $g(h)$ in packings of hard spheres. The plots are reproduced from References [104, 109, 112].	21
1.9	Illustration of the evolution of a dynamical system from unstable states to the margin of the stable states in the phase space. A and B are arbitrary coordinates of the phase space. The plot is reproduced from Reference [101].	23
2.1	Top row: sketches of covalent networks with different mean valence r around the valence r_c : red solid lines represent covalent bonds; cyan dash lines represent van der Waals interactions. Bottom: sketch of our elastic network model with varying coordination number z (defined as the average number of strong springs in red) around Maxwell threshold z_c ; cyan springs have a much weaker stiffness, and model weak interactions.	30

2.2	Specific heat $c(T)$ <i>v.s.</i> rescaled temperature T/T_g for various excess coordination $\delta z \equiv z - z_c$ as indicated in legend, for $\alpha = 3 \times 10^{-4}$ and $d = 2$. $c(T)$ displays a jump at the glass transition. Solid lines are theoretical predictions, deprived of any fitting parameters, of our mean-field approximation. They terminate at the Kautzman temperature T_K . Inset: glass transition temperature T_g <i>vs</i> δz for several amplitude of weak interactions α , as indicated in legend.	35
2.3	Jump of specific heat Δc versus excess coordination δz in $d = 2$ for different strength of weak springs α , as indicated in legend. Solid lines are mean-field predictions not enforcing the orthogonality of the $ \delta r_p\rangle$, dashed-line corresponds to the ROM where orthogonality is enforced. In both cases the specific heat is computed at the numerically obtained temperature T_g . Inset: theoretical predictions for Δc <i>vs</i> δz computed at the theoretical temperature T_K	36
2.4	Fragility m versus excess coordination δz for different strength of weak interactions α as indicated in legend, in $d = 2$. Dash dot lines are guide to the eyes, and reveal the non-monotonic behavior of m near the rigidity transition. Inset: Angell plot representing $\log \tau$ <i>v.s.</i> inverse temperature T_g/T for different δz and $\alpha = 3 \times 10^{-4}$	38
2.5	Left: Inverse boson peak amplitude R_1 versus excess coordination δz in our $d = 3$ elastic network model, for different weak interaction strenghts as indicated in legend. Dash dot lines are drawn to guide one's eyes. Right: Inverse boson peak amplitude R_1 versus fragility m for different weak springs α	41

3.1	<p>Three distinct scenarios for the rigidity transition in chalcogenide glasses. Bonds in blue, green, red corresponds respectively to floppy (under-constrained), isostatic (marginally-constrained) and over-constrained regions. $p(z)$ is the probability that a rigid cluster (made of green and red bonds) percolates, as a function of the valence z. (a) Rigidity percolation model where bonds are randomly deposited on a lattice. Percolation occurs suddenly and $p(z)$ jumps from 0 to 1 at $z_{cen} < z_c$. At z_{cen}, the rigid network is fractal. (b) The self-organizing network model at zero temperature. Over-constrained regions are penalized energetically and are absent for $z < z_z$. For $z \in [z_{iso}, z_c]$, $0 < p(z) < 1$ even in the thermodynamic limit. (c) Mean-field scenario, where $p(z)$ jumps from 0 to 1 at z_c, and where the rigid cluster at z_c is not fractal.</p>	51
3.2	<p>Illustration of our model. The triangular lattice is slightly distorted as shown in the inset of (a), and weak springs connecting all second neighbors are present, as shown in blue in the inset of (b). Our Monte-Carlo considers the motion of strong springs such as that leading from (a) to (b).</p>	52
3.3	<p>P_∞ vs $(z - z_c)N^{1/d\nu}$ in the <i>weak-force</i> condition (a) and for $T = \infty$ (b). p vs $\delta z \equiv z - z_c$ in the <i>weak-force</i> (c) and <i>strong-force</i> (d) conditions. The black squares are extrapolations of the finite N spline curves, as detailed in the main text. In (c), the gray line is a step function at $z = z_c$, whereas in (d) it corresponds to the result of [75].</p>	54

3.4	$D(\omega)$ at $z - z_c = -0.05$ and various T indicated in legend for (a) $\alpha = 0$ and (b) $\alpha = 0.0003$. Gray dashed lines are numerical solution of mean-field networks generated in [130]. (c) Boson peak frequency ω^* vs coordination z for the <i>weak-interaction</i> regime. ω^* is defined as the peak frequency of $D(\omega)/\omega^{d-1}$, a quantity shown in (d).	56
3.5	Shear modulus of the strong network G vs $\delta z \equiv z - z_c$ for parameters indicated in legend. The total shear modulus G_{tot} including the effect of weak springs is represented for the <i>weak-interaction regime</i> . Inset: same plot in log-log scale, the horizontal axis is $z - z_c$ for low-temperatures conditions (blue and green), and $z - z_{cen}$ at $T = \infty$ (red).	57
4.1	Illustration of rigidity transition. Blue, green, and red color the floppy, isostatic, and stressed clusters, respectively.	64

- 4.2 (Color online) (a) and (b) Illustration of the frozen network model [116]; (c) and (d) illustrate the adaptive network model [117]. In the latter case, the triangular lattice is systematically distorted in a unit cell of four nodes shown in the inset of (c). We group nodes by four, labeled as, A, B, C, and D in Fig. 4.2. One group forms the unit cell of the crystalline lattice. Each cell is distorted identically in the following way: node A stays, while nodes B, C, and D move by a distance δ , B along the direction perpendicular to BC, C along the direction perpendicular to CD, and D along the direction perpendicular to DB. δ is set to 0.2 with the lattice constant as unity. Weak springs connecting (b) six nearest neighbors without strong springs and (d) six next-nearest-neighbors are indicated in straight cyan lines, emphasized for the central node. (c) Illustration of an allowed step, where the strong spring in red relocates to a vacant edge indicated by a dashed blue line. 67
- 4.3 (Color online) Illustration of configuration energy of the adaptive network model ($\delta z = 0.27$). Solid lines are springs, colored according to their extensions: from red to purple, the springs go from being stretched to being compressed, with spring extensions shown in the unit of ϵ . Left: Nodes sit at lattice sites, so the color shows the rest length mismatches of the springs $\{\epsilon_\gamma\}$. Right: Nodes are relaxed to mechanical equilibrium. Most links appear in green, indicating that most of the elastic energy is released. The configuration energy is defined by the residual energy. . . 68
- 4.4 (Color online) Relaxation time τ in log-scale versus inverse temperature $1/T$ for different coordination numbers δz and $\alpha = 0.0003$. The solid black line indicates a power law relation between τ and T : $\tau \sim T^{-1/2}$. . . 71

4.5	(Color online) Left: Shear modulus of adaptive networks at temperature T rescaled by G at $T = \infty$ $G(z, T)/G(z, \infty)$, $\alpha = 0.0003$. The temperature T is rescaled by T_g . Right: Correlation between transition temperature T_g and shear modulus G in the frozen network model [116].	72
4.6	(Color online) Thermodynamics of the adaptive network model without weak constraints $\alpha = 0$. (a) Energy E/N_s vs. temperature; (b) specific heat C/N_s vs. temperature; (c) excess number density of redundant constraints n_{ex} extracted using the pebble game algorithm vs. temperature. Symbols are numerical data; solid lines are theoretic predictions.	74
4.7	(Color online) Top: Specific heat $c(z, T)$ vs scaled temperature T/T_g for networks with average coordination numbers near and away from the isostatic on both floppy and rigid sides. The strength of the weak constraints is given by $\alpha = 0.0003$. Bottom: Specific heat at temperature T_g , $c(z, T_g)$, vs coordination number δz for $\alpha = 0, 0.0003, 0.003, 0.03$. The inset shows the transition temperature T_g for different z and α . Symbols are numerical results, and lines are theoretical predictions: dashed lines are for frozen network model and solid lines are for the new model derived in section IV.	75
4.8	(Color online) Theoretical predictions for the jump of specific heat. For vanishingly weak springs $\alpha \rightarrow 0$, it is predicted that the jump is essentially constant for $z < z_c$ and then drops to zero a z_c . For larger z , it behaves as $z - z_c$. As α grows this sharp curve becomes smooth, but a minimum is still present near $z = z_c$	77

4.9	(Color online) (a) $z < z_c$, localized redundant constraints (red) in a floppy sea (blue); (b) $z > z_c$ localized floppy modes (blue) in a rigid sea (red and green).	79
4.10	(Color online) Left: Excess number density of redundant constraints $n_{\text{ex}}(z, \beta)$. Right: Fluctuation of the number density of redundant constraints $(\Delta n_r)^2$. The solid black lines show the predictions from the approximate entropy Eq.(4.9).	81
5.1	Illustration of the model. Small circles indicate lattice sites, particles are represented by discs in yellow, or green if motion occurred between t (left) and $t+1$ (right). The black arrow is in the downhill direction. Solid lines indicate outlet with positive forces. If a particle has two outlets with positive forces, the larger (smaller) one is colored in red (blue).	91
5.2	Average current J versus $\theta - \theta_c$ in log-log scale for the (a) “equilibrated” and (b) “quenched” protocols, for which $\theta_c = 0.164 \pm 0.002$ and $\theta_c = 0.172 \pm 0.002$ respectively- a difference plausibly due to finite size effects. The black solid lines with slope one indicate the linear relation $J \propto \theta - \theta_c$. (c) Density of conducting sites ρ_s versus $\theta - \theta_c$ for the “equilibrated” protocol. (d) ρ_s curves collapsed by rescaling $\theta - \theta_c$ with $L^{1/\nu}$, where $\nu = 3.0 \pm 0.2$	92
5.3	Left: Transient time t_{conv} <i>v.s.</i> θ . For a given realization, t_{conv} is defined as the smallest time for which $J(t) - J \leq \sqrt{\text{Var}(J)}$ where $\text{Var}(J) = \lim_{T \rightarrow \infty} \frac{1}{T} \sum_{t=1}^T (J(t) - J)^2$. The gray dashed lines correspond to $t_{\text{conv}} \sim \theta - \theta_c ^{-2.5}$. Right: The obtained exponent fits well the observations of [88].	94

5.4	Examples of drainage pattern just below θ_c (Left) and above (Right). The black arrow shows the downhill direction. The thickness of the lines represents $\sigma_{i \rightarrow j}$ in logarithmic scale. A few examples showing splitting events are magnified on the left. Here $W = 45$ and $L = 128$, and $J > 0$ even below θ_c due to finite size effects.	95
5.5	Distribution of the site current $P(\sigma)$ in steady state for given average currents J of (a) the erosion model ($L = 256$, $W = 64$) and (b) our mean-field model ($W = 1600$).	96
5.6	(a) Transverse current correlations C_T at θ_c and (b) longitudinal current correlation C_L at θ_c and at $\theta - \theta_c = 0.25$ for $L = 256$ (dashed line). . . .	96
6.1	(a) Hysteresis loop: Magnetization M under a periodic quasi-static driving of the external field h . Inset: magnified segment of the hysteresis loop of a finite size system. (b) Distribution of local stabilities, $\rho(\lambda)$, in locally stable states along the hysteresis loops for different system sizes N . (c) Finite size scaling of the avalanche size distribution $D(n)$ confirms $\tau = \sigma = 1$ up to logarithmic corrections. (d) Correlation $C(\lambda)$ between the least stable spin and spins of stability λ in locally stable states along the hysteresis loop. The data for different system sizes collapses, implying $C(\lambda \ll 1) \sim 1/\lambda$ in the thermodynamic limit.	106
6.2	(a) The average dissipated energy $\Delta\mathcal{H}$ in avalanches of size n scales as $\Delta\mathcal{H} \sim n \ln n / \sqrt{N}$. $-\Delta\mathcal{H}/n$ is a measure of the typical value of the stability of most unstable spins, $\lambda_0(n)$. Thus, in the thermodynamic limit, $\lambda_0 \sim \ln n / \sqrt{N} \ll 1$ even for very large avalanches. (b) The average number of times, $F(n)$, spins active in avalanches of size n re-flip later on in the avalanche.	107

6.3	Illustration of a step in the dynamics, in the SK model and the random walker model. Circles on the λ -axis represent the spins or walkers. At each step, the most unstable spin (in red) is reflected to the stable side, while all others (in green or blue) receive a kick and move. The dashed and solid line outlines the density profile $\rho(\lambda) \sim \lambda$ for $\lambda > 1/\sqrt{N}$. The blue spins were initially frustrated with the flipping spin 0. They are stabilized and are now unfrustrated with 0. In contrast, green spins become frustrated with spin 0 and are softer now. Because of the motion of spins depends on their frustration with spin 0, a correlation builds up at small λ , leading to an overall frustration of “soft” spins among each other.	111
7.1	Boson peak frequency ω^* obtained from equilibrated configurations near T_g vs coordination number δz for different α	116
7.2	(a) (b) Avalanche size distribution $\mathcal{D}(n)$; (c) (d) Magnetization jump distribution $\mathcal{P}(S)$. (a) (c) Reluctant dynamics; (b) (d) Greedy dynamics.	121
7.3	(a) Average avalanche size $\langle n \rangle$ (b) Average magnetization jump $\langle S \rangle$ of avalanches.	122
7.4	Illustration of the dynamic model. Circles on the axis represent the walkers. The leaping walker (in red) jumps to the stable side, and other walkers (in blue) move random steps according to Eq.(7.4).	123
7.5	(a) (c) Distribution of local stability $\rho(\lambda)$ in stable states and (b) (d) Distribution of avalanche size $D(n)$ scaled by finite size N for (a) (b) SK model and (c) (d) random walker model. In the pseudo-gap near $\lambda = 0$, $\rho(\lambda) \propto \lambda$ in both (a) and (c). The collapses in (b) and (d) indicate the power law exponent $\tau = 1.0$, and $\sigma = 1$ with a logarithmic correction. . .	124

A.1	Squares show the shear modulus G normalized by its value at the rigidity threshold for Ge-Se, taken from Ref. [36]. Circles show G for Ge-Sb-Se, taken from Ref. [37]. Lines display the shear modulus G for network models in $d = 3$ using different α , as indicated in the legend.	131
A.2	Angell plot representing $\log \tau$ <i>v.s.</i> inverse temperature T_g/T for different δz and two system sizes $N = 64$ and $N = 256$, $\alpha = 0.0003$.	135
B.1	Illustration of distortion of the triangular lattice, performed to remove straight lines.	141
B.2	Fluctuations of coordination $\langle (z - \bar{z})^2 \rangle$ <i>vs</i> temperature T for different α as indicated in legend. The network size is $N = 256$ and the block size is $N^* = 64$. Mean coordination number corresponds to a) $\bar{z} - z_c = -0.383$, b) $\bar{z} - z_c = -0.055$, c) $\bar{z} - z_c = 0.523$	143
B.3	Boson peak frequency ω^* as a function of excess coordination $\delta z = z - z_c$ for different α as indicated in legend, at temperatures $T = \alpha$. $\omega^* = 0$ indicates that no maximum was observed in $D(\omega)/\omega^{d-1}$, consistent with the presence of fractons at very low frequency.	145
C.1	Variation of density of states $D(\omega, T)$ with temperature for the same $z = -0.055$, $\alpha = 0.0003$. Left: density of states in log-log scale. Right: density of states normalized by its $T = \infty$ value, emphasizing its difference under cooling. Inset: participation ratio $P(\omega, T)$ variation under cooling.	148

C.2	Density of states $D(\omega, T)$ for adaptive networks with different z . (a) Random diluted networks $T = \infty$; a power law $D(\omega) \sim \omega^{-0.25}$ is shown in low frequency range for networks near z_{cen} . (b) Adaptive networks without weak constraints ($\alpha = 0$) at $T = 0.0003$; power laws with different exponents are shown for networks in the rigidity window: $D(\omega) \sim \omega^{-0.25}$ for $\delta z = -0.055$, $D(\omega) \sim \omega^{-0.5}$ for $\delta z = 0.0$. (c) Adaptive networks with weak constraints ($\alpha = 0.0003$) at $T \approx \alpha$; away from isostatic, density of states are gapped between zero frequency and Boson peak, where $D(\omega) \sim \omega^0$. Inset (d) Participation ratio $P(\omega, T)$ at $T = \infty$, see text for definition.	149
C.3	Vector plots of vibrational modes in randomly diluted networks, $N = 100 \times 100$. (a) A typical Debye mode, $\delta z = 0.501$, $\omega = 0.017$. (b) A typical anomalous mode on boson peak, $\delta z = -0.049$, $\omega = 0.011$. (c) A typical fracton, $\delta z = -0.049$, $\omega = 0.0007$	151
C.4	Correlation between a low frequency fractal mode and isostatic clusters. A network configuration ($\delta z = -0.042$) is shown with its springs in the over-constrained regions colored in red, in the isostatic regions colored in green, and in the floppy regions colored in blue. A typical fracton ($\omega = 5 \times 10^{-4}$) specified in this configuration is plotted on top.	154
D.1	Histogram of excitations with given energy change ΔH for different metastable states along the hysteresis curve, $m = 8$, $m' = 16$, and $N = 3000$	157

D.2 The lower data set in solid lines is the total energy $\Delta\mathcal{H}(n)$ dissipated in avalanches of size n . The upper data set in dashed lines is the sum of local stabilities (before the avalanche) of spins that are going to flip in the avalanche, $\sum_{i \text{ flip}} \lambda_i$. This shows that the dissipated energy is vanishingly small as compared to the naïve sum over local stabilities, as $n \rightarrow \infty$, since the two curves scale as different power laws with n 159

D.3 Left: the quantity $NC(\lambda, \lambda')\sqrt{(\lambda + c(N))^2 + (\lambda' + c(N))^2}$ is numerically computed for various λ and λ' , and behaves nearly as a constant (as the color code indicates, this quantity only changes by a factor 3 in the entire range considered. Right: Correlation $C(\lambda, \lambda')$, for $\lambda' = 5\lambda$ with different system sizes N and for different directions $\lambda' = a\lambda$, $a = 0, 1, 2, 5$ with $N = 5000$ 160

List of Appendices

A Why glass elasticity affects the thermodynamics and fragility of super-cooled liquids?	129
B Evolution of covalent networks under cooling	140
C Adaptive elastic networks as a model for supercooled liquids	146
D Dynamics and correlations among soft excitations in marginally stable glasses	155

Chapter 1

Introduction

Statistical physics, one of the cornerstones of modern physics and chemistry, sets the theoretical framework to describe systems in thermal equilibrium. However, more often, systems are not equilibrated. This is the case for open systems which receive energy fluxes from their environments, such as the living or social systems. Other examples are glassy systems, whose thermal activation time is so long that they cannot equilibrate on practical time scales. Examples are the structural glasses that make our windows, whose dynamics are dominated by a glass transition between an equilibrated liquid state and an out-of-equilibrium glass state with an extremely long relaxation time. Other examples are granular materials, where the temperature effect is too small to be relevant. These systems are yield stress materials, which can flow if a sufficient forcing is applied. The transition between the solid and liquid phases is a non-equilibrium dynamical transition. The two transitions are represented in the phase diagram in Fig. 1.1. Understanding them is a long-standing topic of soft condensed matter physics.

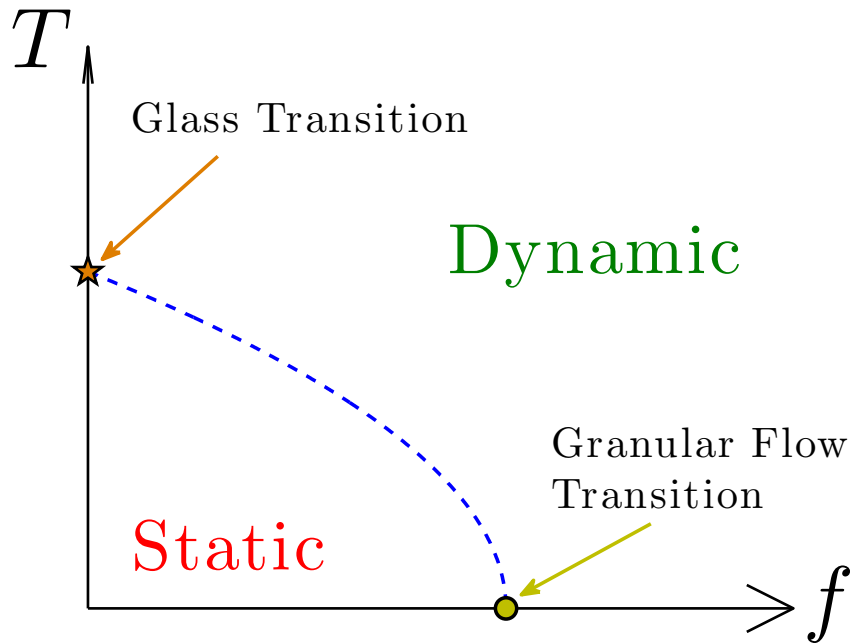


Figure 1.1: A phase diagram of static and dynamic phases of glassy systems. T is the temperature, f is the driving force.

The thermal relaxation of a liquid can be enormously prolonged under cooling [1, 2]. Classical examples are structural glasses, which can be elegantly shaped by blowing them. Blowing is possible because these materials are very viscous and flow on the scale of seconds near the glass transition, compared with picoseconds in liquid phase at high temperature. In light of the long history of glass manufacture [3], it is surprising how little is understood of the microscopic cause for their slow dynamics. In particular, the specific pattern of slowing down near the glass transition depends on the material considered [4, 5]. There is no theoretical framework to predict that dependence.

At zero temperature, the thermal activation time of a glassy system is

absent. The system can however transition from a static state to a dynamic flowing state once a sufficient external forcing is applied. For instance, rocky river beds and sand dunes can flow when pebbles and sand grains are eroded by the water flow and the wind respectively [6]. Many experiments support that erosion occurs only when the stress applied by the fluid exceeds a threshold. Understanding this threshold is important for geophysical applications, as river beds tend to spontaneously evolve toward this threshold where erosion stops [7, 8]. No compelling theoretical framework has been proposed to describe the dynamics near the threshold. One interesting effect is the “armoring” phenomenon: near the threshold, there are long transients where the average number of mobile particles flowing above the frozen bed slowly decays. This slow decay corresponds to the filling up of holes by mobile particles: the system self-organizes into configurations where a minimal number of particles remain mobile.

Another kind of self-organization occurs in glassy systems at zero temperature, when interactions are effectively long-range. Examples include electron glasses, spin glasses or packings of hard particles where elastic interactions dominate. Such systems spontaneously self-organize into configurations that are stable, but barely so. As a consequence, rich dynamics occur when a perturbation is applied. Typical examples are Barkhausen noises in magnetic spin systems [9–11] and avalanches in sand and snow packings. Currently, we lack a dynamical description of how the marginality is reached in these systems.

1.1 Dynamics under cooling – glass transition

A glass is a solid which forms when a supercooled liquid – a liquid at a temperature below its melting point – falls out of equilibrium under cooling. In the practical sense, glass transition is essentially different from other equilibrium phase transitions, where the two phases are both in thermal equilibrium and the transition is determined by symmetry breaking [12, 13]. For example, the translation invariant symmetry breaks in crystallization [12]. By contrast, no obvious symmetry is found broken in the glass transition problem. So there is no comparable theory based on symmetry explaining the glass transition.

The most significant features of glasses are their extremely slow dynamics, which appear to be associated with collective behaviors characterized by an increasing correlation length of the dynamics [14–18]. This increase is however moderate, since the size of collectively rearranging regions in a liquid increases only by four to five times, in contrast to a 10^{16} -fold growth in the relaxation time [1, 2, 19–23]. Experimentalists often fit this fast rise of the relaxation time by the Vogel-Fulcher-Tammann law [24–26],

$$\tau(T) = \tau_0 \exp\left(\frac{A}{T - T_0}\right), \quad (1.1)$$

where τ_0 , A and T_0 are fitting parameters for different materials. The exponential form, Eq.(1.1), indicates that the dynamics in glasses slow down much faster than a typical thermal activation process, where the relaxation time is captured by Arrhenius law:

$$\tau(T) \propto \exp\left(\frac{\Delta F}{T}\right), \quad (1.2)$$

where ΔF is the free energy barrier of relaxation. The two formulas are consistent

only if the free energy barrier ΔF depends on temperature and becomes singular at T_0 . In most fragile liquids, this ΔF can increase by 6 to 7 fold under cooling.

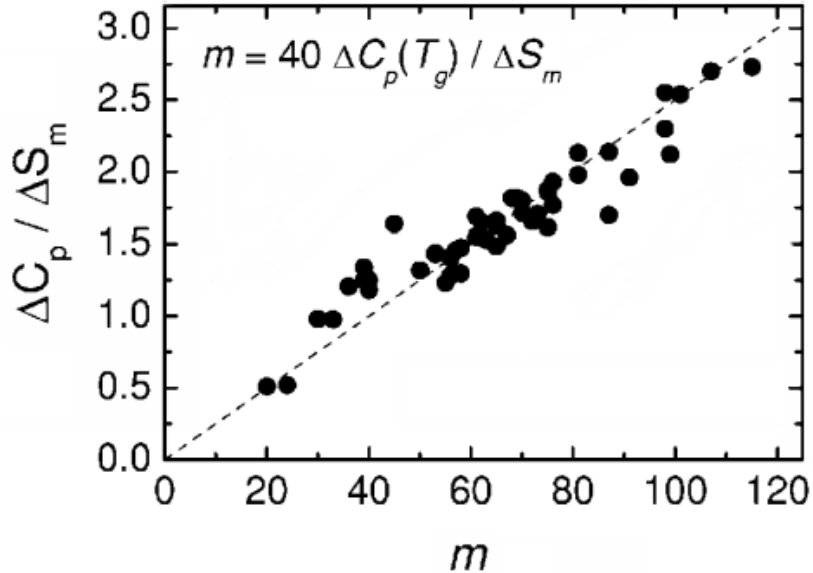


Figure 1.2: Scatter plot of the jump of specific heat $\Delta C_p/\Delta S_m$ and the fragility m of different glassy materials. The dashed line is given by $m = 40\Delta C_p/\Delta S_m$, where ΔS_m is the entropy gain in melting of the same material. The plot is reproduced from Reference [5].

Experiments reveal a connection between the dynamics and thermodynamics in supercooled liquids. For instance, the jump of specific heat Δc_p and the fragility m are linearly correlated for different kinds of glass-forming materials, ranging from network to polymer glasses, as shown in Fig. 1.2 [5, 27]. The fragility, characterizing the temperature dependence of the relaxation time in different materials, is defined as,

$$m \equiv \left. \frac{\partial \ln \tau(T)/\tau_0}{\partial (T/T_g)} \right|_{T=T_g} = \ln \frac{\tau(T_g)}{\tau_0} - \left. \frac{\partial \Delta F(T)}{\partial T} \right|_{T_g}. \quad (1.3)$$

The liquids following the Arrhenius law, Eq.(1.2) with a temperature independent ΔF , are termed as “strong” with small $m_0 = \ln \tau(T_g)/\tau_0$; while those very non-Arrhenius liquids that ΔF increases significantly under cooling are termed as “fragile” with large m values. The jump of specific heat characterizes the number of degrees of freedom contributing to the configuration entropy – the degeneracy of metastable states in the liquid phase. These degrees of freedom are frozen at the glass transition. Specifically, the jump of specific heat is defined as the capacity difference between the liquid phase and the glass phase,

$$\Delta c_p \equiv \frac{1}{N} \left. \frac{\partial H(T)}{\partial T} \right|_{T_g^-}^{T_g^+}, \quad (1.4)$$

where $H(T)/N$ is the enthalpy density of the system. Both m and Δc_p capture the temperature dependence of energy measures of the glasses, must thus be correlated. Most glass theories [21, 28–30] have concentrated on reproducing the linear correlation $\Delta c_p \propto m$, however, only a few [31, 32] have tried to provide an explanation on how they are determined microscopically.

Experiments hint that the elasticity of the structures may be the key factor and both the energy barrier ΔF and the enthalpy H are purely manifestations of this. The elasticity of a structure is featured by its vibration spectra. Glasses are distinguished by the boson peak, a large number of low-frequency modes additional to phonons, in their spectrum. It is found [33, 34] that the fragility of a glass-forming material is inversely proportional to its intensity of the boson peak, defined as,

$$In \equiv R_1^{-1} \equiv \max(D(\omega)/\omega^2)/\min(D(\omega)/\omega^2), \quad (1.5)$$

where $D(\omega)$ is the number density of vibrational modes of frequency ω , shown in

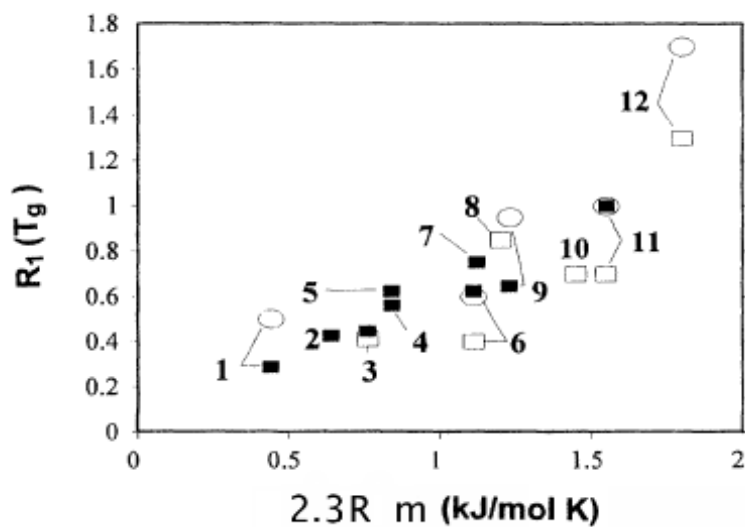


Figure 1.3: Scatter plot of boson peak intensity ratio R_1 and fragility m of different glasses. The plot is reproduced from Reference [33].

Fig. 1.3.

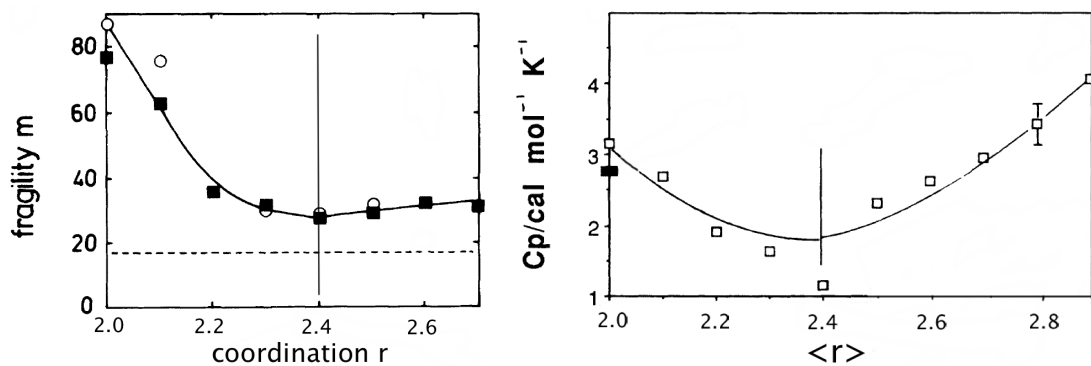


Figure 1.4: The fragility m (Left) and the jump of specific heat Δc_p (Right) of chalcogenides with coordination number r . The plots are reproduced from References [4, 35].

Another line of evidence originates from chalcogenides, a kind of network glasses, where particles interact prominently through specialized covalent bonds, whose number can be experimentally tuned by changing the component ratio [36–

38]. The mechanical stability theory developed by Maxwell [39] predicts that the rigidity of a structure can change by simply tuning the number of constraints in the structure. Applying this to network glasses and counting both the stretching and bending constraints of covalent bonds, Phillips and later Thorpe [40, 41] pointed out that the rigidity of the covalent network sets on at a critical coordination number $r_c = 2.4$, where the coordination number r is the average number of covalent bonds per atom. Experiments [4, 35] indicate a special correlation between the glass properties and this rigidity transition: both the fragility and the jump of specific heat vary non-monotonically when tuning the coordination number and are minimal at the proximity of the rigidity threshold, as shown in Fig. 1.4. Moreover, some recent experiments [42–49] suggest that there exists even a range of coordination number around r_c , where the network glass is strong and the stress distribution is homogeneous. This range near r_c is termed as Intermediate Phase [42].

However, no theory has been developed to successfully rationalize these observations connecting the elasticity of the microscopic structures and the dynamic and thermodynamic properties of the glasses. We develop such a theory and give a quantitative prediction on the thermodynamics of the glasses based on their structures.

1.2 Rigidity of a structure

The two sets of hints on the elasticity of the microscopic structures, the boson peak intensity and the rigidity transition of the interaction network, are in fact

two sides of a coin. Recent observations [47, 50–53] and theories [54–58] on various amorphous materials including jammed packings and random elastic networks indicate that the structures near a rigidity threshold display large boson peaks. At the jamming point [59–61], the hard particle packings become incompressible, which corresponds to the onset of the rigidity of the contact networks where the number of forced contacts equals to the number of degrees of freedom [39]. The densities of states in both jammed packings and critically rigid random networks are filled with low-frequency anomalous modes contributing to strong boson peaks. Therefore, it is essential to investigate the rigidity of a structure in order to study later the correlation of the elasticity and the dynamics of supercooled liquids.

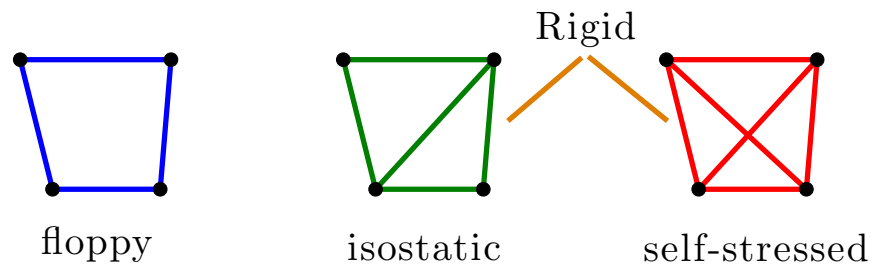


Figure 1.5: An illustration of the rigidity transition of a network by adding pairwise constraints from floppy (Left) to isostatic (Middle) and to self-stressed (Right).

The rigidity of a structure can arise in a purely topological scenario: a network of stiff bonds becomes rigid as the number of bonds increases (independent of the specific geometry), illustrated with a four-joint network in Fig. 1.5. Maxwell [39] first proposed a criterion on the critical number of constraints: when the number of degrees of freedom overwhelms the number of constraints, the structure is floppy with some deformation modes that cost no elastic energy; on the contrary, when the number of constraints exceeds the number of degrees of freedom,

the structure is “more than” rigid – it contains some redundant constraints, removing of which does not affect the rigidity. To characterize these under-constrained and over-constrained features, we define the number of floppy modes (or “zero modes”), F , and the number of redundant constraints (also termed “self-stress states”), N_R . The Maxwell counting indicates [39],

$$F = dN - N_B \quad \text{if } dN > N_B; \quad (1.6)$$

$$N_R = N_B - dN \quad \text{if } dN < N_B, \quad (1.7)$$

where N is the number of particles in the network, d is the spatial dimension, and $N_B \equiv zN/2$, is the number of bonds connecting the particles, with z as the coordination number. In mean-field, the rigidity switches on simultaneously throughout the system at the critical coordination number $z_c = 2N_B/N = 2d$, where there is no floppy modes nor redundant bonds. In general, a random network can violate the special Maxwell counting, Eqs.(1.7), but must satisfy [62, 63],

$$F - N_R = dN - N_B. \quad (1.8)$$

This topological counting is rooted in the linear elasticity of structures [64–66]. We introduce a linear elasticity formalism to give a robust mathematical definition of these numbers and derive the general Maxwell counting, Eq.(1.8).

Consider a generic spring network [63] with no nonlinear structures like two springs adjacent in a straight line, shown in Fig. 1.6. The positions of the particles define a vector $|\vec{R}\rangle$ in $d \times N$ -dimension configuration space, where we use bra-ket notation for vectors. If particle i connects to particle j , the distance

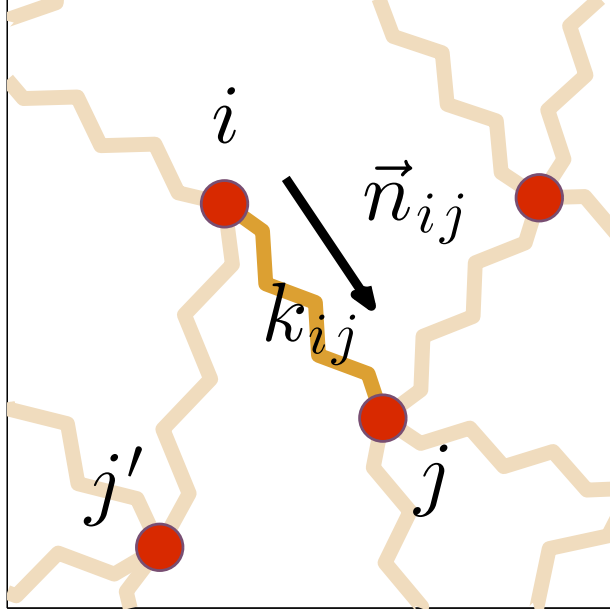


Figure 1.6: Zoom-in illustration of a spring network with a spring of stiffness $k_{\langle i,j \rangle}$ connecting particle i and j .

between the two is given by $r_{\langle i,j \rangle} \equiv \|\vec{R}_i - \vec{R}_j\|$, and N_B springs define a vector $|r\rangle$ in N_B -dimension contact space. If we perturb the system by a small displacement field $|\delta\vec{R}\rangle$, the distance between particles i and j changes by,

$$\delta r_{\langle i,j \rangle} = (\delta\vec{R}_j - \delta\vec{R}_i) \cdot \vec{n}_{ij} + o(\delta\vec{R}^2), \quad (1.9)$$

where \vec{n}_{ij} is the unit vector pointing from i to j . In the linear response region, we neglect all higher order effects, and define a displacement independent matrix, \mathcal{S} , to connect the displacement field $|\delta\vec{R}\rangle$ and the distance change field $|\delta r\rangle$,

$$\mathcal{S}_{\langle i,j \rangle, k} = \vec{n}_{ij}(\delta_{ik} - \delta_{jk}), \quad (1.10)$$

where δ_{ik} is the Kronecker delta function. Equation (1.9) can then be abbreviated as $\delta r_{\langle i,j \rangle} = \sum_k \mathcal{S}_{\langle i,j \rangle, k} \cdot \delta \vec{R}_k$, or simpler as $|\delta r\rangle = \mathcal{S}|\delta \vec{R}\rangle$. The structure matrix, \mathcal{S} , also termed as the compatibility matrix, is N_B by dN .

The relation between the contact tensions and the vector forces on particles is dual to the relation between the distance changes of contacts and the displacements of particles. If there is a tension field $\{f_{\langle i,j \rangle}\}$ on the springs, positive for being stretched and negative for being compressed, the force \vec{F}_i on particle i is

$$\vec{F}_i = \sum_j f_{\langle i,j \rangle} \vec{n}_{ij} = \sum_{\langle j,k \rangle} \vec{n}_{jk} (\delta_{ij} - \delta_{ik}) f_{\langle j,k \rangle}. \quad (1.11)$$

This formula can also be abbreviated as $|\vec{F}\rangle = \mathcal{T}|f\rangle$, where \mathcal{T} is a force-independent dN by N_B matrix. \mathcal{T} and \mathcal{S} are transposes of each other, $\mathcal{T}^t = \mathcal{S}$.

A floppy mode is a vector in configuration space, a displacement field along which does not change the distances of contacts in the linear order. In this formalism, it corresponds to a nontrivial solution of equations, $\mathcal{S}|\delta \vec{R}\rangle = 0$. The number of floppy modes, F , is then equal to the dimension of the kernel of matrix \mathcal{S} [67],

$$F \equiv \dim(\ker \mathcal{S}). \quad (1.12)$$

Similarly, a self-stress state corresponds to a vector in contact space, a tension field along which does not change the mechanical stability, that is to say, $\mathcal{T}|f\rangle = 0$. Accordingly, the number of redundant constraints satisfies

$$N_R \equiv \dim(\ker \mathcal{T}). \quad (1.13)$$

As $\mathcal{T}^t = \mathcal{S}$, $\text{rank}(\mathcal{S}) = dN - F = \text{rank}(\mathcal{T}) = N_B - N_R$ immediately leads to Equation (1.8).

Another benefit from this formalism is that the linear elastic energy corresponding to any small distortion field can be calculated to the linear order without doing relaxation for the mechanical equilibrium. For a given mismatch of springs $|\delta r\rangle = |\epsilon\rangle$, the mechanical equilibrium of the network is achieved with a non-affine response $|\delta \vec{R}_{\text{n.a.}}\rangle$,

$$|\vec{F}\rangle = \mathcal{S}^t |f\rangle = \mathcal{S}^t \mathcal{K} |\epsilon\rangle - \mathcal{S}^t \mathcal{K} \mathcal{S} |\delta \vec{R}_{\text{n.a.}}\rangle = 0, \quad (1.14)$$

$$|\delta \vec{R}_{\text{n.a.}}\rangle = \mathcal{M}^{-1} \mathcal{S}^t \mathcal{K} |\epsilon\rangle, \quad (1.15)$$

where \mathcal{K} is a diagonal matrix with $\mathcal{K}_{\gamma\gamma} = k_\gamma$ the spring constant of spring γ , and $\mathcal{M} \equiv \mathcal{S}^t \mathcal{K} \mathcal{S}$ is the dynamic matrix. The elastic energy equals formally to,

$$\mathcal{H}(|\epsilon\rangle) = \frac{1}{2} \langle \epsilon - \mathcal{S} \delta \vec{R}_{\text{n.a.}} | \mathcal{K} | \epsilon - \mathcal{S} \delta \vec{R}_{\text{n.a.}} \rangle = \frac{1}{2} \langle \epsilon | \mathcal{K} - \mathcal{K} \mathcal{S} \mathcal{M}^{-1} \mathcal{S}^t \mathcal{K} | \epsilon \rangle. \quad (1.16)$$

As the topological counting, Eq.(1.8), captures the essentials of linear elasticity, several linear rigidity transition scenarios relying only on the topology of the interaction networks have been intensively studied. (See Fig. 3.1 for illustration.) First, the rigidity percolation scenario [63, 68–72] searches for a rigid backbone, a rigid cluster spanning over the system, in the networks generated by randomly diluting bonds on lattices. In this scenario, the critical transition is second order at a threshold below z_c [63], characterized by a continuous order parameter P_∞ – the fraction of bonds in the rigid backbone continuous in z . This indicates that the rigid backbone is a fractal object composed of a vanishing number density of

bonds. In addition, the local stresses appear with redundant constraints in rigid islands at a connection density z far below the rigidity threshold, due to the spatial fluctuations of connections.

Based on the assumption that the local stresses cost elastic energy and the networks self-organize to release the energy at low temperature, Thorpe and his followers [73–75] proposed a peculiar rigidity transition scenario, known as “rigidity window”. The self-organized networks are generated by redistributing some of the connections from randomly diluted networks to avoid redundant constraints. The resulting networks contain rigid backbones with finite probabilities [75] from a coordination number $z_{\text{iso}} < z_c$, while the stress only appears when $z > z_c$. The coordination number range from z_{iso} to z_c of rigid non-stressed networks is termed as “rigidity window”. Moreover, this peculiar window has been proposed as a candidate for the intermediate phase observed in chalcogenides [76, 77].

The last scenario, found in the contact networks of jammed packings of soft spheres, obeys the special Maxwell counting: both the rigidity and the stress sets on at the same coordination number. The spatial fluctuation of the connections is so insignificant that a mean-field theory [39, 54, 56, 78] captures the transition. Both the probability of being rigid and the order parameter P_∞ are first-order step functions, that is to say, almost every contact is in the rigid cluster at z_c when the rigidity percolates. Moreover, the mean-field theory predicts that the networks in this scenario possess a shear modulus linear in the coordination number, $G \propto |z - z_c|$, and a flat density of states of anomalous modes, $D(\omega) \sim \omega^0$, above a characteristic frequency $\omega^* \sim |z - z_c|$. In 3D, the boson peak intensity, $In \sim \omega^{*-2}$, is thus peaked at the jamming point when the network is marginally rigid.

Not only does the rigidity transition scenario control the dynamics of the glasses, but the rigidity problem as a non-equilibrium phase transition phenomenon is of fundamental importance in itself. Therefore, it is significant to understand how the network topology evolves under cooling and which of the three rigidity transition scenarios applies to the real glasses.

1.3 Non-equilibrium dynamical phase transition

At zero temperature, a static glassy system can transition to an absorbing dynamical state under a certain dynamical driving. For instance, a flow of pebbles or grains occurs when a viscous fluid shears a substrate of sedimented particles, which are repulsive in short-range. This phenomenon is commonly known as erosion. Water flow and wind shape the Earth's landscape through the erosion effect, which has thus long been the central topic of geophysics [6]. Many theories about the erosion have focused on a continuous description of the particle flux versus certain fluid speed [79–82]. However, this description, which applies when the resuspension of sedimented particles happens, fails near the erosion threshold. Predicting the flux of particles is difficult in the latter case, even though this situation is relevant in gravel rivers, where the river beds self-organize until the fluid stress approaches the threshold value and the erosion stops [7, 8].

A granular material flows at a certain stress anisotropy, $\theta^* = \Sigma/p \sim 1$. In the low Reynolds number region, under a laminar driving flow, the stress anisotropy on the substrate is quantified by a dimensionless Shields number [84], $\theta \equiv \Sigma/(\rho_p - \rho)gd$, where Σ is the shear stress from the fluid, and $(\rho_p - \rho)gd$

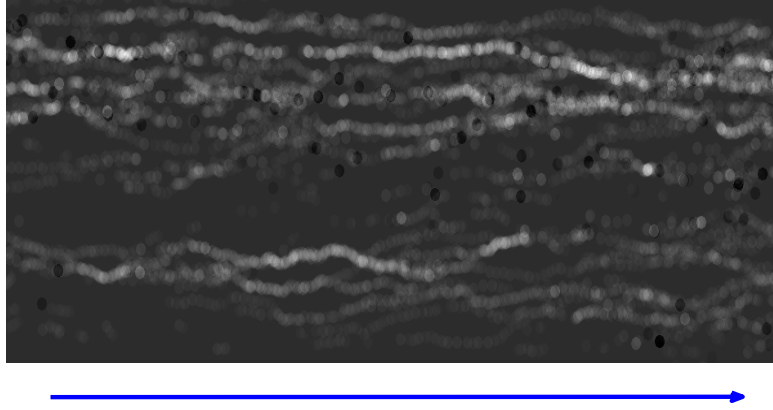


Figure 1.7: Particle trajectories (top view) of a granular bed erosion driven by water flow. The water is injected from the left to right, as indicated by the blue arrow. The plot is reproduced from Reference [83].

quantifies the pressure due to the gravity on one layer of sedimented particles of mass density ρ_p and typical size d immersed in the fluid of density ρ . From hydrodynamics, the relative pressure on particles at depth H below the surface is, $p = (\rho_p - \rho)gH$. The moving particles in the flowing boundary should meet the stress anisotropy requirement, $\Sigma/(\rho_p - \rho)gH \gtrsim \theta^*$, thus, the depth H of the flowing boundary [6] is proportional to the Shields number, $H \lesssim d\theta/\theta^*$. Therefore, there is a threshold $\theta_c \sim \theta^* \sim 1$, near which, $\theta - \theta_c \ll \theta_c$, the moving particles are localized in a layer of a few particle-size thick near the boundary and crawl on the rough surface made of other static particles [6].

As shown by trajectories in the Fig. 1.7, in this region, the particles do not simply follow the laminar flow: they roll around in the perpendicular directions, due to an interplay with the random surface of static particles and the interactions of active particles. Sometimes, the mobile particles may even be trapped and become inactive. Only those particles moving along the laminar flow contribute

to the net flux of sedimented particles. A steady flux, J , switches on when the fluid flow drives stronger than θ_c [84, 85]. (i) Under a constant shear stress near the threshold, the system shows critical dynamics in experiments [81, 82, 86–88],

$$J \sim (\theta - \theta_c)^\beta; \tag{1.17}$$

where β is the critical exponent characterizing the transition. Some works [81, 82, 86, 88] show $\beta = 1$, while other values also fit well in some experiments [87]. (ii) The typical speed of the particles is, however, not critical near the threshold [86, 89, 90]. It is rather the number of active particles that vanishes at the threshold. (iii) Before entering the steady state, the system undergoes a transient process, known as “armoring” or “leveling”, where some of the active particles get trapped and shape the landscape. At the vicinity of the threshold, this transient process is characterized by a typical time scale τ that diverges,

$$\tau \sim |\theta - \theta_c|^{-z}, \tag{1.18}$$

where z is another critical exponent. Surprisingly, though the divergence of the transient time scales and the “armoring” processes in the transients are reported [88], quantitative studies of the divergence [91] and the spatial organization of the flux have barely been done.

Two distinct theoretical views have been proposed for the erosion near the threshold. Bagnold and followers [6, 92] introduced the concept of “a moving flow boundary”, where active particles forming a layer carry a fraction of the shear stress from fluid such that the lower layers remain static under the critical shear

which is balanced by friction. The depth of the flow boundary, or the amount of moving particles, is thus proportional to $\theta - \theta_c$. In this view, the dynamic response recovers the critical flux (*i*) and the vanishing number of moving particles (*ii*). However, this hydrodynamic treatment that the active particles in the boundary move in an average manner captures no transients (*iii*) nor spatial organization of flux and applies only when active particle interactions are irrelevant.

By contrast, the other view raised in erosion/deposition models [86] emphasizes the slow “armoring” of the particle bed. Models assume that initially active particles, moving on a frozen static background, may be trapped by “holes”, which are energy depressions in the landscape. Consequently, the number of active particles contributing to the steady flux is less than the initial number of them. The shear stress θ tunes the number of these energetic “holes”, and θ_c corresponds to the critical stress where the number of holes matches the number of initially active particles. Although this view captures (*i,ii,iii*) qualitatively well, that some of the active particles have to fill all holes and the rest contributes to the steady flux is an implicit assumption, which is highly non-trivial. In fact, the disorder of the static bed will lead the mobile particles to follow favored paths which eventually lead to a few channels, thus exploring only a small fraction of the space, as found in river channels and the aggregations of adhesive particles [93–96]. Some plastic-depinning models of vortex dynamics in dirty Type-II superconductors [97, 98] have argued that the fact that the active particles explore a vanishing fraction of the surface at the threshold implies a vanishing number of holes to be filled and thus a steeper change in the flux, with $\beta > 1$.

To settle these problems in previous views, we start from a dynamical

model capturing the microscopic details missed before, in particular, the interplay between the disorder that leads to channelization and the particle interaction. We then build a theoretical framework based on the model to reveal the microscopic cause for the critical flux-drive relation, Eq.(1.17). Our theory also provides a testable description on the spatial organization of the flux.

1.4 Critical dynamics

In the erosion problem, the granular bed self-organizes into an “armored” state where a minimal number of particles are mobile. Athermal glassy systems with long-range interactions can also self-organize into microscopic states that have rich dynamics and sensitive responses [8, 99, 100], characterized by diverging length and time scales. Their dynamics are in some sense critical: a tiny local perturbation ends up with a response, called an “avalanche”, which can spread over the system and last very long. The frequency distributions of the lifespans and sizes of the response obey a power law,

$$P(A) \sim A^{-\tau} p(A/N^\sigma), \quad (1.19)$$

where A can be either the avalanche duration or size, N is the system size, and N^σ sets a cutoff that diverges in the thermodynamic limit. Common examples of these “scale-free” avalanches are Barkhausen noises and earthquakes.

An important feature of such glassy systems is that the densities of soft

excitations are singular [101], corresponding to the so-called pseudogap:

$$\rho(\lambda) \sim \lambda^\theta \tag{1.20}$$

where the local stability λ quantifies the external field needed to cause an elementary excitation in the system. As shown in Fig. 1.8, such singular distributions are observed in various glassy systems. In Coulomb glasses [101–103], the energy to excite an electron is determined by the electron energy E and its distance to the Fermi level E_f . Experiments find the density of states of electrons is gapped at E_f , shown in Fig. 1.8(a). In spin glasses [11, 101, 104–107], the magnitude of the local magnetic field defines the energy to flip the corresponding spin. Numerics show that the density of local fields λ vanishes linearly at $\lambda = 0$ in mean-field spin glasses, as shown in Fig. 1.8(b). In random packings of hard particles [56, 101, 108], the contact force f characterizes the difficulty to break a contact and the depth h of a gap between two particles features the difficulty to close it and to form a new contact. The densities of both contacts with force f and gaps separated by h follow the singular distribution, Eq.(1.20), shown in Fig. 1.8 (c) and (d).

The pseudogap exponent θ is in general bounded by a stability requirement [101], first recognized by Effros and Shklovskii [102]. For instance, in the example of a mean-field spin glass, the Sherrington-Kirkpatrick (SK) model, Ising spins are randomly coupled with each other, defined by the Hamiltonian,

$$\mathcal{H} = -\frac{1}{2} \sum_{i,j} J_{ij} s_i s_j - h \sum_i s_i, \tag{1.21}$$

where J_{ij} are independent random variables obeying a Gaussian distribution with

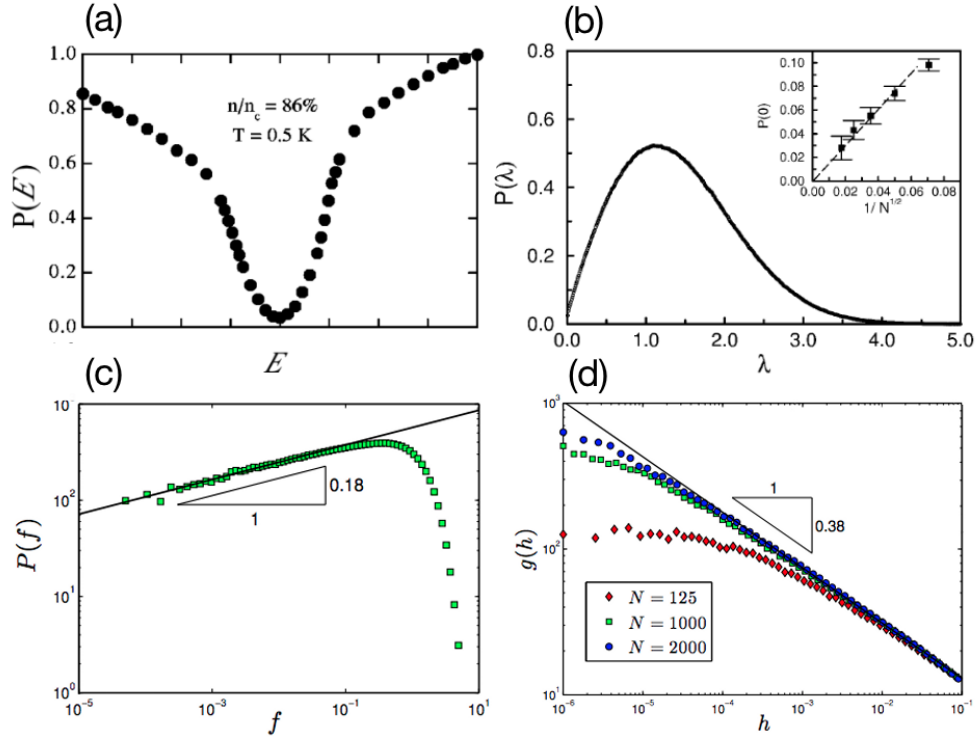


Figure 1.8: Pseudogap in distribution of local stabilities in various glassy systems. (a) Density of states $P(E)$ in Coulomb glasses, where the gap is centered at the Fermi level; (b) Distribution of local fields $P(\lambda)$ in spin glasses; (c) Distribution of contact forces $p(f)$ and (d) distribution of contact gaps $g(h)$ in packings of hard spheres. The plots are reproduced from References [104, 109, 112].

zero mean and variance $1/N$ (N is the system size.). The energy cost (or gain, if the sign is negative) of flipping a set of spins \mathcal{F} from an initial state is,

$$\Delta\mathcal{H} = 2 \sum_{i \in \mathcal{F}} \lambda_i - 2 \sum_{i, j \in \mathcal{F}} J_{ij} s_i s_j \quad (1.22)$$

where $\lambda_i \equiv h_i s_i = (h + \sum_{j \neq i} J_{ij} s_j) s_i$ defines the local stability, the energy cost to flip one spin. A trivial stability requirement demands that every single-spin flip

costs energy, i.e., $\lambda_i > 0$ for $\forall i$. For two-spin flips, from Eq.(1.22), the stability meets when $\lambda_i + \lambda_j - 2J_{ij}s_i s_j \geq 0$ for $\forall i, j$. The worst case to ensure this two-spin flip stability is to flip the two of the lowest λ which are correlated with a positive $J_{ij}s_i s_j$. In this case, $\lambda \sim N^{-1/(1+\theta)}$, presuming the pseudogap distribution, Eq.(1.20), and the typical magnitude of the correlation is determined by the variance of the Gaussian distribution $J_{ij}s_i s_j \sim 1/\sqrt{N}$. Therefore, the pseudogap exponent θ is bounded by $\theta \geq 1$ in the SK model [113, 114].

Very often, these stability bounds are saturated, so that the exponent θ is the minimum one guaranteeing stability, $\theta = 1$, as shown in Fig. 1.8(b) for the SK spin glass. Such marginal stability has been proven for dynamical, out-of-equilibrium situations under a quasi-static driving at zero temperature in the glassy systems with sufficiently long-range effective interactions [101]. The emerging scenario is described in Fig. 1.9, underlying that the dynamics can only probe the boundary between the stable states and the unstable states.

The presence of a pseudogap can be shown to be intrinsically related to the presence of power law avalanches [101]. However, how such pseudogaps emerge dynamically is not understood. Currently, thermodynamic calculation of the distribution of local stabilities has been worked out for the ground state of specific glassy systems [11, 107, 111, 115], but these arguments do not apply in the relevant context of driven athermal systems. In this dissertation, we will explain how the pseudogap appears dynamically in the mean-field spin glass. This work leads to the novel idea that soft excitations are singularly anti-correlated, which we believe will apply broadly to other glassy systems.

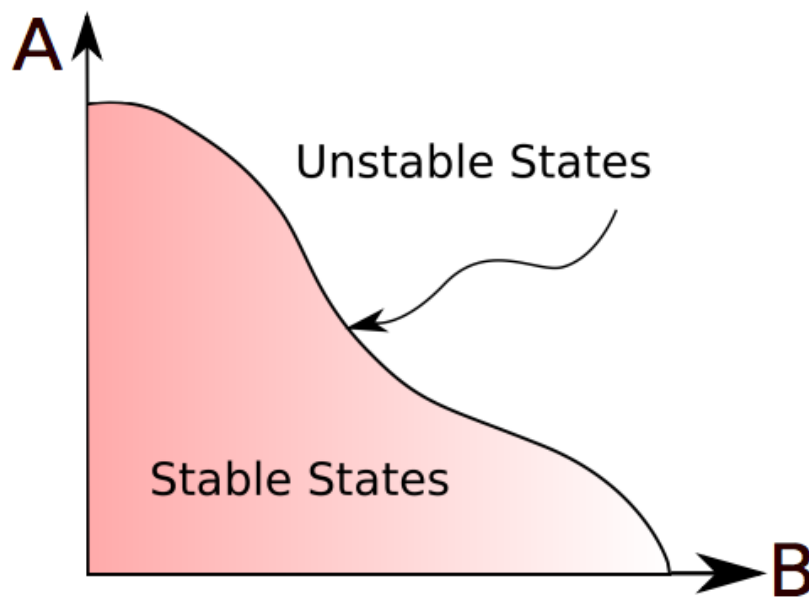


Figure 1.9: Illustration of the evolution of a dynamical system from unstable states to the margin of the stable states in the phase space. A and B are arbitrary coordinates of the phase space. The plot is reproduced from Reference [101].

1.5 Structure of the dissertation

The dissertation is organized in the following order. In *Chapter 2*, we develop an elastic network model of network glasses to unveil the microscopic mechanism that determines the dynamic and thermodynamic properties of glasses, and we derive a thermodynamic theory to predict the non-monotonic dependence of the specific heat on the coordination number. The chapter is a reproduction of the work published in Reference [116]. In *Chapter 3*, we study how the network topology evolves under cooling with a network model with a topology adaptive to the temperature, and we show that the mean-field rigidity transition rather than the rigidity window would apply to the real network glasses due to the existence

of Van der Waals interactions. We reproduce the chapter essentially from the Reference [117]. In *Chapter 4*, we concentrate on the same question as in *Chapter 2*, but including the fact that the network topology evolves under cooling with the model studied in *Chapter 3*. We derive the thermodynamics of the model with features not captured in mean-field rigidity transition. The chapter is a duplication of our work in the Reference [118]. In *Chapter 5*, we investigate the dynamics of driven particles on random surface, which models the erosion of granular river beds. We show model recovers the critical flux-drive relation observed in experiments, as it captures a mechanism missed in the literature. We derive testable predictions on the spatial organization of the erosion flux. The equivalent work is published as the Reference [119]. In *Chapter 6*, we reveal the dynamical emergence of the pseudogap in the mean-field spin-glass with a stochastic description of the critical dynamics. A non-trivial singular correlation among soft excitations arising in the dynamics is the key to the pseudogap. This mechanism can be generalized to other glassy systems. We have published the main content of the chapter in the Reference [120]. In *Chapter 7*, we list the open questions following up with our published works and we discuss briefly the possible methods and preliminary results to tackle them. We conclude the questions and the results on the dynamics of glassy systems in the end.

Chapter 2

Why glass elasticity affects the thermodynamics and fragility of super-cooled liquids

Super-cooled liquids are characterized by their fragility: the slowing down of the dynamics under cooling is more sudden and the jump of specific heat at the glass transition is generally larger in fragile liquids than in strong ones. Despite the importance of this quantity in classifying liquids, explaining what aspects of the microscopic structure controls fragility remains a challenge. Surprisingly, experiments indicate that the linear elasticity of the glass – a purely local property of the free energy landscape – is a good predictor of fragility. In particular, materials presenting a large excess of soft elastic modes, the so-called boson peak, are strong. This is also the case for network liquids near the rigidity percolation, known to affect elasticity. Here we introduce a model of the glass transition based

on the assumption that particles can organize locally into distinct configurations, which are coupled spatially via elasticity. The model captures the mentioned observations connecting elasticity and fragility. We find that materials presenting an abundance of soft elastic modes have little elastic frustration: energy is insensitive to most directions in phase space, leading to a small jump of specific heat. In this framework strong liquids turn out to lie the closest to a critical point associated with a rigidity or jamming transition, and their thermodynamic properties are related to the problem of number partitioning and to Hopfield nets in the limit of small memory.

2.1 Introduction

When a liquid is cooled rapidly to avoid crystallization, its viscosity increases up to the glass transition where the material becomes solid. Although this phenomenon was already used in ancient times to mold artifacts, the nature of the glass transition and the microscopic cause for the slowing down of the dynamics remain controversial. Glass-forming liquids are characterized by their fragility [1, 2]: the least fragile liquids are called strong, and their characteristic time scale τ follows approximatively an Arrhenius law $\tau(T) \sim \exp(E_a/k_B T)$, where the activation energy E_a is independent of temperature. Instead in fragile liquids the activation energy grows as the temperature decreases, leading to a sudden slowing-down of the dynamics. The fragility of liquids strongly correlates with their thermodynamic properties [5, 27]: the jump in the specific heat that characterizes the glass transition is large in fragile liquids and moderate in strong ones. Various theoretical works [21, 29, 121], starting with Adam and Gibbs, have proposed explanations for

such correlations. By contrast few propositions, see e.g. [31, 122], have been made to understand which aspects of the microscopic structure of a liquid determines its fragility and the amplitude of the jump in the specific heat at the transition. This question is conceptually important, but also practically, as solving it would help engineering materials with desired properties.

Observations indicate that the linear elasticity of the glass is a key factor determining fragility – a fact a priori surprising since linear elasticity is a local property of the energy landscape, whereas fragility is a non-local property characterizing transition between meta-stable states. In particular (i) glasses are known to present an excess of soft elastic modes with respect to Debye vibrations at low frequencies, the so-called boson peak that appears in scattering measurements [123]. The amplitude of the boson peak is strongly anti-correlated with fragility, both in network and molecular liquids: structures presenting an abundance of soft elastic modes tend to be strong [33, 34]. (ii) In network glasses, where particles interact via covalent bonds and via the much weaker Van der Waals interactions, the microscopic structure and the elasticity can be monitored by changing continuously the composition of compounds [35, 77, 124, 125]. As the average valence r is increased toward some threshold r_c , the covalent networks display a rigidity transition [40, 41] where the number of covalent bonds is just sufficient to guarantee mechanical stability. Rigidity percolation has striking effects on the thermal properties of super-cooled liquids: in its vicinity, liquids are strong [4, 77] and the jump of specific heat is small [35]; whereas they become fragile with a large jump in specific heat *both* when the valence is increased, and decreased [4, 35, 77]. There are currently no explanations to why increasing the valence affects the glass transition properties in a non-monotonic way, and why such properties are extremal

when the covalent network acquires rigidity.

Recently it has been shown that the presence of soft modes in various amorphous materials, including granular media [51, 126–128], Lennard-Jones glasses [128, 129], colloidal suspensions [52, 53, 55] and silica glass [50, 128] was controlled by the proximity of a jamming transition [60], a sort of rigidity transition that occurs for example when purely repulsive particles are decompressed toward vanishing pressure [51]. Near the jamming transition spatial fluctuations play a limited role and simple theoretical arguments [127, 128] capture the connection between elasticity and structure. They imply that soft modes must be abundant near the transition, suggesting a link between observations (i) and (ii). However these results apply to linear elasticity and cannot explain intrinsically non-linear phenomena such as those governing fragility or the jump of specific heat. In this article we propose to bridge that gap by introducing a model for the structural relaxation in super-cooled liquids. Our starting assumption is that particles can organize locally into distinct configurations, which are coupled at different points in space via elasticity. We study what is perhaps the simplest model realizing this idea, and show numerically that it captures qualitatively the relationships between elasticity, rigidity, thermodynamics and fragility. The thermodynamic properties of this model can be treated theoretically within a good accuracy in the temperature range we explore. Our key result is the following physical picture: when there is an abundance of soft elastic modes, elastic frustration vanishes, in the sense that a limited number of directions in phase space cost energy. Only those directions contribute to the specific heat, which is thus small. Away from the critical point, elastic frustration increases: more degrees of freedom contribute to the jump of specific heat, which increases while the boson peak is reduced.

2.2 Random Elastic Network Model

Our main assumption is that in a super-cooled liquid, nearby particles can organize themselves into a few distinct configurations. Consider for example covalent networks sketched in Fig. 1, where we use the label $\langle ij \rangle$ to indicate the existence of a covalent bond between particles i and j . If two covalent bonds $\langle 12 \rangle$ and $\langle 34 \rangle$ are adjacent, there exists locally another configuration for which these bonds are broken, and where the bonds $\langle 13 \rangle$ and $\langle 24 \rangle$ are formed instead. These two configurations do not have the same energy in general. Moreover going from one configuration to the other generates a local strain, which creates an elastic stress that propagates in space. In turn, this stress changes the energy difference between local configurations elsewhere in the system. This process leads to an effective interaction between local configurations at different locations.

Our contention is that even a simple description of the local configurations – in our case we will consider two-level systems, and we will make the approximation that the elastic properties do not depend on the levels – can capture several unexplained aspects of super-cooled liquids, as long as the salient features of the elasticity of amorphous materials are taken into account. To incorporate in particular the presence of soft modes in the vibrational spectrum we consider random elastic networks. The elasticity of three types of networks have been studied extensively: networks of springs randomly deposited on a lattice [70], on-lattice self-organized networks [77] and off-lattice random networks with small spatial fluctuations of coordination [78, 130, 131]. We shall consider the third class of networks, which are known to capture correctly the scaling properties of elasticity near jamming, and can be treated analytically [78, 127, 132]. In our model two

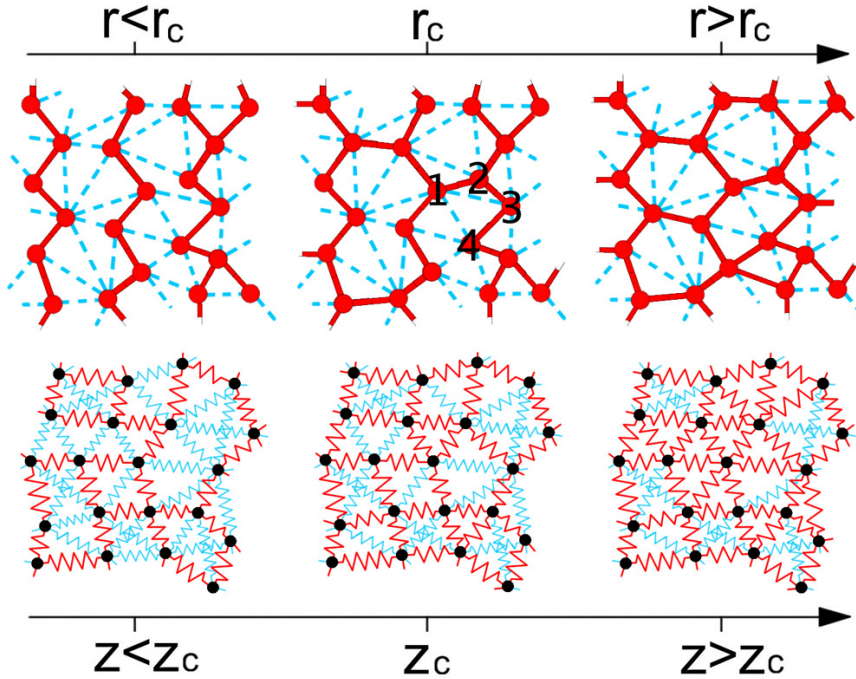


Figure 2.1: Top row: sketches of covalent networks with different mean valence r around the valence r_c : red solid lines represent covalent bonds; cyan dash lines represent van der Waals interactions. Bottom: sketch of our elastic network model with varying coordination number z (defined as the average number of strong springs in red) around Maxwell threshold z_c ; cyan springs have a much weaker stiffness, and model weak interactions.

kinds of springs connect the N nodes of the network: strong ones, of stiffness k and coordination z , and weak ones, of stiffness k_w and coordination z_w . These networks undergo a rigidity transition as z crosses $z_c = 2d$, where d is the spatial dimension. For $z < z_c$ elastic stability is guaranteed by the presence of the weak springs. As indicated in Fig. 1, this situation is similar to covalent networks, where the weak Van der Waals interactions are required to insure stability when the valence r is smaller than its critical value r_c .

Initially when our network is built, every spring $\langle ij \rangle$ is at rest: the rest length follows $l_{\langle ij \rangle}^0 = \|\mathbf{R}_i^0 - \mathbf{R}_j^0\|$, where \mathbf{R}_i^0 is the initial position of the node i . To allow for local changes of configurations we shall consider that any strong spring $\langle ij \rangle$ can switch between two rest lengths: $l_{\langle ij \rangle} = l_{\langle ij \rangle}^0 + \epsilon \sigma_{\langle ij \rangle}$, where $\sigma_{\langle ij \rangle} = \pm 1$ is a spin variable. There are thus two types of variables: the $N_s \equiv zN/2$ spin variables $\{\sigma_{\langle ij \rangle}\}$, which we shall denote using the ket notation $|\sigma\rangle$, and the Nd coordinates of the particles denoted by $|\mathbf{R}\rangle$. The elastic energy $\mathcal{E}(|\mathbf{R}\rangle, |\sigma\rangle)$ is a function of both types of variables. The inherent structure energy $\tilde{\mathcal{H}}(|\sigma\rangle)$ associated with any configuration $|\sigma\rangle$ is defined as:

$$\tilde{\mathcal{H}}(|\sigma\rangle) \equiv \min_{|\mathbf{R}\rangle} \mathcal{E}(|\mathbf{R}\rangle, |\sigma\rangle) \equiv k\epsilon^2 \mathcal{H}(|\sigma\rangle) \quad (2.1)$$

where we have introduced the dimensionless Hamiltonian \mathcal{H} . We shall consider the limit of small ϵ , where the vibrational energy is simply that of harmonic oscillators. In this limit all the relevant information is contained in the inherent structures energy, since including the vibrational energy would increase the specific heat by a constant, which does not contribute to the jump of that quantity at the glass transition. In this limit, linear elasticity implies the form:

$$\mathcal{H}(|\sigma\rangle) = \frac{1}{2} \sum_{\lambda, \beta} \mathcal{G}_{\lambda, \beta} \sigma_\lambda \sigma_\beta + o(\epsilon^2) \equiv \frac{1}{2} \langle \sigma | \mathcal{G} | \sigma \rangle + o(\epsilon^2) \quad (2.2)$$

where λ and β label strong springs, $\mathcal{G}_{\lambda, \beta}$ is the Green function describing how a dipole of force applied on the contact λ changes the amplitude of the force in the contact β . $\mathcal{G}_{\lambda, \beta}$ is computed in Appendix Sec. A.1 and reads:

$$\mathcal{G} = \mathcal{I} - \mathcal{S}_s \mathcal{M}^{-1} \mathcal{S}_s^t \quad (2.3)$$

where \mathcal{I} is the identity matrix, and \mathcal{S}_s and the dimensionless stiffness matrix \mathcal{M} are standard linear operators connecting forces and displacements in elastic networks [64]. They can be formally written as:

$$\begin{aligned} \mathcal{M} &= \mathcal{S}_s^t \mathcal{S}_s + \frac{k_w}{k} \mathcal{S}_w^t \mathcal{S}_w, \\ \mathcal{S}_\bullet &= \sum_{\langle ij \rangle_\bullet \equiv \gamma} |\gamma\rangle \mathbf{n}_{ij} (\langle i| - \langle j|) \end{aligned} \quad (2.4)$$

where $\langle i|\mathbf{R}\rangle \equiv \mathbf{R}_i$, $\langle ij \rangle_\bullet$ indicate a summation over the strong springs ($\bullet = s$) or the weak springs ($\bullet = w$). \mathcal{S}_\bullet is a $N_\bullet \times dN$ matrix which projects any displacement field onto the contact space of strong or weak springs. The components of this linear operator are uniquely determined by the unit vectors \mathbf{n}_{ij} directed along the contacts $\langle ij \rangle$ and point toward the node i .

Finally note that the topology of the elastic network is frozen in our model. This addition of frozen disorder is obviously an approximation, as the topology itself should evolve as local configurations change. Building models which incorporate this possibility, while still tractable numerically and theoretically, remains a challenge.

2.3 Numerical Results of the Model

2.3.1 Network structure

Random networks with weak spatial fluctuations of coordination can be generated from random packings of compressed soft particles [78, 130, 131]. We consider packings with periodic boundary conditions. The centers of the particles correspond to the nodes of the network, of unit mass $m = 1$, and un-stretched springs of stiffness $k = 1$ are put between particles in contact. Then springs are removed, preferably where the local coordination is high, so as to achieve the desired coordination z . In a second phase, N_w weak springs are added between the closest unconnected pairs of nodes. The relative effect of those weak springs is best characterized by $\alpha \equiv (z_w/d)(k_w/k)$, which we modulate by fixing $z_w = 6$ and changing (k_w/k) . Note that an order of magnitude estimate of α in covalent glasses can be obtained by comparing the behavior of the shear modulus G in the elastic networks [130] and in network glasses near the rigidity transition. As shown In Fig. A.1 of Appendix Sec. A.2, this comparison yields the estimate that $\alpha \in [0.01, 0.05]$.

2.3.2 Thermodynamics

We introduce the rescaled temperature $T = \tilde{T}k_B/(k\epsilon^2)$ where \tilde{T} is the temperature. To equilibrate the system, we perform a one spin-flip Monte Carlo algorithm. The energy \mathcal{H} of configurations are computed using Eq.(2.2). We use 5 networks of $N = 256$ nodes in two dimensions and $N = 216$ in three dimensions, each run with 10 different initial configurations. Thus our results are averaged on

these 50 realizations. We perform 10^9 Monte Carlo steps at each T . The time-average inherent structure energy $E(T)$ is calculated, together with the specific heat $C_v = \partial E / \partial T$. The intensive quantity $c(T) \equiv C_v / N_s$ is represented in Fig. 2 for various excess coordination $\delta z = z - z_c$ and $\alpha = 3 \times 10^{-4}$. We observe that the specific heat increases under cooling, until the glass transition temperature T_g where $c(T)$ rapidly vanishes, indicating that the system falls out of equilibrium.

The amplitude of $c(T)$ just above T_g thus corresponds to the jump of specific heat Δc , and is shown in Fig. 3. Our key finding is that as the coordination increases, $\Delta c(z)$ varies non-monotonically and is minimal in the vicinity of the rigidity transition for all values of α investigated, as observed experimentally [35, 77]. This behavior appears to result from a sharp asymmetric transition at $\alpha \rightarrow 0$. For $z > z_c$ we observe that $\Delta c(z) \propto \delta z$. The jump in specific heat thus vanishes as $\delta z \rightarrow 0^+$ where the system can be called “perfectly strong”. For $z < z_c$, Δc is very rapidly of order one. When α increases, this sharp transition becomes a cross-over, marked by a minimum of $\Delta c(z)$ at some coordination larger but close to z_c .

2.3.3 Dynamics

To characterize the dynamics we compute the correlation function $C(t) = \langle \sigma(t) | \sigma(0) \rangle$, which decays to zero at long time in the liquid phase. We define the relaxation time τ as $C(\tau) = 1/2$, and the glass transition temperature T_g as $\tau(T_g) / \tau(\infty) = 10^5$. Finite size effects on τ appear to be weak, as shown in Appendix Sec. A.3. The Angell plot representing the dependence of τ with inverse rescaled temperature is shown in the inset of Fig. 4. It is found that the dynamics

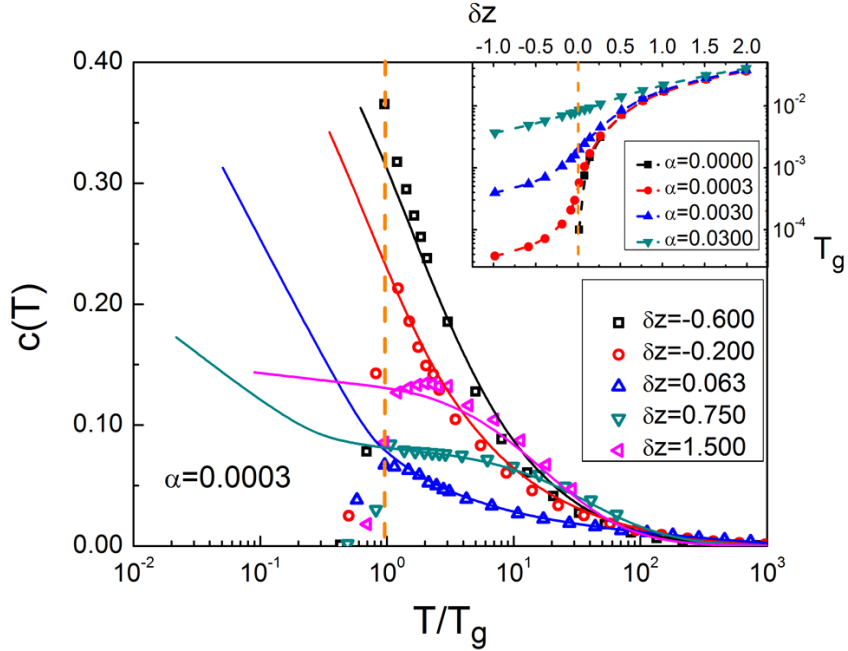


Figure 2.2: Specific heat $c(T)$ *v.s.* rescaled temperature T/T_g for various excess coordination $\delta z \equiv z - z_c$ as indicated in legend, for $\alpha = 3 \times 10^{-4}$ and $d = 2$. $c(T)$ displays a jump at the glass transition. Solid lines are theoretical predictions, deprived of any fitting parameters, of our mean-field approximation. They terminate at the Kautzman temperature T_K . Inset: glass transition temperature T_g *vs.* δz for several amplitude of weak interactions α , as indicated in legend.

follows an Arrhenius behavior for $\alpha \rightarrow 0$ and $z \approx z_c$. Away from the rigidity transition, the slowing down of the dynamics is faster than Arrhenius. To quantify this effect we compute the fragility $m \equiv \frac{\partial \log \tau}{\partial (T_g/T)}|_{T=T_g}$, whose variation with coordination is presented in Fig. 4. Our key finding is that for all weak interaction amplitudes α studied, the fragility depends non-monotonically on coordination and is minimal near the rigidity transition, again as observed empirically in covalent liquids [4]. As was the case for the thermodynamic properties, the fragility appears to be controlled by a critical point present at $\alpha = 0$ and $z = z_c$ where the liquid

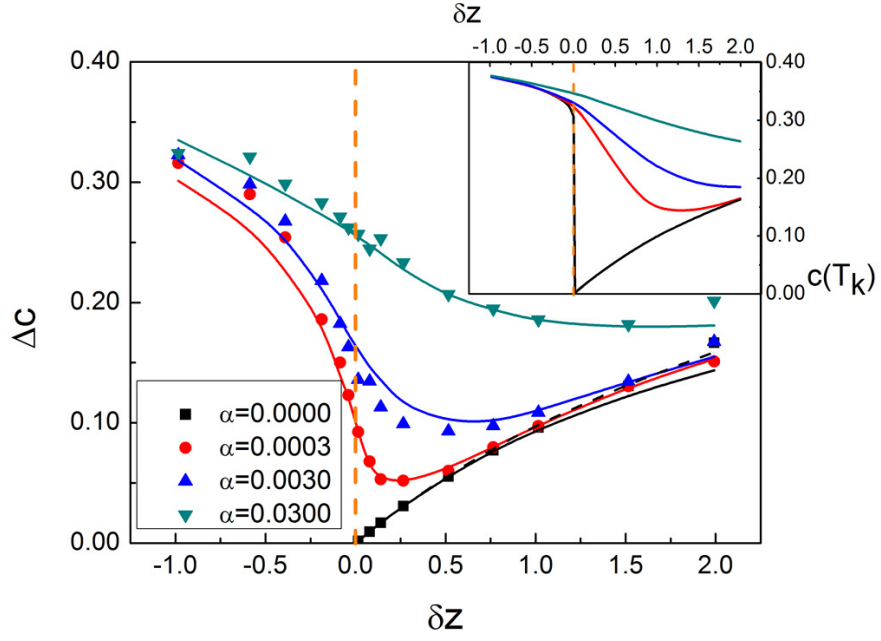


Figure 2.3: Jump of specific heat Δc versus excess coordination δz in $d = 2$ for different strength of weak springs α , as indicated in legend. Solid lines are mean-field predictions not enforcing the orthogonality of the $|\delta r_p\rangle$, dashed-line corresponds to the ROM where orthogonality is enforced. In both cases the specific heat is computed at the numerically obtained temperature T_g . Inset: theoretical predictions for Δc vs δz computed at the theoretical temperature T_K .

is strong, and the dynamics is simply Arrhenius. As the coordination changes and $|\delta z|$ increases, the liquid becomes more fragile. The rapid change of fragility near the rigidity transition is smoothed over when the amplitude of the weak interaction α is increased.

2.3.4 Correlating boson peak and fragility

The presence of soft elastic modes in glasses is traditionally analyzed by considering the maximum of $Z(\omega) \equiv \frac{D(\omega)}{\omega^2}$ [123], where $D(\omega)$ is the vibrational density of states. $Z(\omega)$ quantifies the departure from Debye behavior. The maximum of $Z(\omega)$ defines the boson peak frequency ω_{BP} [123]. To characterize the amplitude of the peak, Sokolov and coworkers [33, 34] have introduced a dimensionless quantity $\tilde{R}_1 \equiv \frac{Z(\omega_{min})}{Z(\omega_{BP})}$, where ω_{min} is the minimum of $Z(\omega)$ for $\omega \in [0, \omega_{BP}]$. \tilde{R}_1 characterizes the inverse amplitude of the boson peak, and was shown to strongly correlate with fragility [33, 34] both in molecular liquids and covalent networks.

To test if our model can capture this behavior we compute the density of states via a direct diagonalization of the stiffness matrix, see Eq.(2.4). Then we extract the maximum $Z(\omega_{BP})$ of $D(\omega)/\omega^2$. We find that below this maximum, $Z(\omega)$ is monotonic, implying that $\omega_{min} = 0$. For all coordinations if $\alpha > 0$ the density of states follows a Debye behavior at low frequency in such networks [78, 132], and in three dimensions $D(\omega) \sim \omega^2/G^{3/2}$ where G is the shear modulus. Thus $\tilde{R}_1 \sim 1/(G^{3/2}Z(\omega_{BP})) \equiv R_1$. The dependence of R_1 is represented in Fig. 5 and shows a minimum near the rigidity transition, and even a cusp in the limit $\alpha \rightarrow 0$. This behavior can be explained in terms of previous theoretical results on the density of states near the rigidity transition, that supports that $R_1 \sim |\delta z|^{1/2}$ when $\alpha \rightarrow 0$ ¹.

Fig. 5 shows that R_1 and the liquid fragility m are correlated in our model,

¹ When $\alpha \rightarrow 0$ and $\delta z > 0$, $\omega_{BP} \sim \delta z$ and $D(\omega_{BP}) \sim 1$ [127], whereas $G \sim \delta z$ [128], leading to $R_1 \sim \sqrt{\delta z}$. For $\delta z < 0$, $G \sim -\alpha/\delta z$ [130]. On the other hand the boson peak is governed by the fraction $\sim \delta z$ of floppy modes, which gain a finite frequency $\sim \sqrt{\alpha}$ [78] thus we expect $D(\omega_{BP}) \sim -\delta z/\sqrt{\alpha}$ and $R_1 \sim \sqrt{-\delta z}$.

thus capturing observations in molecular liquids. The model also predicts that R_1 and the jump of specific heat are correlated. Note that the correlation between fragility and R_1 is not perfect, and that two branches, for glasses with low and with high coordinations, are clearly distinguishable. In general we expect physical properties to depend on the full structure of the density of states, as will be made clear for the thermodynamics of our model below. The variable R_1 , which is a single number, cannot capture fully this relationship. In our framework it is a useful quantity however, as it characterizes well the proximity of the jamming transition.

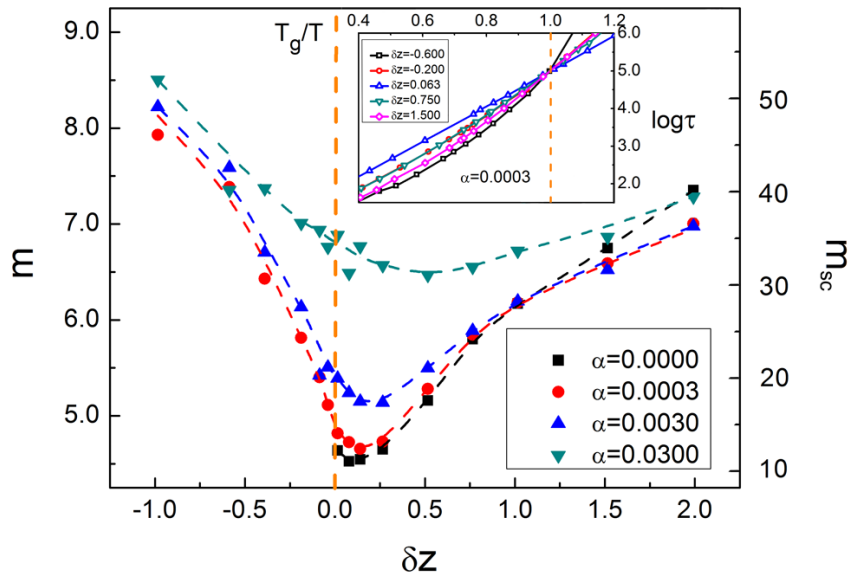


Figure 2.4: Fragility m versus excess coordination δz for different strength of weak interactions α as indicated in legend, in $d = 2$. Dash dot lines are guide to the eyes, and reveal the non-monotonic behavior of m near the rigidity transition. Inset: Angell plot representing $\log \tau$ *v.s.* inverse temperature T_g/T for different δz and $\alpha = 3 \times 10^{-4}$.

2.4 Theory on Thermodynamics of the Model

2.4.1 Thermodynamics in the absence of weak interactions

$$(\alpha = 0)$$

In the absence of weak springs the thermodynamics is non-trivial if $z \geq z_c$, otherwise the inherent structure energies are all zero. Then Eq.(2.4) implies $\mathcal{M} = \mathcal{S}_s^t \mathcal{S}_s$, and Eq.(2.3) leads to $\mathcal{G} = \mathcal{I} - \mathcal{S}_s(\mathcal{S}_s^t \mathcal{S}_s)^{-1} \mathcal{S}_s^t$. Inspection of this expression indicates that \mathcal{G} is a projector on the kernel of \mathcal{S}_s^t , which is generically of dimension $N_s - Nd \equiv \delta z N/2$. This kernel corresponds to all the sets of contact forces that balance forces on each node [128]. We denote by $|\delta r_p\rangle, p = 1, \dots, \delta z N/2$ an orthonormal basis of this space. We may then rewrite $\mathcal{G} = \sum_p |\delta r_p\rangle \langle \delta r_p|$ and Eq.(2.2) as:

$$\mathcal{H}(|\sigma\rangle) = \frac{1}{2} \sum_{p=1}^{\delta z N/2} \langle \sigma | \delta r_p \rangle^2 \quad (2.5)$$

Eq.(2.5) is a key result, as it implies that near the rigidity transition the number $\delta z N/2$ of directions of phase space that cost energy vanishes. Only those directions can contribute to the specific heat, which must thus vanish linearly in δz as the rigidity transition is approached from above.

Eq.(2.5) also makes a connection between strong liquids in our framework and well-know problems in statistical mechanics. In particular Eq.(2.5) is similar to that describing Hopfield nets [133] used to store $\delta z N/2$ memories consisting of the spin states $|\delta r_p\rangle$. The key difference is the sign: in Hopfield nets memories correspond to meta-stables states, whereas in our model the vectors $|\delta r_p\rangle$ corresponds to maxima of the energy. A particularly interesting case is $\delta z N/2 = 1$, the closest

point to the jamming transition which is non-trivial. In this situation the sum in Eq.(2.5) contains only one term: $\mathcal{H}(|\sigma\rangle) = \frac{1}{2}\langle\sigma|\delta r_1\rangle^2 = \frac{1}{2}(\sum_{\alpha=1}^{N_s} \delta r_{1,\alpha}\sigma_\alpha)^2$. This Hamiltonian corresponds to the NP complete partitioning problem [134], where given a list of numbers (the $\delta r_{1,\alpha}$) one must partition this list into two groups whose sums are as identical as possible. Thermodynamically this problem is known [135] to map into the random energy model [136] where energy levels are randomly distributed.

It is in general very difficult to compute the thermodynamic functions of the problem defined by Eq.(2.5) because the vectors $|\delta r_p\rangle$ present spatial correlations, as must be the case since the amplitude of the interaction kernel $\mathcal{G}_{\gamma,\beta}$ must decay with distance. However this effect is expected to be mild near the rigidity transition. Indeed there exists a diverging length scale at the transition, see [78] for a recent discussion, below which $\mathcal{G}_{\gamma,\beta}$ is dominated by fluctuations and decays mildly with distance. Beyond this length scale $\mathcal{G}_{\gamma,\beta}$ presents a dipolar structure, as in a standard continuous elastic medium. We shall thus assume that $|\delta r_p\rangle$ are random unitary vectors, an approximation of mean-field character expected to be good near the rigidity transition.

Within this approximation, the thermodynamic properties can be derived for any spectrum of \mathcal{G} [137]. If the orthogonality of the vectors $|\delta r_p\rangle$ is preserved, the Hamiltonian of Eq.(2.5) corresponds to the Random Orthogonal Model (ROM) whose thermodynamic properties have been derived [137] as well as some aspects of the dynamics [138]. Comparison of the specific heat of our model and the ROM predictions of [137] is shown in Fig. 3 and are found to be very similar. For sake of simplicity, in what follows we shall also relax the orthogonal condition on the

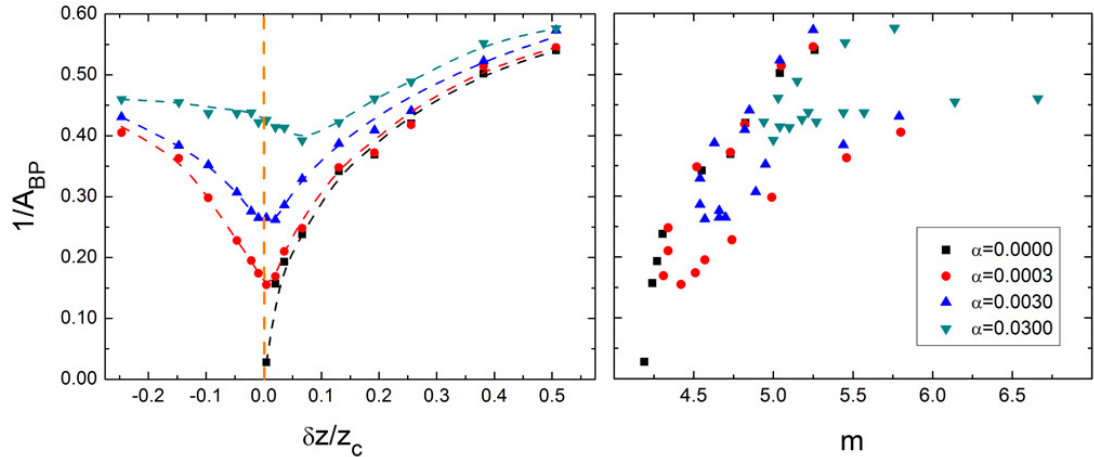


Figure 2.5: Left: Inverse boson peak amplitude R_1 versus excess coordination δz in our $d = 3$ elastic network model, for different weak interaction strengths as indicated in legend. Dash dot lines are drawn to guide one's eyes. Right: Inverse boson peak amplitude R_1 versus fragility m for different weak springs α .

vectors $|\delta r_p\rangle$. This approximation allows for a straightforward analytical treatment in the general case $\alpha \neq 0$, and is also very accurate near the rigidity transition since the number of vectors $\delta z N/2$ is significantly smaller than the dimension of the space dN they live in, making random vectors effectively orthogonal. Under these assumptions we recover the random Hopfield model with negative temperature.

In the parameter range of interest, the Hopfield free energy $\mathcal{F} = \overline{\ln(\mathcal{Z})}$ (here $\overline{(\dots)}$ represents the disorder average on the $|\delta r_p\rangle$) is approximated very precisely by the annealed free energy $\ln(\overline{\mathcal{Z}})$ (this is obviously true for the number partitioning problem that maps to the Random Energy Model), which can be easily calculated. Indeed in our approximations the quantities $X_p \equiv \langle \sigma | \delta r_p \rangle$ are

independent gaussian random variables of variance one, and:

$$\bar{Z} \propto \int \left(\prod_{p=1}^{N\delta z/2} dX_p \frac{1}{\sqrt{2\pi}} e^{-X_p^2/2} \right) e^{-\frac{1}{2T} \sum_p X_p^2} \quad (2.6)$$

Performing the Gaussian integrals we find:

$$c(T) = \frac{\delta z}{2z} \frac{1}{(1+T)^2} \quad (2.7)$$

The Kautzman temperature defined as $s(T_K) = 0$ is found to follow $T_K \approx \frac{2}{e} 2^{-2z/\delta z}$. Eq.(2.7) evaluated at T_g is tested against the numerics in Fig. 3 and performs remarkably well for the range of coordination probed.

2.4.2 General case ($\alpha \neq 0$)

To solve our model analytically in the presence of weak interactions, we make the additional approximation that the associated coordination $z_w \rightarrow \infty$, while keeping $\alpha \equiv z_w k_w / (kd)$ constant. In this limit weak springs lead to an effective interaction between each node and the center of mass of the system, that is motionless. Thus the restoring force stemming from weak interactions $|\mathbf{F}_w\rangle$ follows $|\mathbf{F}_w\rangle = -\alpha|\delta\mathbf{R}\rangle$, leading to a simple expression in the stiffness matrix Eq.(2.4) for the weak spring contribution $\frac{k_w}{k} \mathcal{S}_w^t \mathcal{S}_w = \alpha \mathcal{I}$. It is useful to perform the eigenvalue decomposition:

$$\mathcal{S}_s^t \mathcal{S}_s = \sum_{\omega} \omega^2 |\delta\mathbf{R}_\omega\rangle \langle \delta\mathbf{R}_\omega| \quad (2.8)$$

where $|\delta\mathbf{R}_\omega\rangle$ is the vibrational mode of frequency ω in the elastic network without weak interactions. We introduce the orthonormal eigenvectors in contact space $|\delta r_\omega\rangle \equiv \mathcal{S}_s|\delta\mathbf{R}_\omega\rangle/\omega$ defined for $\omega > 0$. For $\delta z < 0$ these vectors form a complete basis of that space, of dimension N_s . When $\delta z > 0$ however, this set is of dimension $Nd < N_s$, and it must be completed by the kernel of \mathcal{S}_s^t , i.e. the set of the $|\delta r_p\rangle$, $p = 1, \dots, \delta z N/2$ previously introduced. Using this decomposition in Eq.(2.3,2.4) we find:

$$\mathcal{H}(|\sigma\rangle) = \frac{1}{2} \sum_{p=1}^{\delta z N/2} \langle \sigma | \delta r_p \rangle^2 + \frac{1}{2} \sum_{\omega>0} \frac{\alpha}{\alpha + \omega^2} \langle \sigma | \delta r_\omega \rangle^2 \quad (2.9)$$

where the first term exists only for $\delta z > 0$. Using the mean field approximation that the set of $|\delta r_p\rangle$ and $|\delta r_\omega\rangle$ are random gaussian vectors, the annealed free energy is readily computed, as shown in Appendix Sec. A.4. We find in particular for the specific heat:

$$c(T) = \frac{\delta z}{2z} \frac{\theta(\delta z)}{(1+T)^2} + \frac{1}{2N_s} \sum_{\omega>0} \left(\frac{\alpha}{\alpha + (\omega^2 + \alpha)T} \right)^2 \quad (2.10)$$

where $\theta(x)$ is the unitary step function. To compare this prediction with our numerics without fitting parameters, we compute numerically the vibrational frequencies for each value of the coordination. Our results are again in excellent agreement with our observations, as appears in Figs. 2, 3.

To obtain the asymptotic behavior near jamming, we replace the summation over frequencies in Eq.(2.10) by an integral $\sum_{\omega>0} \rightarrow N_s \int d\omega D(\omega)$. The associated density of vibrational modes $D(\omega)$ in such networks has been computed theoretically [78, 127, 132]. These results allows us to compute the scaling behavior of thermodynamic properties near the rigidity transition, see Appendix Sec. A.5.

We find that the specific heat increases monotonically with decreasing temperature. Its value at the Kautzman temperature thus yields an upperbound on the jump of specific heat. In the limit $\alpha \rightarrow 0$, we find that a sudden discontinuity of the jump of specific heat occurs at the rigidity transition:

$$c(T_K) \sim \frac{\delta z}{2z} \quad \text{for } \delta z > 0 \quad (2.11)$$

$$\lim_{\delta z \rightarrow 0^-} c(T_K) \sim \frac{\pi z_c}{8z} \quad \text{for } \delta z < 0 \quad (2.12)$$

Eq.(2.11) states that adding weak interactions is not a singular perturbation for $\delta z > 0$, and we recover Eq.(2.7). On the other hand for $\delta z < 0$, the energy of inherent structures is zero in the absence of weak springs, which thus have a singular effect. The relevant scale of temperature is then a function of α . In particular we find that the Kautzman temperature is sufficiently low that all the terms in the second sum of Eq.(2.10) contribute significantly to the specific heat, which is therefore large as Eq.(2.12) implies. Thus as the coordination decreases below the rigidity transition, one goes discontinuously from a regime where at the relevant temperature scale the energy landscape consists of a vanishing number of costly directions in phase space, whose cost is governed by the strong interaction k , to a regime where the weak interaction α is the relevant one, and where at the relevant temperature scale all directions in phase space contribute to the specific heat.

Note that although the sharp change of thermodynamic behavior that occurs at the rigidity transition is important conceptually, empirically a smooth cross-over will always be observed. This is the case because (i) α is small but finite. As α increases this sharp discontinuity is replaced by a cross-over at a coordination

$\delta z \sim \ln(1/\alpha)^{-1}$ (see Appendix Sec. A.5) where $c(T_K, z)$ is minimal, as indicated in the inset of Fig. 3. (ii) The Kautzman temperature range is not accessible dynamically, i.e. $T_g \gg T_K$ near the rigidity transition. Comparing Fig. 3 with its inset, our theory predicts that the minimum of $c(T_g)$ is closer to z_c and more pronounced than at T_K .

2.5 Discussion

Previous work [60] has shown that well-coordinated glasses must have a small boson peak, which increases as the coordination (or valence for network glasses) is decreased toward the jamming (or rigidity) transition. Here we have argued that as this process occurs, elastic frustration vanishes: thanks to the abundance of soft modes, any configuration (conceived here as a set of local arrangements of the particles) can relax more and more of its energy as jamming is approached from above. As a result, the effective number of degrees of freedom that cost energy and contribute to the jump of specific heat at the glass transition vanishes. As the coordination is decreased further below the rigidity transition, the scale of energy becomes governed by the weak interactions (such as Van der Waals) responsible for the finite elasticity of the glass. At that scale, all direction in phase space have a significant cost and the specific heat increases. This view potentially explains why linear elasticity strongly correlates to key aspects of the energy landscape in network and molecular glasses [33–35, 77, 124]. This connection we propose between structure and dynamics can also be tested numerically. For example, the amplitude of weak interactions can be increased by adding long-range forces to the interaction potential [128, 129]. According to our analysis,

doing so should increase fragility, in agreement with existing observations [139].

The model of the glass transition we introduced turns out to be a spin glass model, with the specificity that (i) the interaction is dipolar in the far field, and that (ii) the sign of the interaction is approximatively random below some length scale l_c that diverges near jamming, where the coupling matrix has a vanishingly small rank. Applying spin glass models to structural glasses have a long history. In particular the Random First Order Theory (RFOT) [29] is based on mean-field spin glass models that display a thermodynamic transition at some T_K where the entropy vanishes. A phenomenological description of relaxation in liquids near T_K based on the nucleation of random configurations leads to a diverging time scale and length scale ξ at T_K [21, 29]. One limitation of this approach is that no finite dimensional spin models have been shown to follow this scenario so far [140], and it would thus be important to know if our model does display a critical point at finite temperature. Our model will also allow one to investigate the generally neglected role of the action at a distance allowed by elasticity, characterized by a scale l_c . In super-cooled liquids heterogeneities of elasticity (that correlates to irreversible rearrangements) can be rather extended [141] suggesting that l_c is large. This length scale may thus play an important role in a description of relaxation in liquids, and in deciphering the relationship between elastic and dynamical heterogeneities.

Chapter 3

Evolution of Covalent Networks under Cooling: Contrasting the Rigidity Window and Jamming Scenarios

We study the evolution of structural disorder under cooling in supercooled liquids, focusing on covalent networks. We introduce a model for the energy of networks that incorporates weak non-covalent interactions. We show that at low-temperature, these interactions considerably affect the network topology near the rigidity transition that occurs as the coordination increases. As a result, this transition becomes mean-field and does not present a line of critical points previously argued for, the “rigidity window”. Vibrational modes are then not fractons, but instead are similar to the anomalous modes observed in packings of particles near

jamming. These results suggest an alternative interpretation for the intermediate phase observed in chalcogenides.

3.1 Introduction

The physics of amorphous materials is complicated by the presence of structural disorder, which depends on temperature in supercooled liquids, and on system preparation in glasses. As a result, various properties of amorphous solids are much less understood than in their crystalline counterparts, such as the non-linear phenomena that control plasticity under stress [142, 143] or the glass transition [1], or even linear properties like elasticity. Concerning the latter, glasses present a large excess of soft elastic modes, the so-called boson peak [123], and their response to a point perturbation can be heterogeneous on a scale l_c larger than the particle size [144–147]. Recent progress has been made on these questions for short-ranged particles with radial interactions [60]. A central aspect of these systems is the *contact network* made by interacting particles, and its associated average coordination z . Scaling behaviors [60] are observed at the unjamming transition where $z \rightarrow z_c$, where $z_c = 2d$ is the minimal coordination required for stability [39] in spatial dimension d . As this bound is approach most of the vibrational spectrum consists of strongly-scattered but extended modes [51, 148] coined *anomalous modes* [128], whose characteristic onset frequency ω^* vanishes [128, 148] and length scale l_c diverges [146, 148] at threshold. Surprisingly, these critical behaviors can be computed correctly by mean-field approximations, which essentially assume that the spatial fluctuations of coordination are small [127, 149, 150]. Likewise, some detailed aspects of the structure of random close packing

are well captured by infinite dimensional calculations [115, 151]. However, it is unclear if these results, which assume that structural fluctuations are mild, apply generically to glasses.

In particular, it is generally believed that fluctuations in the structure are fundamental in covalent glasses such as chalcogenides. In these systems the degree of bonding z plays a role analogous to coordination, and can be changed continuously in compounds such as $Se_xAs_yGe_{1-x-y}$, allowing to go from a polymeric, under-coordinated glass ($x = 1, y = 0$) to well-connected structures. Around a mean valence $z_c = 2.4$ one expects the network to become rigid [40, 152]. Near z_c there is a range of valence, called the intermediate phase [42–46], where the supercooled liquid is strong and the jump of specific heat is small [4, 35], and where the glass almost does not age at all [42–46, 153, 154]. Theoretically, at least three distinct scenarios were proposed (but see [155] for a recent fourth proposition) to describe this rigidity transition, see Fig. 3.1. Fluctuations are important in the first two. The *rigidity percolation* model [63, 68, 156, 157] assumes that bonds are randomly deposited on a lattice. This leads to a second order transition at some z_{cen} where a rigid cluster (a subset of particles with no floppy modes) percolates. Near z_{cen} vibrational modes are fractons [158, 159]. This model does not take into account that rigid regions cost energy, and thus corresponds to infinite temperature. To include these effects *self-organizing network models* were introduced [73, 75, 160, 161], where rigid regions are penalized. A surprising outcome of these models is the emergence of a rigidity window: a range of valence for which rigidity occurs with a probability $0 < p(z) < 1$, even in the thermodynamic limit. This rigidity window was proposed to correspond to the intermediate phase observed experimentally [73]. Finally, in the *mean-field or jamming scenario*, fluctuations of

coordinations are limited, and $p(z)$ jumps from 0 to 1 at z_c . The rigid cluster at z_c is not fractal, and is similar to that of packings of repulsive particles. Specific protocols to generate such networks were used to study elasticity [130, 131] as well as the thermodynamics and fragility of chalcogenides [116].

In this Letter we introduce an on-lattice model of networks, and study how structure and vibrational modes evolve under cooling. Unlike previous models supporting the existence of a rigidity window [75, 160], our model includes weak interactions (such as Van der Waals), always present in addition to covalent bonds. We show numerically and justify theoretically that the rigidity window is not robust: it disappears at low temperature as soon as weak interactions are added. At zero temperature the rigidity transition is then well described by the mean field scenario, and the vibrational modes consist of anomalous modes and not fractons.

3.2 Adaptive Elastic Network Model

Our model shares similarity to glasses of polydisperse particles, but it is on-lattice, and particles are replaced by springs. Specifically, in the spirit of [63] we consider a triangular lattice with slight periodic distortion to avoid straight lines (non-generic in disordered solids), as shown in Fig. 3.2. The lattice spacing between neighboring nodes i and j is $r_{\langle i,j \rangle} = 1 + \delta_{\langle i,j \rangle}$ where the periodic distortion $\delta_{\langle i,j \rangle}$ is specified in Appendix Sec. B.1. Springs of identical stiffness k can jump from an occupied to an unoccupied link, as shown in Fig. 3.2. Their number is controlled by fixing the coordination z . The rest length l_γ of the spring γ positioned on the link $\langle ij \rangle$ is $l_\gamma = r_{\langle i,j \rangle} + \epsilon_\gamma$, where ϵ_γ is taken from a Gaussian distribution of zero

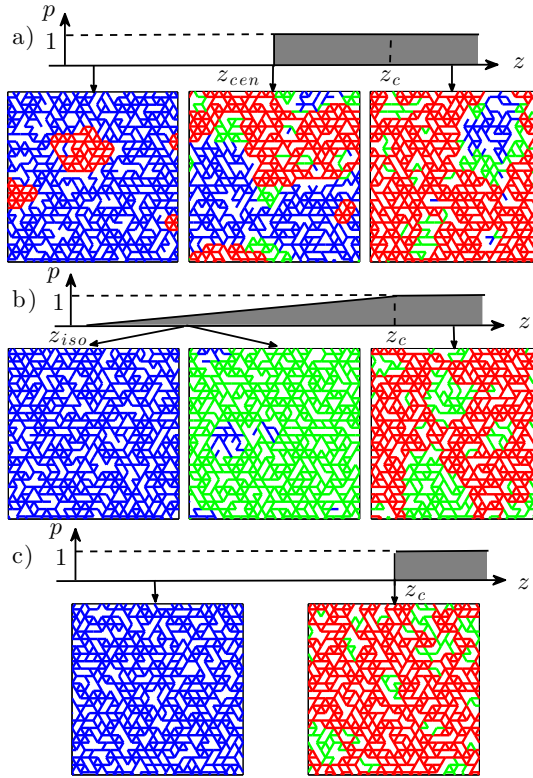


Figure 3.1: Three distinct scenarios for the rigidity transition in chalcogenide glasses. Bonds in blue, green, red corresponds respectively to floppy (under-constrained), isostatic (marginally-constrained) and over-constrained regions. $p(z)$ is the probability that a rigid cluster (made of green and red bonds) percolates, as a function of the valence z . (a) Rigidity percolation model where bonds are randomly deposited on a lattice. Percolation occurs suddenly and $p(z)$ jumps from 0 to 1 at $z_{cen} < z_c$. At z_{cen} , the rigid network is fractal. (b) The self-organizing network model at zero temperature. Over-constrained regions are penalized energetically and are absent for $z < z_z$. For $z \in [z_{iso}, z_c]$, $0 < p(z) < 1$ even in the thermodynamic limit. (c) Mean-field scenario, where $p(z)$ jumps from 0 to 1 at z_c , and where the rigid cluster at z_c is not fractal.

mean and variance ϵ^2 ¹. $k\epsilon^2$ is set to unity as the energy scale. To mimic Van der

¹The dependence of l_{ij} on link ij is a trick to remove the effect of straight lines on vibrational modes, unphysical for amorphous solids. In an elastic network it could be implemented in two dimensions by forcing the spring to bend in the third dimension, with a position-dependent

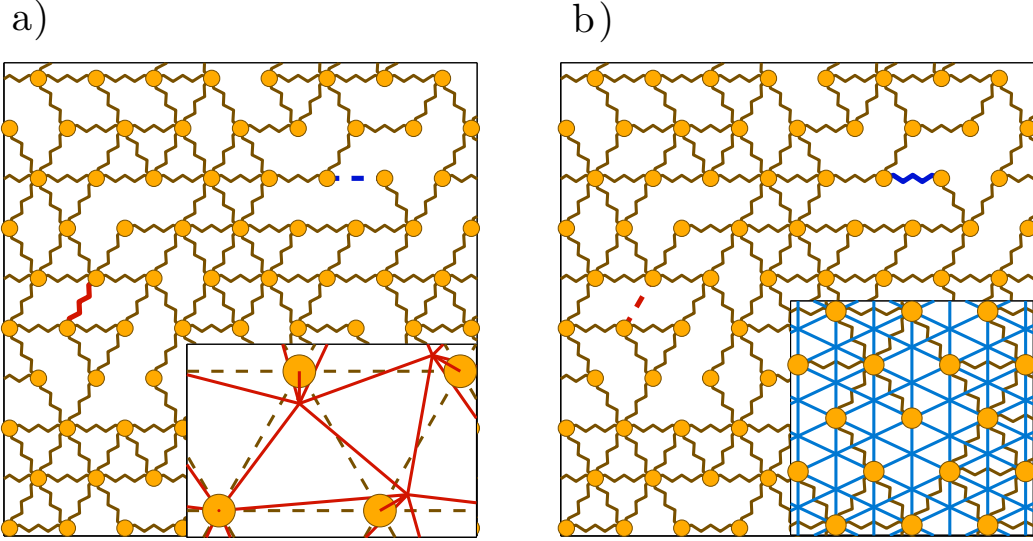


Figure 3.2: Illustration of our model. The triangular lattice is slightly distorted as shown in the inset of (a), and weak springs connecting all second neighbors are present, as shown in blue in the inset of (b). Our Monte-Carlo considers the motion of strong springs such as that leading from (a) to (b).

Waals interactions, we add weak springs of stiffness k_w between second neighbors, so that the coordination of weak springs is $z_w = 6$. For a given choice of spring location, indicated as $\Gamma \equiv \{\gamma \leftrightarrow \langle i, j \rangle\}$, forces are unbalanced if the positions of the nodes are fixed. Instead we allow the nodes to relax to a minimum of elastic energy $H(\Gamma)$, which depends only on the location of the springs Γ :

$$H(\Gamma) = \min_{\{\vec{R}_i\}} \sum_{\gamma} \frac{k}{2} \left[\|\vec{R}_i - \vec{R}_j\| - l_{\gamma} \right]^2 + \sum_{\langle i, j \rangle_2} \frac{k_w}{2} \left[\|\vec{R}_i - \vec{R}_j\| - \sqrt{3} \right]^2 \quad (3.1)$$

amount of bending.

where \vec{R}_i is the position of node i and $\langle i, j \rangle_2$ labels second neighbors. How the minimization of Eq.(3.1) is performed in practice is described in Appendix Sec. B.2. Having defined an energy functional on all possible network structures Γ , we perform a Monte Carlo simulation using Glauber dynamics (illustrated in Fig. 3.2) at temperature T .

Our model has two parameters: the temperature T and $\alpha \equiv (z_w/d)(k_w/k)$ characterizing the relative strength of the weak forces, estimated from experiments to be of order $\alpha = 0.03$ [116]. We find that we can equilibrate networks in the vicinity of the rigidity transition for $T \geq \alpha$. As we shall see below, for $T \gg 1$ we naturally recover rigidity percolation. When $\alpha = 0$ and $T \ll 1$, a rigidity window appears, as previously reported in [63, 73, 75, 162], which we exemplify below using $T = 3 \times 10^{-4}$ and $\alpha = 0$. We refer to this condition as *strong-force regime*. Finally, our main contention is that for $\alpha > 0$ and for $T \leq \alpha$, the rigidity window disappears, and the rigidity transition is mean-field. We show that this is already the case for extremely weak additional interactions $\alpha = T = 0.0003$, a condition we refer to as *weak-force regime*.

3.3 Numerical Proofs of the Mean-field Rigidity Transition

Percolation probabilities: the probability $p(z)$ to have a rigid cluster spanning the system, and the probability $P_\infty(z)$ for a bond to belong to this cluster are key quantities to distinguish scenarios. They can be computed for the network of strong springs using the Pebble Game algorithm [163]. For rigidity percolation and

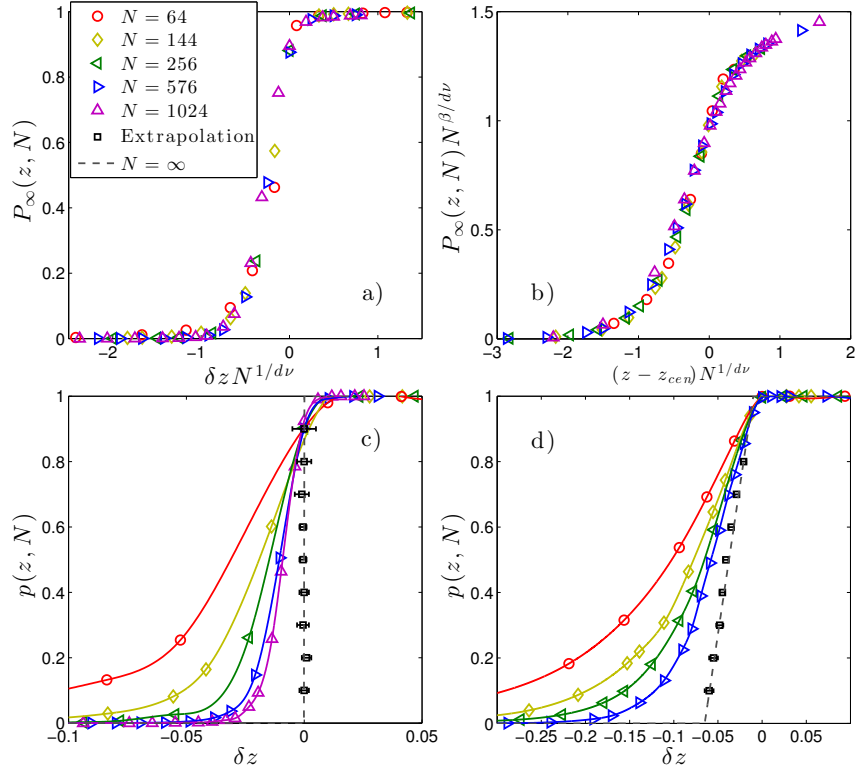


Figure 3.3: P_∞ vs $(z - z_c)N^{1/d\nu}$ in the *weak-force* condition (a) and for $T = \infty$ (b). p vs $\delta z \equiv z - z_c$ in the *weak-force* (c) and *strong-force* (d) conditions. The black squares are extrapolations of the finite N spline curves, as detailed in the main text. In (c), the gray line is a step function at $z = z_c$, whereas in (d) it corresponds to the result of [75].

infinite system size $N \rightarrow \infty$, $P_\infty(z) \sim (z - z_{cen})^\beta$. For finite N one then expects [164] $P_\infty(z, N) = N^{-\beta/d\nu} f_{RP}((z - z_{cen})N^{1/d\nu})$, where f_{RP} is a scaling function and ν the length scale exponent. As shown in Fig. 3.3(b), we recover this result for $T = \infty$, with $z_{cen} = z_c - 0.04$, $\beta = 0.17$ and $\nu = 1.3$, which perfectly matches previous works [165]. Here the Maxwell threshold is set to $z_c = 4 - 6/N$, as expected in two dimensions with periodic boundary conditions. In mean-field, the transition is discontinuous at z_c and one therefore expects $P_\infty(z, N) = f_J((z - z_c)N^{1/d\nu})$. Our first key evidence that the *weak-force regime* is mean-field is shown in Fig. 3.3(a),

where this collapse is satisfied with $\nu = 1.0$ - an exponent consistent with the prediction of [127].

Our second key evidence considers $p(z)$, which varies continuously [73, 75, 160] in the rigidity window scenario, but abruptly in mean-field, see Fig. 3.1. For finite size systems, it turns out to be easier to extract the inverse function $z(p)$, proceeding as follows. We first compute $p(z, N)$ for various z and N . For each N we use a spline interpolation to obtain continuous curves, as shown in Fig. 3.3(c,d). We then extract $z(p)$ by fitting the following correction to scaling $|z(p) - z(p, N)| \sim N^{-1/d\nu}$. Our central result is that for the *weak-force regime*, $p(z)$ discontinuously jumps from 0 to 1 at z_c (which simply corresponds to the crossing of the spline lines) as shown in Fig. 3.3(c), again supporting that the mean-field scenario applies. By contrast, in the *strong force regime* this procedure predicts a rigidity window for $z \in [z_c - 0.06, z_c]$. This result is essentially identical to previous work using much larger N [75] (which is impossible in our model).

Density of vibrational modes (DOS) $D(\omega, T)$: The DOS is a sensitive observable to characterize network structure. In the mean-field scenario, anomalous modes appear above a frequency $\omega^* \sim |z - z_c|$ [78, 127], above which the DOS displays a plateau: $D(\omega) \sim \omega^0$, as observed in packings [148]. By contrast, at rigidity percolation the rigid cluster is fractal and the spectrum consist of fractons, leading to $D(\omega) \sim \omega^{\tilde{d}-1}$ [158, 159], where \tilde{d} is the fracton dimension. Numerically we compute the DOS associated with the network of strong springs by diagonalization of the stiffness matrix. Within the rigidity window, we find that the DOS is insensitive to temperature for $\alpha = 0$ as shown in Fig. 3.4(a), supporting that normal modes are fractons in the rigidity window, with $\tilde{d} \approx 0.75$ [159]. By contrast,

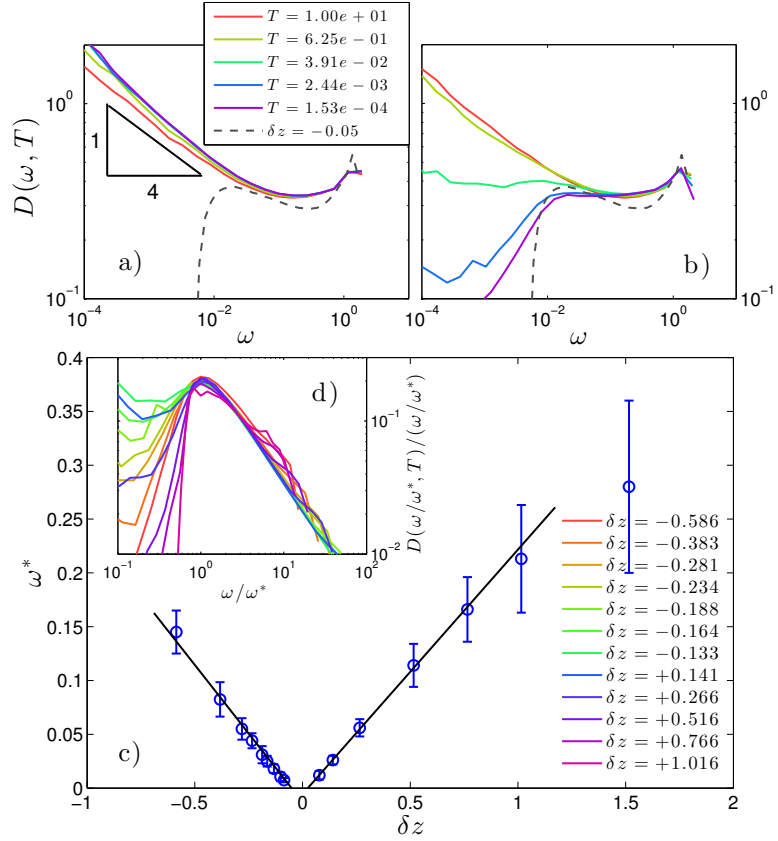


Figure 3.4: $D(\omega)$ at $z - z_c = -0.05$ and various T indicated in legend for (a) $\alpha = 0$ and (b) $\alpha = 0.0003$. Gray dashed lines are numerical solution of mean-field networks generated in [130]. (c) Boson peak frequency ω^* vs coordination z for the *weak-interaction* regime. ω^* is defined as the peak frequency of $D(\omega)/\omega^{d-1}$, a quantity shown in (d).

already at small $\alpha = 0.0003$, a key observation is that the DOS evolves under cooling toward the mean-field prediction, as illustrated in Fig. 3.4(b). At low-temperature, one recovers a frequency scale $\omega^* \sim |z - z_c|$ as shown in Fig. 3.4(c,d), supporting further that the mean-field scenario applies. Note that there is a very narrow region around z_c where the mean-field prediction does not work well and instead one finds $\omega^* \approx 0$ (see discussion below).

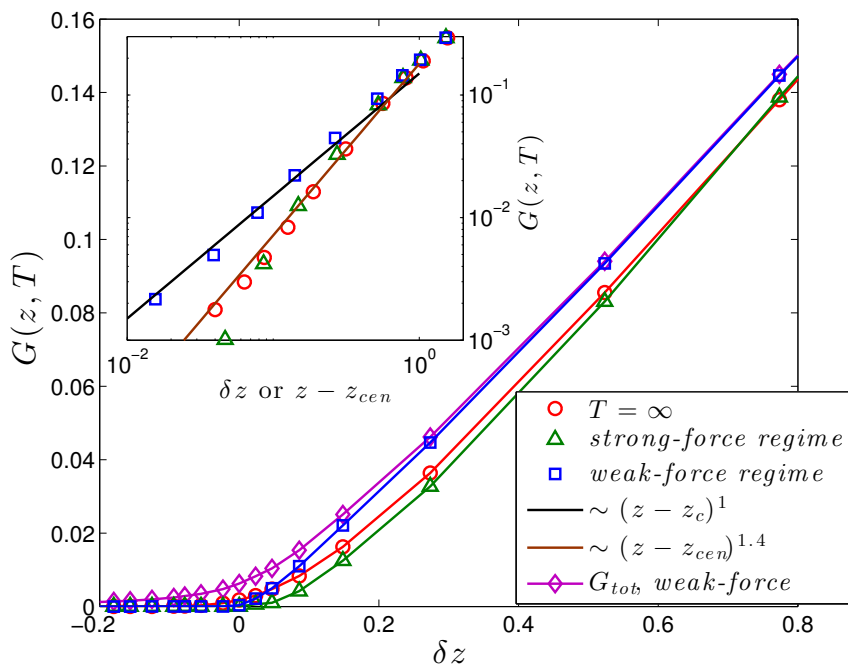


Figure 3.5: Shear modulus of the strong network G vs $\delta z \equiv z - z_c$ for parameters indicated in legend. The total shear modulus G_{tot} including the effect of weak springs is represented for the *weak-interaction regime*. Inset: same plot in log-log scale, the horizontal axis is $z - z_c$ for low-temperatures conditions (blue and green), and $z - z_{cen}$ at $T = \infty$ (red).

Shear modulus $G(z)$: Lastly, we compute the shear modulus for the strong network numerically, as shown in Fig. 3.5. As expected, we find for $T = \infty$ the rigidity percolation result $G(z) \sim (z - z_{cen})^f$, with $f \approx 1.4$ [166]. In the *weak-interaction regime*, we find that the mean-field result [152] $G(z) \sim \delta z$ holds, supporting further our main claim. In the strong interaction regime, we find that the shear modulus is zero up to z_c . However no power law scaling is found near z_c , and G is much lower than in mean-field, in agreement once again with previous models that observed a window [167].

3.4 A Simple Argument for the Mean-field Scenario

We have shown numerically that the *weak interaction regime* is well-described by the mean-field scenario. To explain this fact, we argue that this scenario is stable if $\alpha > 0$, but unstable if $\alpha = 0$. Consider the elastic energy per unit volume E_p . Qualitatively this quantity is expected to behave as $E_p \sim G_{tot}\epsilon^2$, where G_{tot} is the total shear modulus that includes weak interactions, also shown in Fig. 3.5. The central point is that in mean-field, if $\alpha = 0$ then $E_p(z)$ linearly grows for $z > z_c$ and is strictly 0 for $z < z_c$. It implies that there is no penalty for increasing spatial fluctuations of coordination as long as $z < z_c$ locally. Thus large fluctuations of coordination are expected, the mean-field scenario is not stable and one finds a rigidity window instead. By contrast, $E_p(z)$ is strictly convex for all z as soon as $\alpha > 0$. Then spatial fluctuations of coordination are penalized energetically, and they disappear at low T . In Appendix Sec. B.3., Fig. C.1, we find numerically that in our model, fluctuations of coordination indeed decay under cooling only if $\alpha > 0$.

It is apparent from Fig. S2 that this process of homogenization is already playing a role at temperatures of order $T \sim 10\alpha$. In practice the glass transition T_g is of order α (the typical covalent bond energy is between 1 and 10eV, Van der Waals interactions are of between 0.01 and 0.1eV, and the glass transition temperature T_g is of order 100 to 1000K, which is about 0.01 to 0.1eV), supporting that spatial fluctuations of coordination are strongly tamed due to the presence of weak interactions in real covalent glasses.

To conclude, we have argued that weak interactions induce a finite cost to spatial fluctuations of coordination, which therefore vanish with temperature. As a consequence, the rigidity transition is mean-field in character, if equilibrium can be achieved up to $T = 0$. In this light, the mean-field scenario is a convenient starting point to describe these materials. Note that although we focussed on $d = 2$, our arguments go through unchanged in $d = 3$, where the order of the rigidity percolation transition appears to be non-universal [168].

However, as T increases fluctuations must be included in the description, as appears in Fig. 3.4(b). Since covalent networks freeze at some $T_g > 0$, one still expects a finite amount of fluctuations in the glass phase. Indeed one must cross-over from rigidity percolation at $T = \infty$ to a mean-field scenario at $T = 0$. We shall investigate this cross-over in detail elsewhere, and instead speculate on its nature here. We expect this cross-over to be continuous, implying that at any finite temperature, there is a narrow region around z_c where fluctuations still play a role, and where the transition lies in the rigidity percolation universality class. The size of this region vanishes with vanishing temperature but is finite at T_g . Inside this region, one expects the boson peak to be dominated by fractons, whereas outside the mean-field approximation holds and anomalous modes dominate the spectrum. Fig. 3.4(c) supports this view since already at the very low-temperature considered, there is a narrow region for which $\omega^* \approx 0$, at odds with the mean-field prediction. As expected, this effect is stronger as T_g increases (as occurs in our model when α increases), as illustrated in Fig. C.4 of Appendix Sec. B.4. This qualitative difference in elasticity is likely to affect thermodynamic and aging properties near the glass transition, since these properties are known to be strongly coupled [34, 116]. The region surrounding the rigidity transition where fluctuations

are important is thus a plausible candidate for the intermediate phase observed in chalcogenides, which would then result from a dynamical effect, namely the freezing of fluctuations at the glass transition.

Chapter 4

Adaptive Elastic Networks as Models of Supercooled Liquids

The thermodynamics and dynamics of supercooled liquids correlate with their elasticity. In particular for covalent networks, the jump of specific heat is small and the liquid is *strong* near the threshold valence where the network acquires rigidity. By contrast, the jump of specific heat and the fragility are large away from this threshold valence. In a previous work [Proc. Natl. Acad. Sci. U.S.A., 110, 6307 (2013)], we could explain these behaviors by introducing a model of supercooled liquids in which local rearrangements interact via elasticity. However, in that model the disorder characterizing elasticity was frozen, whereas it is itself a dynamic variable in supercooled liquids. Here we study numerically and theoretically adaptive elastic network models where polydisperse springs can move on a lattice, thus allowing for the geometry of the elastic network to fluctuate and evolve with temperature. We show numerically that our previous results

on the relationship between structure and thermodynamics hold in these models. We introduce an approximation where redundant constraints (highly coordinated regions where the frustration is large) are treated as an ideal gas, leading to analytical predictions that are accurate in the range of parameters relevant for real materials. Overall, these results lead to a description of supercooled liquids, in which the distance to the rigidity transition controls the number of directions in phase space that cost energy and the specific heat.

4.1 Introduction

Liquids undergo a glass transition toward an amorphous solid state when cooled rapidly enough to avoid crystallization [2]. The glass lacks structural order: it is a liquid “frozen” in a local minimum in the energy landscape, due to the slowing down of relaxation processes. It is very plausible that the thermodynamics and the dynamics in supercooled liquids strongly depend on the microscopic structure of these configurations – hereafter referred to as “inherent structures” [169]. However, a majority of glass theories [21, 28, 29, 121, 170–172] have focused on explaining the correlations between macroscopic observables seen in experiments (such as the relationship between thermodynamics and dynamics [5, 27]), while only a few [31, 32, 173, 174] have investigated the role of structure.

Experiments reveal that elasticity plays a key role in both the thermodynamic and dynamical properties in supercooled liquids, such as the jump of specific heat and the fragility characterizing the glass transition. Specifically, it has been found that (I) glasses present an excess of low-frequency vibrational modes with

respect to Debye modes. The number of these excess anomalous modes, quantified as the intensity of the boson peak [123], shows a strong anti-correlation with the fragility [33, 34]. (II) The rigidity of the inherent structures is tunable by changing the fraction of components with different valences in network glasses [35, 42, 125], where atoms interact via covalent bonds and much weaker Van der Waals force. The covalent network becomes rigid [39–41], when the average valence r exceeds a threshold r_c , determined by the balance between the number of covalent constraints and the degrees of freedom of the system. Both the fragility and the jump of specific heat depend nonmonotonically on r , and their minima coincide with r_c [4, 35]. Interesting works using density functional theory [31, 175] investigated the relationship between structure and fragility, but they do not capture this nonmonotonicity.

Recent observations [47, 50–53] and theory [54–58, 128, 129, 150, 173, 176] indicate that in various amorphous materials, the presence of soft elastic modes is regulated by the proximity of the rigidity transition, linking evidence (I) and (II). To rationalize this connection, we have introduced a frozen elastic network model that bridges the gap between network elasticity and geometry on one hand, elasticity and the thermodynamics and dynamics of liquids on the other [116]. This model incorporated the following aspects of supercooled liquids: (*i*) particles interact with each other with interactions that can greatly differ in strength, such as the covalent bonds and the much weaker Van der Waals interaction found in network glasses. (*ii*) Neighboring particles can organize into a few distinct local configurations. (*iii*) The choices of local configurations are coupled at different location in space via elasticity. These features were modeled using a random elastic network whose topology was frozen, as illustrated in Fig. 4.2. The possibility

for local configurations to change was incorporated by letting each spring switch between two possible rest lengths. Despite its simplicity, this model recovered (I) and (II). In particular, it reproduced the nonmonotonic variance of the jump of specific heat and the fragility with the coordination z of the network: they are extremal at $z_c = 2d$ (d is the spatial dimension), where a rigidity transition occurs. This model could be solved analytically, and it led to the view that near the rigidity transition, the jump of specific heat is small because frustration vanishes: most directions in phase space do not cost energy, and thus do not contribute to the specific heat.

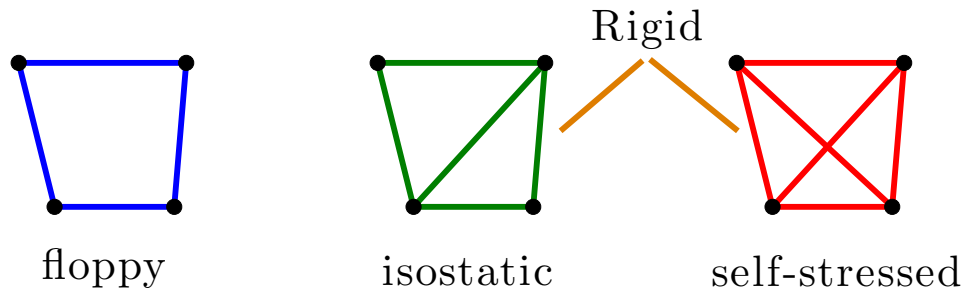


Figure 4.1: Illustration of rigidity transition. Blue, green, and red color the floppy, isostatic, and stressed clusters, respectively.

This is a novel explanation for a long-standing problem, and it is important to confirm that this view is robust when more realism is brought into the model. In particular, the model used frozen disorder to describe elasticity, whereas it is itself a dynamical property in liquids, where there cannot be any frozen disorder. The thermal evolution of the topology of the contact network and its effects on rigidity transition were also not addressed. A network is rigid when an imposed global strain induces stress, and the rigidity can be achieved topologically by adding constraints [39], see Fig. 4.1 for an illustration in a small network.

The network is said to be self-stressed if some of the constraints are redundant, removing those leaves the network rigid. Three scenarios of rigidity transition have been extensively studied in the literature [117, 177] (but see Ref. [155] for a recent fourth proposition). Spatial fluctuations of coordination are important in the first two. The *rigidity percolation* model [63, 68, 156, 157] assumes that bonds are randomly deposited on a lattice. Fluctuations lead to over-constrained (self-stressed) clusters even when the average coordination number is not sufficient to make the whole network rigid. This model corresponds to the infinite temperature limit. To include these effects, self-organized network models were introduced [73, 75, 160, 161], where overconstrained regions are penalized. A surprising outcome of these models is the emergence of a rigidity window: rigidity emerges at a small coordination number before the self-stress appears (even in the thermodynamic limit). Finally, in the *mean-field or jamming scenario*, fluctuations of coordinations are limited. Similar to the simple picture in Fig. 4.1, the rigidity, and the stress appear at the same z_c in the thermodynamic limit. The rigid cluster at z_c is not fractal and is similar to that of packings of repulsive particles. The model of Ref. [116] assumed that networks were of this last type.

Recently, we have introduced adaptive elastic network models [117], where the topology of the network is free to evolve to lower its elastic energy as the system is cooled. We found that as soon as weak interactions are present, the network of strong interactions becomes mean-field like at low temperature. However, the thermodynamic properties were not studied to test the robustness of the thermodynamic predictions of Ref. [116] relating structure to the jump of specific heat. In this work, we directly show numerically and theoretically that the prediction for the jump of specific heat is essentially identical in adaptive and frozen elastic

network models. Section II describes the adaptive network models. Section III presents the numerical results of the model, while Section IV gives the explicit derivation of the thermodynamic properties, developing an approximation scheme to deal with the temperature-dependence of the number of over-constraints in the system, treating them as an ideal gas.

4.2 Adaptive Network Model

In our model degrees of freedom are springs, which are poly-disperse and can move on a lattice. The lattice is built using a triangular lattice with periodic boundary conditions, see Fig. 4.2(c), with a slight regular distortion to minimize the non-generic presence of zero modes that occurs when straight lines are present, as illustrated in the inset of Fig. 4.2(c). Polydisperse and mobile “strong” springs of identical stiffness k connect the nearest neighbors on the lattice and model the covalent constraints. We model weak Van der Waals interactions with “weak” and stationary springs of stiffness $k_w \ll k$ adding to all next-nearest-neighbors on the triangular lattice, illustrated in Fig. 4.2(b). We introduce a control parameter $\alpha \equiv (z_w/d)(k_w/k)$ to characterize the relative strength of the weak interactions, where the spatial dimension is $d = 2$ and the number of weak constraints per node is chosen $z_w = 6$.

The number of “covalent” springs N_s , equivalent to the coordination number $z \equiv 2N_s/N$ (N is the number of nodes in the lattice), is also a dimensionless control parameter. For a given $\delta z \equiv z - z_c$, the valid configurations are defined by the locations of the N_s springs, indicated as $\Gamma \equiv \{\gamma \leftrightarrow \langle i, j \rangle\}$, where the Greek

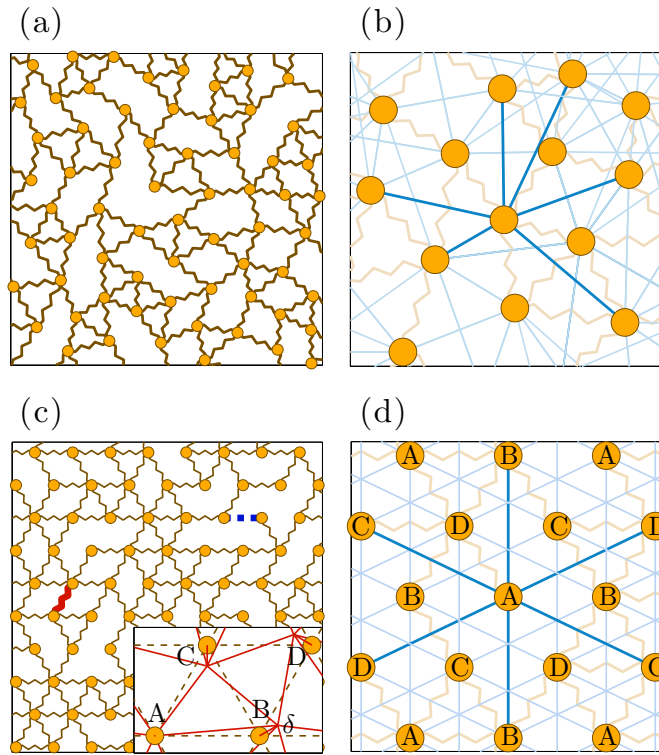


Figure 4.2: (Color online) (a) and (b) Illustration of the frozen network model [116]; (c) and (d) illustrate the adaptive network model [117]. In the latter case, the triangular lattice is systematically distorted in a unit cell of four nodes shown in the inset of (c). We group nodes by four, labeled as, A, B, C, and D in Fig. 4.2. One group forms the unit cell of the crystalline lattice. Each cell is distorted identically in the following way: node A stays, while nodes B, C, and D move by a distance δ , B along the direction perpendicular to BC, C along the direction perpendicular to CD, and D along the direction perpendicular to DB. δ is set to 0.2 with the lattice constant as unity. Weak springs connecting (b) six nearest neighbors without strong springs and (d) six next-nearest-neighbors are indicated in straight cyan lines, emphasized for the central node. (c) Illustration of an allowed step, where the strong spring in red relocates to a vacant edge indicated by a dashed blue line.

index γ labels springs and the Roman indices $\langle i, j \rangle$ label the edges on triangular lattice between nodes i and j . We introduce the occupation of an edge: $\sigma_{\langle i, j \rangle} = 0$ if there is no strong spring on the edge ij , and $\sigma_{\langle i, j \rangle} = 1$ if there is one. If $r_{\langle i, j \rangle}$ denotes the geometric length between nodes i and j on the lattice, we assume that the spring γ has a rest length $l_\gamma = r_{\langle i, j \rangle} + \epsilon_\gamma$, where the mismatch ϵ_γ is a feature of a given spring. ϵ_γ are sampled independently from a Gaussian distribution with mean zero and variance ϵ^2 , which thus characterizes the polydispersity of the model. $k\epsilon^2$ is set to unity as the natural energy scale.

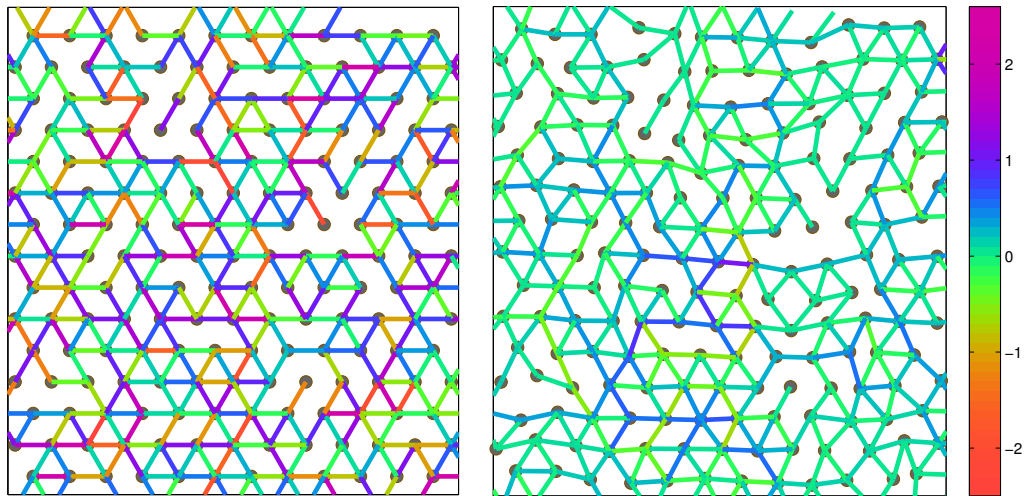


Figure 4.3: (Color online) Illustration of configuration energy of the adaptive network model ($\delta z = 0.27$). Solid lines are springs, colored according to their extensions: from red to purple, the springs go from being stretched to being compressed, with spring extensions shown in the unit of ϵ . Left: Nodes sit at lattice sites, so the color shows the rest length mismatches of the springs $\{\epsilon_\gamma\}$. Right: Nodes are relaxed to mechanical equilibrium. Most links appear in green, indicating that most of the elastic energy is released. The configuration energy is defined by the residual energy.

The energy of an inherent structure is denoted $\mathcal{H}(\Gamma)$. The configuration

Γ is sampled with probability proportional to $\exp(-\mathcal{H}(\Gamma)/T)$ in the liquid phase, with $k_B = 1$. Temperature T serves as a third dimensionless control parameter. $\mathcal{H}(\Gamma)$ is defined as the remaining energy once the nodes of the network are allowed to relax to mechanical equilibrium:

$$\mathcal{H}(\Gamma) = \min_{\{\vec{R}_i\}} \left\{ \sum_{\gamma} \frac{k}{2} \left[\|\vec{R}_i - \vec{R}_j\| - l_{\gamma} \right]^2 + \sum_{\langle i,j \rangle_2} \frac{k_w}{2} \left[\|\vec{R}_i - \vec{R}_j\| - r_{\langle i,j \rangle_2} \right]^2 \right\} \quad (4.1)$$

where \vec{R}_i is the position of particle i and $\langle i, j \rangle_2$ labels the next-nearest neighbors. The minimal energy can be calculated by steepest decent as illustrated in Fig. 4.3, but this is computationally expensive. Instead, we approximate the elastic energy in the linear response range, setting that $\epsilon^2 \ll 1$ ¹. The above minimization expression Eq.(4.1) could then be written as,

$$\mathcal{H}(\Gamma) = \frac{k}{2} \sum_{\Gamma} \epsilon_{\langle i,j \rangle} \mathcal{G}_{\langle i,j \rangle, \langle l,m \rangle} \epsilon_{\langle l,m \rangle} + o(\epsilon^3) \quad (4.2)$$

where $\epsilon_{\langle i,j \rangle} = \epsilon_{\gamma}$ when spring γ connects i and j . The coupling matrix $\mathcal{G} = \mathcal{P} - \mathcal{S}(\mathcal{S}^t \mathcal{S} + \frac{k_w}{k} \mathcal{S}_w^t \mathcal{S}_w)^{-1} \mathcal{S}^t$, derived in our previous works [116, 117] (or see Appendix Sec. C.1), is a product of the structure matrix \mathcal{S} and its transpose \mathcal{S}^t , the structure matrix of the weak spring network \mathcal{S}_w , and \mathcal{P} the projection operator of the triangular lattice onto occupied edges. The structure matrices \mathcal{S} and \mathcal{S}_w describe the topology of the networks of strong and weak springs: if neighbor nodes i and j are connected, the change of the distance between i and j , $\delta r_{\langle i,j \rangle} = \mathcal{S}_{\langle i,j \rangle, i} \cdot \delta \vec{R}_i + \mathcal{S}_{\langle i,j \rangle, j} \cdot \delta \vec{R}_j + o(\delta \vec{R}^2)$, due to displacements of nodes $\delta \vec{R}$. We point out that as the weak network is fixed, \mathcal{S} and thus \mathcal{G} depend only on the

¹We have tested the validity of the linear approximation: the energy difference from the steepest decent results keeps below 3% for $\epsilon < 0.02$.

network topology of strong springs, but not on the mismatches ϵ_γ .

Our model is a generalization of on-lattice network models: setting the interaction strength control parameter $\alpha = 0$, it naturally recovers the randomly diluted lattice model [63] when $T = \infty$. It is also related to the self-organized lattice model [73, 75], which postulates that elastic energy is linearly proportional to the number of redundant constraints [73, 178]. We will find that this assumption holds true for $\alpha = 0$ and $T \ll 1$. However, the existence of weak interactions among sites means that in real physical systems $\alpha > 0$. This turns out to completely change the physics, an effect that our model can incorporate.

4.3 Numerical Results of the Model

We implement a Monte Carlo simulation to sample the configuration space of the model, with 10^6 Monte Carlo steps at each T . At each step, a potential configuration is generated by a Glauber dynamics - moving one randomly chosen spring to a vacant edge, as illustrated in Fig. 4.2(c). We numerically compute the elastic energy of the proposed configuration using Eq.(4.2): calculating the structure matrix \mathcal{S} and then the corresponding \mathcal{G} . On computing \mathcal{G} , the matrix inversion, $(\mathcal{S}^t \mathcal{S} + \frac{k_w}{k} \mathcal{S}_w^t \mathcal{S}_w)^{-1}$, is singular when the network contains floppy structures, which do not appear except when $k_w = 0$. When $\alpha = 0$, we implement the “pebble game” algorithm [163] to identify the over-constrained sub-networks, and then do matrix division in the subspace, as the isostatic and floppy regions store no elastic energy after relaxation. We have found little finite size effect by varying the system size from $N = 64$ to $N = 1024$ nodes in the triangular lattice. In the following, we

present our numerical results of networks with $N = 256$ nodes, averaged over 50 realizations of random mismatches if not specified.

4.3.1 Dynamics

We investigate the dynamics by computing the correlation function $C(t) = \frac{1}{N_s(1-N_s/3N)}(\langle \sigma(t)|\sigma(0) \rangle - N_s^2/3N)$, where $|\sigma(t)\rangle$ is the vector indicating the occupation of all edges at time t . The correlation $C(t)$ decays from one to zero at long time scales. We define the relaxation time τ as the time $C(\tau) = 1/2$, and the numerical results of τ as a function of temperature T for several different coordination numbers are shown in the Fig. 4.4.

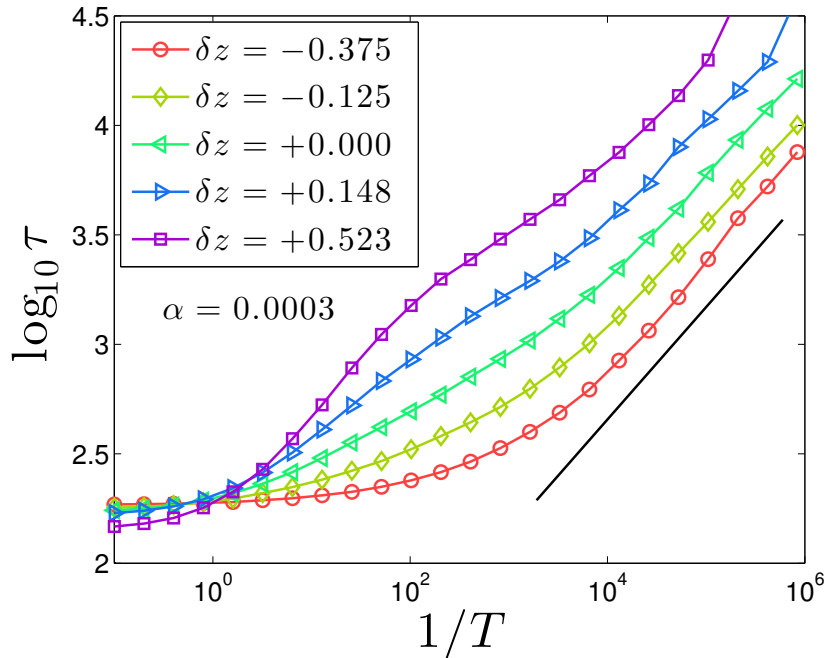


Figure 4.4: (Color online) Relaxation time τ in log-scale versus inverse temperature $1/T$ for different coordination numbers δz and $\alpha = 0.0003$. The solid black line indicates a power law relation between τ and T : $\tau \sim T^{-1/2}$.

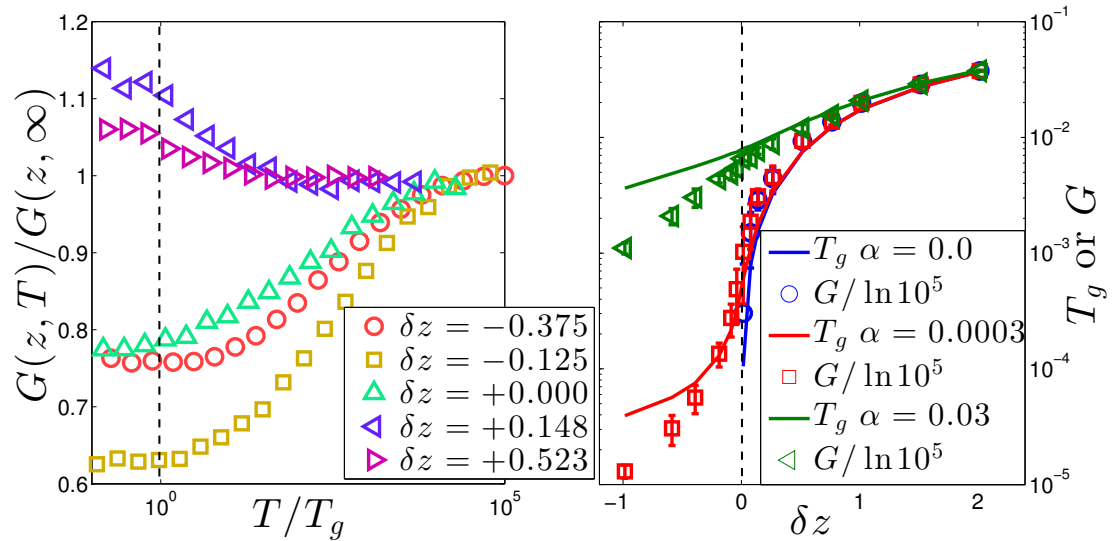


Figure 4.5: (Color online) Left: Shear modulus of adaptive networks at temperature T rescaled by G at $T = \infty$ $G(z, T)/G(z, \infty)$, $\alpha = 0.0003$. The temperature T is rescaled by T_g . Right: Correlation between transition temperature T_g and shear modulus G in the frozen network model [116].

We find that the implemented dynamics is not glassy. The relaxation time increases as a power law of the temperature $T^{-0.5}$, even much slower than a strong glass that would display an Arrhenius behavior $\log_{10} \tau \propto 1/T$. This result is very surprising because the frozen elastic network model we studied earlier was glassy (its fragility was similar to that of network liquids). Despite being dynamically very different, these two models are almost identical as far as thermodynamics is concerned, as we will see below. It could be that the lack of glassiness comes from our choice of Monte-Carlo where springs can try other locations anywhere in the system [179].

To compare the thermodynamics of these models we now need to define an effective glass temperature T_g (even if we do not see a real glass transition).

We do that by using the empirical Lindemann criterion [180] according to which an amorphous solid melts when the standard deviation $\langle \delta R^2 \rangle^{1/2}$ of particles' displacements is greater than a fraction c_L of the particle size a . The coefficient c_L must depend on the quench rate q , since this is also the case for T_g . This dependence is logarithmic, because the dependence of relaxation time on temperature in experimental glass formers is at least exponential (for typical experimental quench rate in supercooled liquids, $c_L \approx 0.15$ [181]). We can estimate this standard deviation via the elastic modulus if we treat the glass as a continuum $\langle \delta R^2 \rangle \sim T/Ga$ where G is the instantaneous shear modulus of the structure [171], we thus get $T_g \propto Ga^3/\ln(1/q)$. We set the lattice length a in our model to unity.

We measure the shear modulus averaging over configurations at given temperatures, shown in the left panel of Fig. 4.5. Practically, we choose $T_g = \langle G \rangle_{T_g} / \ln(1/10^3 q)$, where the cooling rate q is defined as the inverse of the number of Monte Carlo steps performed at each temperature in the model. $\langle \bullet \rangle_{T_g}$ is the mean value at temperature T_g . The prefactor in this definition of T_g does not affect qualitatively our conclusions, but for this pre-factor the definition of T_g in the frozen model [116] is essentially identical to the dynamical definition used in [116], as shown in the right panel of Fig. 4.5 by lining up G and T_g . The specific values of T_g following that definition are shown in the inset of the bottom panel of Fig. 4.7, they correspond to $T_g = \langle G \rangle_{T_g} / \ln(10^3)$ in the present model, and $T_g = \langle G \rangle_{T_g} / \ln(10^5)$ in the frozen network model [116], which is simpler to simulate and can thus be equilibrated longer.

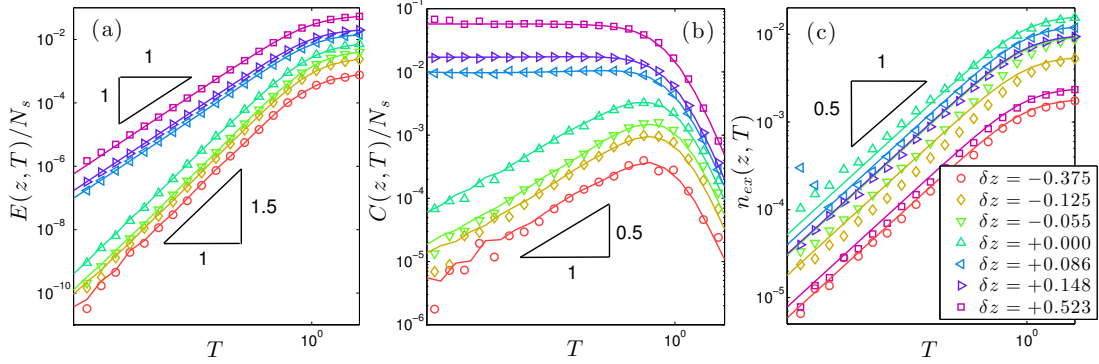


Figure 4.6: (Color online) Thermodynamics of the adaptive network model without weak constraints $\alpha = 0$. (a) Energy E/N_s vs. temperature; (b) specific heat C/N_s vs. temperature; (c) excess number density of redundant constraints n_{ex} extracted using the pebble game algorithm vs. temperature. Symbols are numerical data; solid lines are theoretic predictions.

4.3.2 Specific heat

The specific heat data shown in Figs. 4.6 and 4.7 are our central numerical results. The energy $E = \langle \mathcal{H} \rangle$ is obtained using a time-average over Monte Carlo steps, and is shown in Fig. 4.6(a). The specific heat is calculated as its derivative $c \equiv \frac{1}{N_s} dE/dT$, and is shown versus T for several coordination numbers when $\alpha = 0$ in Fig. 4.6(b) and $\alpha = 0.0003$ in the top panel of Fig. 4.7. When $\alpha = 0$, the specific heat increases as temperature decreases for networks with $\delta z > 0$ while it meets a maximum at $T_a \sim 1$ and decreases under cooling when $T < T_a$ if $\delta z \leq 0$. By contrast, the specific heat increases under cooling close to the transition temperature for all coordination numbers when $\alpha > 0$. In addition, when $T \lesssim \alpha$, $c \rightarrow 0.5$. All these results are qualitatively identical to our previous frozen model.

To define the jump of the specific heat at the glass transition, we simply

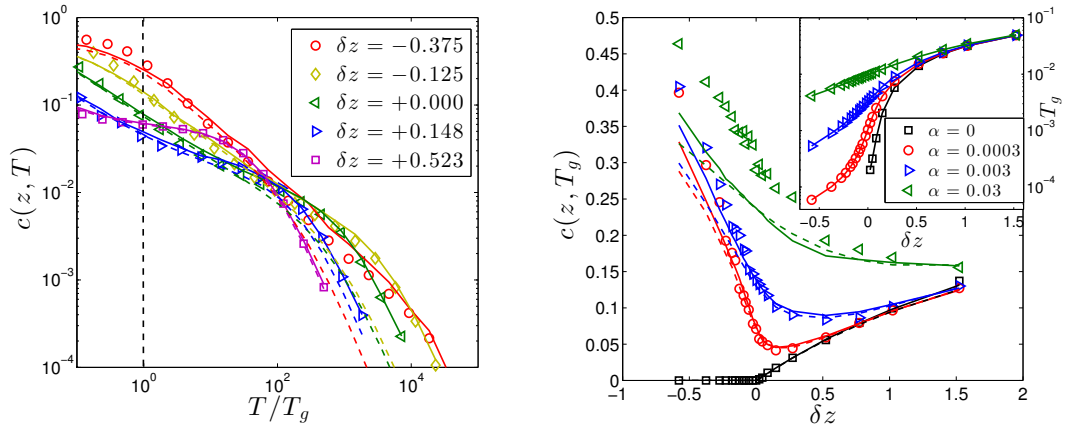


Figure 4.7: (Color online) Top: Specific heat $c(z, T)$ vs scaled temperature T/T_g for networks with average coordination numbers near and away from the isostatic on both floppy and rigid sides. The strength of the weak constraints is given by $\alpha = 0.0003$. Bottom: Specific heat at temperature T_g , $c(z, T_g)$, vs coordination number δz for $\alpha = 0, 0.0003, 0.003, 0.03$. The inset shows the transition temperature T_g for different z and α . Symbols are numerical results, and lines are theoretical predictions: dashed lines are for frozen network model and solid lines are for the new model derived in section IV.

measure the specific heat at our glass transition T_g defined above. This definition is natural, since in a real glassy system, below T_g the liquid is essentially frozen in an inherent structure, and the contribution to the specific heat from configurational entropy (i.e. the bottom energy of inherent structures) vanishes.

Our central numerical result is shown in the bottom panel of Fig. 4.7: $c(T_g)$ varies nonmonotonically with the coordination number z when $\alpha > 0$. When the network of strong springs is poorly coordinated $\delta z \lesssim 0$, $c(T_g)$ decreases as z increases; When the strong network gets better coordinated $\delta z \gtrsim 0$, c gradually changes to increase with z ; c is minimal at the proximity of the rigidity transition z_c for finite α . These numerical results are very similar to empirical observations,

see Point (II) in the introduction. Our data are in fact very similar to that of the frozen model, which essentially follows the dotted lines in Fig. 4.7.

4.3.3 Number of redundant constraints R

When $\alpha = 0$ and $T \rightarrow 0$, the specific heat is simply proportional to R , as shown in Fig. 4.6(b). This number is fixed, $R = N\delta z/2$, in the frozen network models. It varies in the adaptive network model and depends on the temperature. As the Maxwell counting gives the minimal number of redundant constraints of a network, we can define an excess number of redundant constraints

$$n_{\text{ex}} \equiv \frac{1}{N_s} \left(R - \frac{N\delta z}{2} \Theta(\delta z) \right), \quad (4.3)$$

where $\Theta(x)$ is the Heaviside step function. n_{ex} counts the average number of redundant constraints, additional to the Maxwell counting. This excess number of redundant constraints decreases monotonically to zero under cooling. When $\alpha = 0$, n_{ex} is proportional to \sqrt{T} in the adaptive network model at low temperature, shown in Fig. 4.6(c).

4.4 Theory of Thermodynamics

As illustrated in Fig. 4.8, in the frozen elastic model we found that as $\alpha \rightarrow 0$, c converges to a constant if $z < z_c$, whereas it behaves as $z - z_c$ for $z > z_c$. As α is increased, the discontinuous behavior becomes smooth and looks similar to experimental data. We seek to derive these same features in the adaptive network

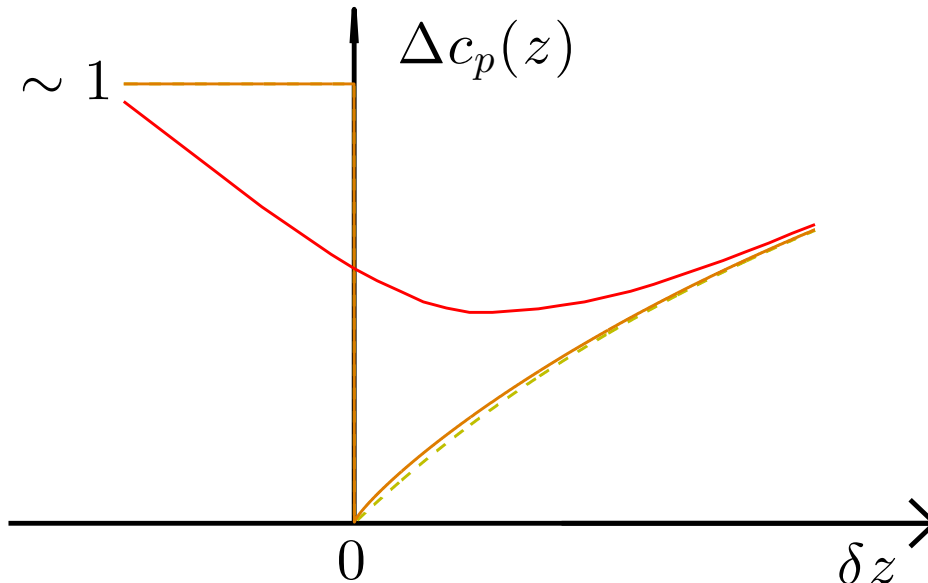


Figure 4.8: (Color online) Theoretical predictions for the jump of specific heat. For vanishingly weak springs $\alpha \rightarrow 0$, it is predicted that the jump is essentially constant for $z < z_c$ and then drops to zero at z_c . For larger z , it behaves as $z - z_c$. As α grows this sharp curve becomes smooth, but a minimum is still present near $z = z_c$.

models.

4.4.1 Partition function

For simplicity, we consider the annealed free energy $\mathcal{F}_{\text{ann}} = -T \ln \bar{\mathcal{Z}}$. It is exact in the random energy model [136] above the ideal glass transition [182] and we find it to be a good approximation of $\bar{\mathcal{F}}$ in our models [116]. The over-line implies an average over disorder ϵ ,

$$\bar{\mathcal{Z}} = \overline{\sum_{\{\sigma\}} \sum_{\text{perm}[\gamma]} \exp[-\mathcal{H}(\Gamma)/T]} \quad (4.4)$$

where a given configuration Γ is characterized by $\{\sigma\}$ indicating which edges are occupied on the triangular lattice, and $\text{perm}[\gamma]$ labels the possible permutations of springs' rest lengths.

We first average over the quenched randomnesses. Using the linear approximation Eq.(4.2) and the Gaussian distribution $\rho(\epsilon_\gamma) = \frac{1}{\sqrt{2\pi\epsilon^2}} e^{-\epsilon_\gamma^2/2\epsilon^2}$,

$$\bar{Z} = \sum_{\{\sigma\}} \left(\frac{Nz}{2}\right)! \exp\left[-\frac{1}{2} \text{tr} \ln \left(\mathcal{I} + \frac{\mathcal{G}(\{\sigma\})}{T}\right)\right] \quad (4.5)$$

The factorial comes from $N_s! = \sum_{\text{perm}[\gamma]} \mathbf{1}$ as \mathcal{G} is independent of the permutation. \mathcal{I} is a $3N \times 3N$ identity matrix; each component corresponds to an edge on the lattice. To compute the trace in the exponent, we first make the approximation that the weak springs are weak and numerous $\mathcal{S}_w^t \mathcal{S}_w \approx \frac{z_w}{d} \mathcal{I}_{Nd \times Nd}$, which corresponds to the highly connected limit $z_w \rightarrow \infty$ and finite α . We can then decompose the coupling matrix $\mathcal{G} \approx \mathcal{P} - \mathcal{S}(\mathcal{S}^t \mathcal{S} + \alpha \mathcal{I})^{-1} \mathcal{S}^t$ as [116]:

$$\mathcal{G}(\{\sigma\}) = \sum_{p(\{\sigma\})} |\psi_p\rangle \langle \psi_p| + \sum_{\omega(\{\sigma\}) > 0} \frac{\alpha}{\omega^2 + \alpha} |\psi_\omega\rangle \langle \psi_\omega| \quad (4.6)$$

where p labels the vectors $|\psi_p\rangle$ satisfying $\mathcal{S}^t |\psi_p\rangle = 0$ (i.e. a basis for the kernel of \mathcal{S}^t), and where the $|\psi_\omega\rangle$ satisfy $\mathcal{S} \mathcal{S}^t |\psi_\omega\rangle = \omega^2 |\psi_\omega\rangle$. The number of redundant directions is $\sum_p \mathbf{1} = N_s - (Nd - F) \equiv R$. Note that $\text{tr} \mathcal{P} = N_s$, $Nd - F$ gives the number of frequencies ω , and F counts the number of floppy modes. The modes $|\psi_p\rangle$, $|\psi_\omega\rangle$, R , and ω depend on occupation $\{\sigma\}$. As the $|\psi\rangle$'s are orthonormal, the

trace in Eq.(4.5) gives

$$\bar{Z} = \left(\frac{Nz}{2}\right)! \sum_{n_r, D(\omega)} \exp \left[N_s \left(s(n_r, D(\omega)) - \frac{n_r}{2} \ln\left(1 + \frac{1}{T}\right) - \frac{1 - n_r}{2} \int d\omega D(\omega) \ln\left(1 + \frac{1}{T} \frac{\alpha}{\omega^2 + \alpha}\right) \right) \right], \quad (4.7)$$

where $s(n_r, D(\omega)) \equiv \frac{1}{N_s} \ln \sum_{\{\sigma\}} \mathbf{1}_{R, D(\omega)}$ is configurational entropy density with given number of redundant constraints $n_r \equiv R/N_s$ and density of vibrational modes, $D(\omega)$, satisfies $(1 - n_r) \int d\omega D(\omega) \equiv \lim_{N \rightarrow \infty} \frac{1}{N_s} \sum_{\omega > 0}$.

4.4.2 No weak interactions

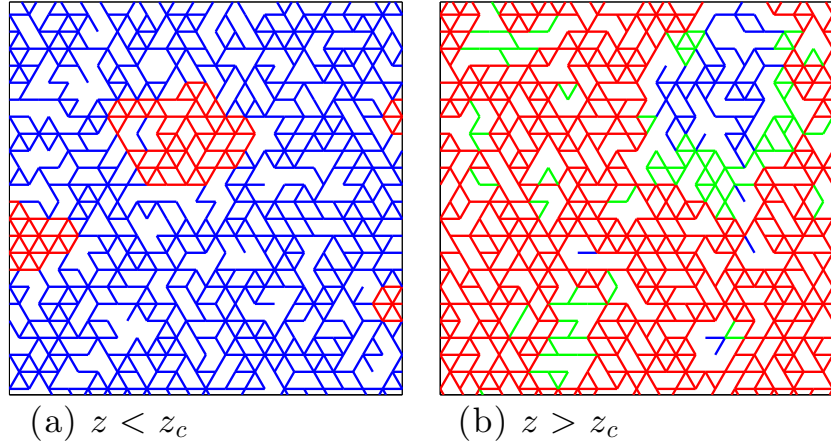


Figure 4.9: (Color online) (a) $z < z_c$, localized redundant constraints (red) in a floppy sea (blue); (b) $z > z_c$ localized floppy modes (blue) in a rigid sea (red and green).

Neglecting the weak constraints $\alpha = 0$, the last term in the exponential vanishes and the summation over states with given density of states can be absorbed into the entropy, which then depends only on the number of redundant

constraints.

$$\bar{Z} = \left(\frac{Nz}{2}\right)! \sum_{n_r} e^{N_s[s(n_r) - \frac{n_r}{2} \ln(1 + \frac{1}{T})]} \quad (4.8)$$

We propose an ideal-gas picture of “defects” to find an approximation form of the entropy $s(n_r)$. When the coordination number is very small $z < z_c$ and the network is mostly floppy, redundant constraints are defects localized in rigid islands. Similarly, when the coordination number is very large $z > z_c$ with most regions of the network rigid, there are localized floppy modes in regions where there are negative fluctuations of coordination number, which we again described as defects, see illustration in Fig. 4.9. The number of such floppy modes is equal to the number of additional over-constrained in the rigid cluster. The entropy gains from having these defects. Assuming that such defects are independent, we approximate the entropy by that of an ideal gas:

$$s(n_{\text{ex}}) \approx s(0) - n_{\text{ex}} \ln \frac{n_{\text{ex}}}{en_0(z)} \quad (4.9)$$

where n_{ex} is the excess number of redundant constraints defined in Eq.(4.3) and is thus counting the number of defects. $s(0)$ is the entropy density of the states with a minimal number of redundant constraints (i.e. they satisfy the Maxwell counting); and $n_0(z)$ is the excess number of redundant constraints at $T = \infty$. Both $s(0)$ and n_0 depend only on z and the lattice structure. This form of Eq.(4.9) fails when the assumption of independent “defects” breaks down, as must occur near the rigidity transition. However, our numerical results indicate that this approximation is very accurate, we see deviations only for $|\delta z| \lesssim 0.1$.

We numerically test the formula Eq.(4.9) for a triangular lattice. The

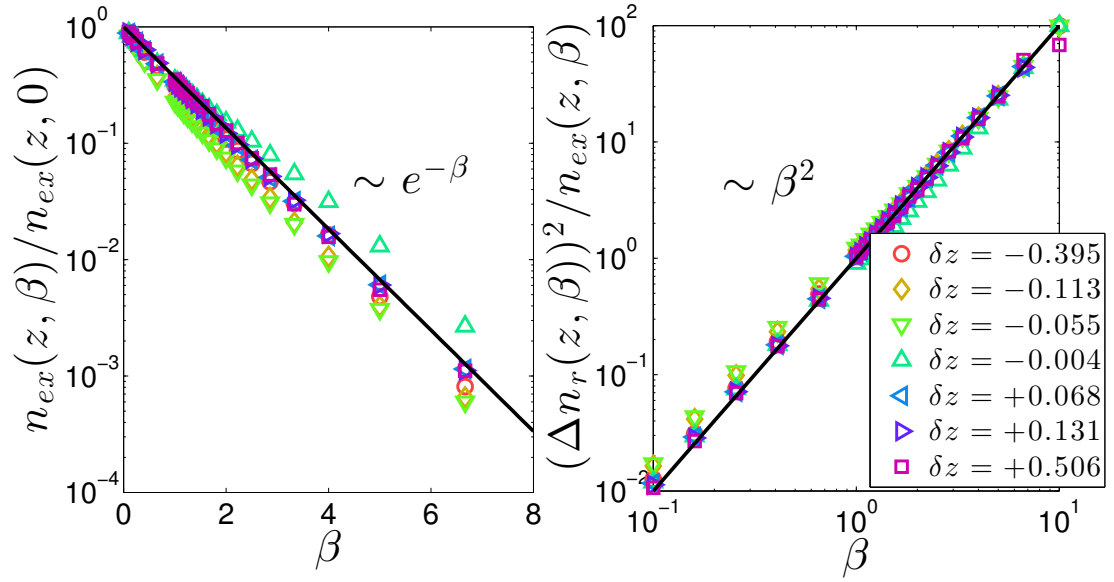


Figure 4.10: (Color online) Left: Excess number density of redundant constraints $n_{\text{ex}}(z, \beta)$. Right: Fluctuation of the number density of redundant constraints $(\Delta n_r)^2$. The solid black lines show the predictions from the approximate entropy Eq.(4.9).

configurations with R redundant constraints are weighted by $e^{-\beta R}$ for different values of the parameter β . From Eq.(4.9), the mean and variance of the excess number density of redundant constraints, n_{ex} , satisfy the following formulas:

$$\beta \equiv \frac{\partial s}{\partial n_{\text{ex}}} \Rightarrow n_{\text{ex}}(z, \beta) = n_0(z) e^{-\beta} \quad (4.10a)$$

$$\Delta n_{\text{ex}}^2(z, \beta) = -\beta^2 \frac{\partial}{\partial \beta} n_{\text{ex}}(z, \beta) = \beta^2 n_{\text{ex}}(z, \beta) \quad (4.10b)$$

Our numerical results coincide with Eqs.(4.10a) and (4.10b) remarkably well, with minor deviations for $|\delta z| \lesssim 0.1$, as shown in Fig. 4.10.

Applying Eq.(4.9), we derive the thermodynamics of our model when $\alpha =$

0. Solving the saddle point of Eq.(4.8), we obtain the average energy density:

$$\frac{1}{N_s}E(z, T) = \frac{r_0 + n_{\text{ex}}(z, T)}{2} \frac{T}{1 + T} \quad (4.11a)$$

the specific heat:

$$\frac{1}{N_s}C(z, T) = \frac{r_0 + \frac{3}{2}n_{\text{ex}}(z, T)}{2} \frac{1}{(1 + T)^2} \quad (4.11b)$$

and the excess number density of redundant constraints:

$$n_{\text{ex}}(z, T) = n_0(z) \left(1 + \frac{1}{T}\right)^{-1/2} \quad (4.11c)$$

where $r_0 \equiv \frac{\delta z}{z}\Theta(\delta z)$.

As $n_0(z)$ is expected to be an analytic function of z , Eqs.(4.11) indicate that c converges to the one found in frozen network model in the limit $T \rightarrow 0$: $c = 0$ when $\delta z < 0$ and $c = \delta z/2z$ when $\delta z > 0$ - the dashed yellow line in Fig. 4.8. This is our first central result, which shows that our previous results hold even when the network is adaptive.

Eqs.(4.11) predict the energy, specific heat, and the number density of redundant constraints at an arbitrary temperature without any fitting parameter. The solid lines, shown in Fig. 4.6(a) and (b), are predictions of Eqs.(4.11a) and (4.11b), respectively, with n_{ex} as the numerical input. They are closely consistent with the data points, which confirms the annealed free energy approximation when $\alpha = 0$. A $T^{1/2}$ power-law with numerical prefactor $n_0(z) = n_{\text{ex}}(z, \infty)$ predicted by Eq.(4.11c) coincides well with data points in Fig. 4.6(c).

Extending to finite glass transition T_g at $\alpha = 0$, we find a correction

vanishing as $\sqrt{\delta z}$ in addition to $c \approx \delta z/2z$, assuming $T_g \sim G \sim \delta z$ for $z > z_c$. But this correction is quantitatively unimportant as $n_0 \leq 0.03$ and does not change qualitatively the linear growth of the specific heat when $\delta z > 0$, as illustrated by the solid orange line in Fig. 4.8.

Our theoretic prediction that $n_{\text{ex}} \rightarrow 0$ when $T \rightarrow 0$ validates the assumptions of [73, 75, 178] that the energy of redundant bonds is proportional to their number, and that this number is R_0 at $T = 0$.

4.4.3 General case

In the thermodynamic limit, $N_s \rightarrow \infty$, we take the saddle point of Eq.(4.7),

$$\frac{2\partial s}{\partial n_r} = \ln\left(1 + \frac{1}{T}\right) - \int d\omega D(\omega) \ln\left(1 + \frac{1}{T} \frac{\alpha}{\omega^2 + \alpha}\right) \quad (4.12a)$$

and

$$\frac{2\delta s}{\delta D(\omega)} = (1 - n_r) \ln\left(1 + \frac{1}{T} \frac{\alpha}{\omega^2 + \alpha}\right) \quad (4.12b)$$

and solve for energy,

$$\begin{aligned} \frac{1}{N_s} E(z, T, \alpha) = & \frac{n_r(T)}{2} \frac{T}{1+T} \\ & + \frac{1 - n_r(T)}{2} \int d\omega D(\omega, T) \frac{\alpha T}{\alpha + (\omega^2 + \alpha)T} \end{aligned} \quad (4.13)$$

The specific heat predictions from differentiating Eq.(4.13) with numerical inputs $n_r(z, T, \alpha)$ and $D_{z,T,\alpha}(\omega)$ are plotted as solid lines in Fig. 4.7. (See Appendix Secs. C.2, C.3, and C.4 for the temperature dependence of $D(\omega)$.) Notice that replacing $n_r(T)$ by $\delta z/z$ and $D(\omega, T)$ by its low-temperature limit $D(\omega)$ studied

in [78, 116, 130], Eq.(4.13) recovers exactly the one obtained in the frozen network model, whose predictions are plotted as dashed lines in Fig. 4.7. The dashed lines converge to the solid lines despite differences at high temperatures for weakly coordinated networks.

In the limit $\alpha \rightarrow 0$ and $T \ll \alpha$, Eq.(4.13) converges to $E/N_s = T/2$, which indicates a constant specific heat $c = 0.5$ when $\delta z < 0$ independent of the models. This is shown by the solid orange line and the dashed yellow line in Fig. 4.8, and is our second key theoretical result showing the robustness of our conclusions for adaptive networks.

4.5 Conclusions

In this work, we have studied the correlation between the elasticity of inherent structures and the thermodynamics in covalent glass-forming liquids using adaptive network models. We found numerically and explained theoretically why these models have a thermodynamic behavior similar to frozen network models [116] which captures nicely experimental facts.

The main prediction conclusion of [116] is thus robust: as the coordination number approaches z_c from above, elastic frustration vanishes. This leads both to an abundance of soft elastic modes, as well as a diminution of the number of directions in phase space that cost energy, which is directly proportional to the jump of specific heat. Below the rigidity transition, the elasticity of strong force network vanishes, thus the energy landscape is governed by the weak Van der Waals interactions. At these energy scale, all directions in contact space have a cost, and

thus the specific heat increases. Thus thermodynamic properties are governed by a critical point at $\delta z = 0$, $\alpha = 0$ where the jump of specific heat is zero. This prediction focuses on the configurational part of the jump of specific heat, since we considered only the energy minima in the metastable states. In Appendix Sec. C.5, we argue that the vibrational contribution to this jump is so small in our models. Thus the main prediction of the specific heat still holds, even when including the vibrational part.

Beyond network glasses, our main result potentially explains the correlation between elasticity and the key aspects of the energy landscape in molecular glasses [4, 35, 77]. Indeed according to our work we expect glasses with a strong Boson peak to display less elastic frustration, so that they have a limited number of directions in phase space costing energy, see discussion in [116].

Chapter 5

A Model for the Erosion Onset of a Granular Bed Sheared by a Viscous Fluid

We study theoretically the erosion threshold of a granular bed forced by a viscous fluid. We first introduce a novel model of interacting particles driven on a rough substrate. It predicts a continuous transition at some threshold forcing θ_c , beyond which the particle current grows linearly $J \sim \theta - \theta_c$. The stationary state is reached after a transient time t_{conv} which diverges near the transition as $t_{\text{conv}} \sim |\theta - \theta_c|^{-z}$ with $z \approx 2.5$. Both features agree with experiments. The model also makes quantitative testable predictions for the drainage pattern: the distribution $P(\sigma)$ of local current is found to be extremely broad with $P(\sigma) \sim J/\sigma$, spatial correlations for the current are negligible in the direction transverse to forcing, but long-range parallel to it. We explain some of these features using

a scaling argument and a mean-field approximation that builds an analogy with q -models. We discuss the relationship between our erosion model and models for the plastic depinning transition of vortex lattices in dirty superconductors, where our results may also apply.

5.1 Introduction

Erosion shapes Earth’s landscape, and occurs when a fluid exerts a sufficient shear stress on a sedimented layer. It is controlled by the dimensionless Shields number $\theta \equiv \Sigma/(\rho_p - \rho)gd$, where d and ρ_p are the particle diameter and density, and ρ and Σ are the fluid density and the shear stress. Sustained sediment transport can take place above some critical value θ_c [84, 85, 87], in the vicinity of which motion is localized on a thin layer of order of the particle size, while deeper particles are static or very slowly creeping [82, 86, 88]. This situation is relevant in gravel rivers, where erosion occurs until the fluid stress approaches threshold [7]. In that case, predicting the flux J of particles as a function of θ is difficult, both for turbulent and laminar flows [6, 86, 92, 183]. We focus on the latter, where experiments show that: (i) in a stationary state, $J \propto (\theta - \theta_c)^\beta$ with $\beta \approx 1$ [81, 86, 88, 89], although other exponents are sometimes reported [87], (ii) transient effects occur on a time scale that appears to diverge as $\theta \rightarrow \theta_c$ [86, 88] and (iii) as $\theta \rightarrow \theta_c$ the density m of moving particles vanishes, but not their speed [86, 89, 90].

Two distinct views have been proposed to describe erosion near threshold. For Bagnold [6] and followers [92], hydrodynamics is key: moving particles carry a fraction of the stress proportional to their density m , such that the bed of

static particles effectively remains at the critical Shields number. This argument implies $m \sim \theta - \theta_c$, in agreement with (i,iii). However, it treats the hydrodynamic effect of a moving particle on the static bed in an average (mean-field) way, and its application when moving particles are far apart (i.e. $m \ll 1$) may thus not be warranted. By contrast, erosion/deposition models [86] emphasize the slow “armoring” or “leveling” of the particle bed. One assumes that a θ -dependent fraction of initially mobile particles evolve over a frozen static background, which contain holes. In this view, θ_c occurs when the number of holes matches the number of initially moving particles. This phenomenological model also leads to $m \sim \theta - \theta_c$ and captures (i,ii,iii) qualitatively well. However, the implicit assumption that the moving particles visit the static bed entirely (thus filling up all holes) is highly non-trivial. Indeed, due to the disorder of the static bed one expects mobile particles to follow favored paths and to eventually flow in a few channels, thus exploring a tiny region of space. Such disorder-induced coarsening dynamics occurs for example in river networks models [95], as well as plastic-depinning models of vortex lattices in dirty superconductors [97, 98] which also display a transition, but with $\beta \approx 1.5$, at odd with (i).

To decide which physical process (hydrodynamic interactions or armoring) governs the erosion threshold, new theoretical predictions must be made and put to experimental test. In this letter, we achieve the first step of this goal while resolving the apparent contradictions of deposition models. Specifically, we introduce a model of interacting particles forced along one direction on a disordered substrate. Particle interactions based on mechanical considerations are incorporated. Such model recovers (i,ii,iii) with $\beta = 1$ and an equilibration time $t_{\text{conv}} \sim |\theta - \theta_c|^{-2.5}$, which agrees quantitatively with experiments [88]. Our most striking predictions

concerns the spatial organization of the flux near threshold, which emerges from the interplay between disorder and particle interaction: (a) the distribution of local flux σ is extremely broad, and follows $P(\sigma) \sim 1/\sigma$ and (b) spatial correlations of flux are short-range and very small in the lateral direction, but are power-law in the mean flow direction. We derive $\beta = 1$ and explain why $P(\sigma)$ is broad using a mean-field description of our model, leading to an analogy with q -models [184, 185] used to study force propagation in grains.

5.2 Erosion Model

We consider a density n of particles on a frozen background. n should be chosen to be of order one, but its exact value does not affect our conclusions. The background is modeled via a square lattice, whose diagonal indicates the direction of forcing, referred to as “downhill”. The lattice is bi-periodic, of dimension $L \times W$, where L is the length in downhill direction and W the transverse width. Each node i of the lattice is ascribed a height $h_i \in [0, 1]$, chosen randomly with a uniform distribution. Lattice bonds $i \rightarrow j$ are directed in the downhill direction, and characterized by an inclination $\theta_{i \rightarrow j} = h_i - h_j$. We denote by θ the amplitude of the forcing. For an isolated particle on site i , motion will occur along the steepest of the two outlets (downhill bonds) [96], if it satisfies $\theta + \theta_{i \rightarrow j} > 0$. Otherwise, the particle is trapped.

However, if particles are adjacent, interaction takes place. First, particles cannot overlap, so they will only move toward unoccupied sites. Moreover, particles can push particles below them, potentially un-trapping these or affecting their

direction of motion. To model these effects, we introduce scalar forces $f_{i \rightarrow j}$ on each outlet of occupied sites, which satisfy:

$$f_{i \rightarrow j} = \max(f_{j' \rightarrow i} + \theta_{i \rightarrow j} + \theta, 0) \quad (5.1)$$

where $f_{j' \rightarrow i}$ is the force on the input bond $j' \rightarrow i$ along the same direction as $i \rightarrow j$, as depicted in Fig. 5.1. Eq.(5.1) captures that forces are positive for repulsive particles, and that particle i exerts a larger force on toward site j if the bond inclination $\theta_{i \rightarrow j}$ is large, or if other particles above i are pushing it in that direction. From our analysis below, we expect that the details of the interactions (contacts, lubrication forces, etc...) are not relevant, as long as the direction of motion of one particle can depend on the presence of particles above it- an ingredient not present in [97, 98].

We update the position of the particles as follows, see Fig. 5.1 for illustration. We first compute all the forces in the system. Next we consider one row of W sites, and consider the motion of its particles. Priority is set by considering first outlets with the largest $f_{i \rightarrow j}$ and unoccupied downhill site j . Once all possible moves ($f_{i \rightarrow j} > 0$, j empty) have been made, forces are computed again in the system, and the next uphill row of particles is updated. When the L rows forming the periodic system have all been updated, time increases by one.

For given parameters θ, n we prepare the system via two protocols. In the “quenched” protocol, one considers a given frozen background, and launch the numerics with a large θ and randomly placed particles - parameters are such that the system is well within the flowing phase. Next, θ is lowered slowly so that stationarity is always achieved. We also consider the “Equilibrated” proto-

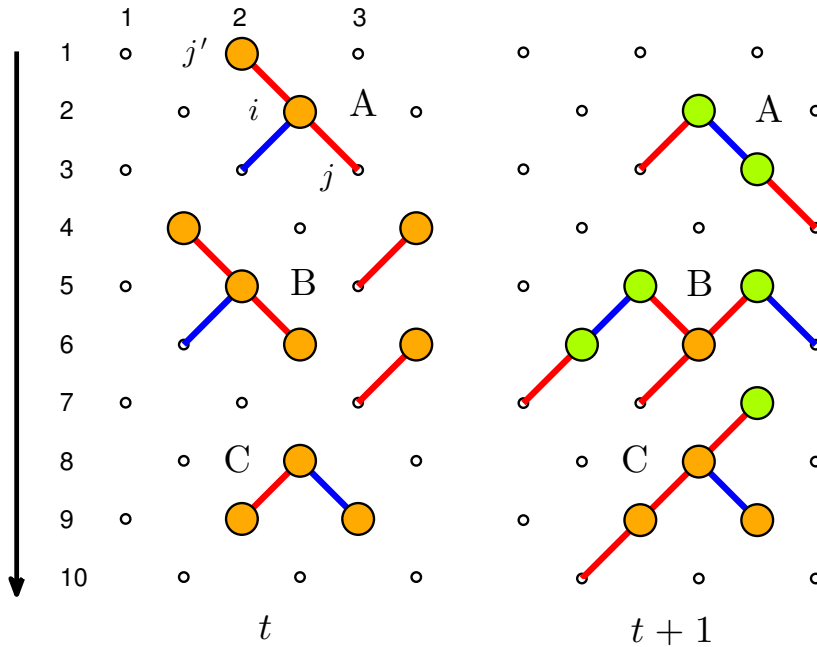


Figure 5.1: Illustration of the model. Small circles indicate lattice sites, particles are represented by discs in yellow, or green if motion occurred between t (left) and $t + 1$ (right). The black arrow is in the downhill direction. Solid lines indicate outlet with positive forces. If a particle has two outlets with positive forces, the larger (smaller) one is colored in red (blue).

col: for *any* θ , particles initial positions are random. Dynamical properties are measured after the memory of the random initial condition is lost. We find that using different protocols does not change critical exponents, but that the quenched protocol appears to converge more slowly with system size. Below we present most of our results obtained from the “equilibrated” protocol with $W = 4\sqrt{L}$ [98], and $n = 0.25$ unless specified.

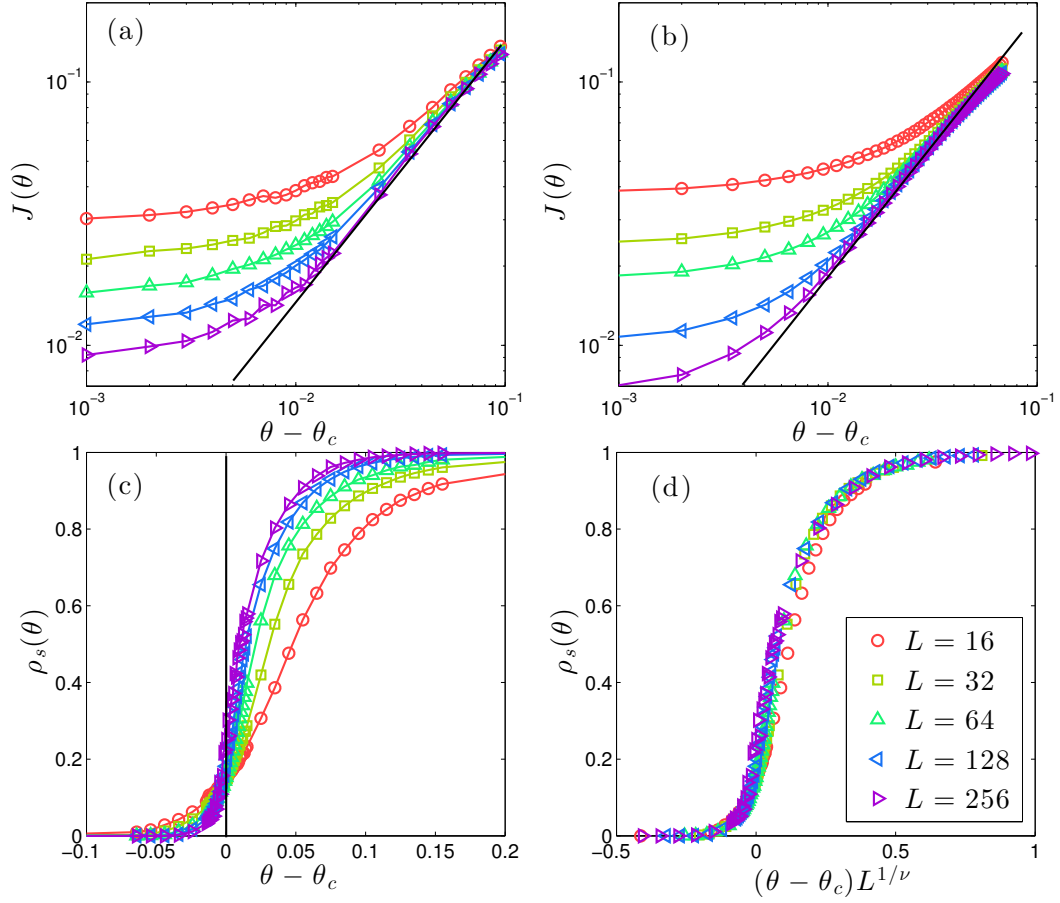


Figure 5.2: Average current J versus $\theta - \theta_c$ in log-log scale for the (a) “equilibrated” and (b) “quenched” protocols, for which $\theta_c = 0.164 \pm 0.002$ and $\theta_c = 0.172 \pm 0.002$ respectively- a difference plausibly due to finite size effects. The black solid lines with slope one indicate the linear relation $J \propto \theta - \theta_c$. (c) Density of conducting sites ρ_s versus $\theta - \theta_c$ for the “equilibrated” protocol. (d) ρ_s curves collapsed by rescaling $\theta - \theta_c$ with $L^{1/\nu}$, where $\nu = 3.0 \pm 0.2$.

5.3 Numerical Results on Dynamics of the Model

Once the steady state is reached, we measure the average current of particles J and the number density of sites carrying a finite current ρ_s . Measurements of

both quantities indicate a sharp dynamical transition at some θ_c below which $J = 0$ and $\rho_s = 0$ as $L \rightarrow \infty$, see Fig. 5.1. θ_c can be accurately extracted by considering the crossing point of the curves $\rho_s(\theta)$ as L is varied, yielding $\theta_c = 0.164 \pm 0.002$ for the equilibrated protocol. In the limit $L \rightarrow \infty$ our data extrapolates to:

$$J(\theta) \sim \theta - \theta_c \quad \text{for } \theta > \theta_c \quad (5.2)$$

$$\rho_s(\theta) = \Theta(\theta - \theta_c), \quad (5.3)$$

where Θ is the Heaviside function. Eq.(5.2) corresponds to $\beta = 1$, whereas Eq.(5.3) indicates that all sites are visited by particles in the flowing phase. Introducing the exponent $\rho_s(\theta) \sim (\theta - \theta_c)^\gamma$, this corresponds to $\gamma = 0$. The collapse of Fig. 5.2(d) shows how convergence to Eq.(5.3) takes place as $L \rightarrow \infty$, from which a finite size scaling length $\xi \sim (\theta - \theta_c)^{-\nu}$ with $\nu \approx 3$ can be extracted.

Criticality is also observed in the transient time t_{conv} needed for the current to reach its stationary value. Fig. 5.3 reports that $t_{\text{conv}} \sim |\theta - \theta_c|^{-z}$ with $z \approx 2.5$ on both sides of the transition, which captures accurately the experiments of [88] and the numerics of [91].

The spatial organization of the current in steady state can be studied by considering the time-averaged local current σ_i on site i , or the time-averaged outlet current $\sigma_{i \rightarrow j}$. The spatial average of each quantity is J . Fig. 5.4 shows an example of drainage pattern, i.e. one realization of the map of the $\sigma_{i \rightarrow j}$.

To quantify such patterns, we compute in Fig. 5.5(a) the distribution $P(\sigma)$

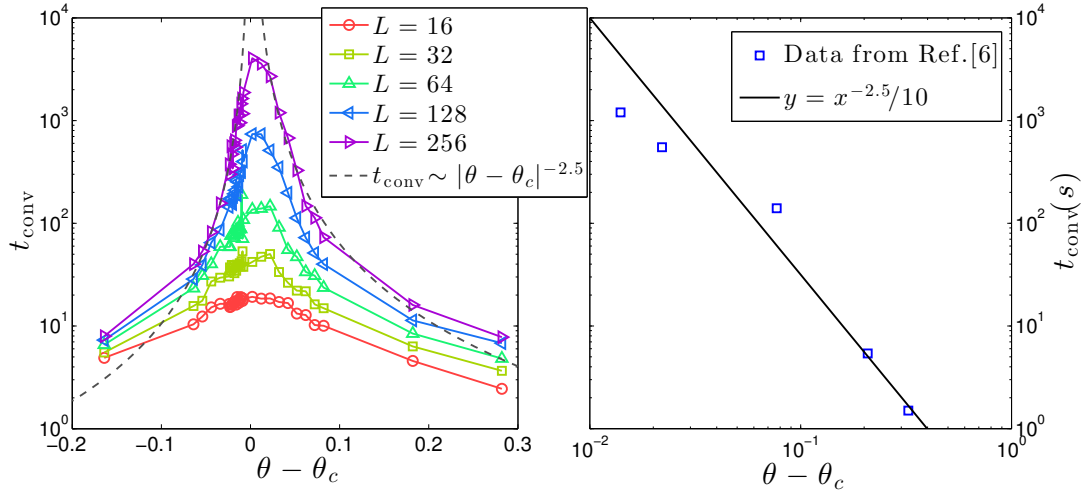


Figure 5.3: Left: Transient time t_{conv} *v.s.* θ . For a given realization, t_{conv} is defined as the smallest time for which $J(t) - J \leq \sqrt{\text{Var}(J)}$ where $\text{Var}(J) = \lim_{T \rightarrow \infty} \frac{1}{T} \sum_{t=1}^T (J(t) - J)^2$. The gray dashed lines correspond to $t_{\text{conv}} \sim |\theta - \theta_c|^{-2.5}$. Right: The obtained exponent fits well the observations of [88].

of the local current σ_i for various mean current J . We observed that:

$$P(\sigma) = J\sigma^{-\tau} f(\sigma) \quad (5.4)$$

where $\tau \approx 1$ and f is a cut-off function, expected since in our model $\sigma_i < 1$. Eq.(5.4) indicates that $P(\sigma)$ is remarkably broad. In fact, the divergence at small σ is so pronounced that a cut-off σ_{min} must be present in Eq.(5.4) to guarantee a proper normalization of the distribution $P(\sigma)$, although we cannot detect it numerically.

Next, we compute the spatial correlation of the local current in the trans-

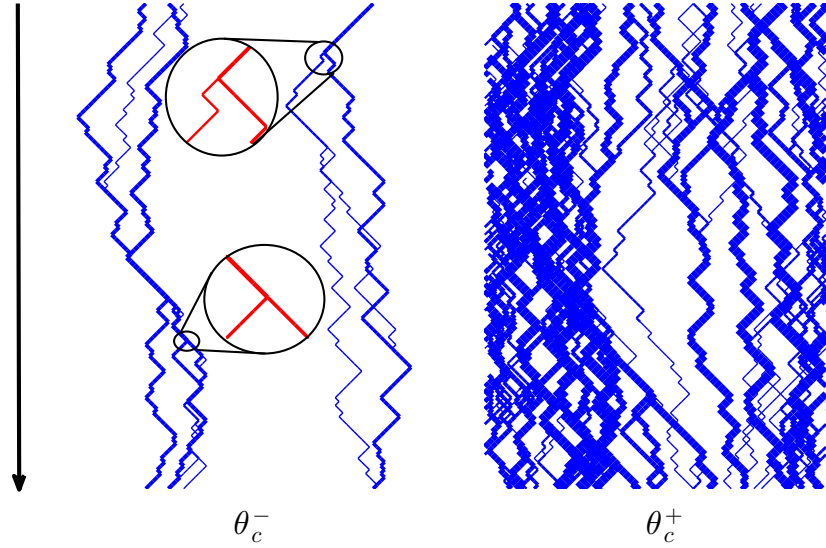


Figure 5.4: Examples of drainage pattern just below θ_c (Left) and above (Right). The black arrow shows the downhill direction. The thickness of the lines represents $\sigma_{i \rightarrow j}$ in logarithmic scale. A few examples showing splitting events are magnified on the left. Here $W = 45$ and $L = 128$, and $J > 0$ even below θ_c due to finite size effects.

verse direction $C_T(x)$, defined as:

$$C_T(x) = \overline{(\langle \sigma_i \sigma_{i+x} \rangle - J^2) / (\langle \sigma_i^2 \rangle - J^2)} \quad (5.5)$$

where the site i and $i + x$ are on the same row, but at a distance x of each other. Here the brackets denote the spatial average, whereas the overline indicates averaging over the quenched randomness (the h_i 's). Fig. 5.6(a) shows that no transverse correlations exist for distances larger than one site. However, long-range, power-law correlations are observed in the longitudinal direction, as can be seen by defining a longitudinal correlation function $C_L(y)$, where y is the vertical distance between two sites belonging to the same column. We find that $C_L(y) \sim 1/\sqrt{y}$ at

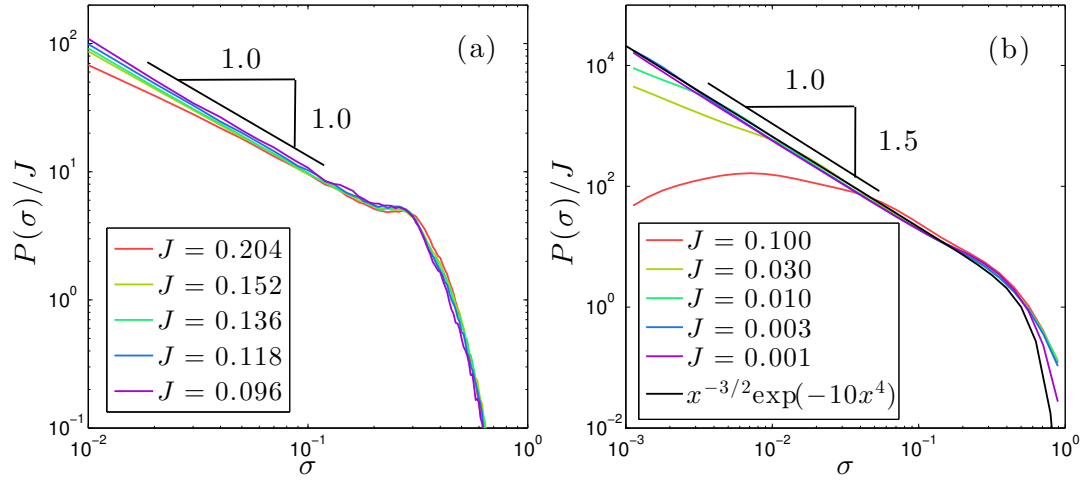


Figure 5.5: Distribution of the site current $P(\sigma)$ in steady state for given average currents J of (a) the erosion model ($L = 256$, $W = 64$) and (b) our mean-field model ($W = 1600$).

θ_c , but that $C_L(y)$ decays somewhat faster deeper in the flowing phase, as shown in Fig. 5.6(b).

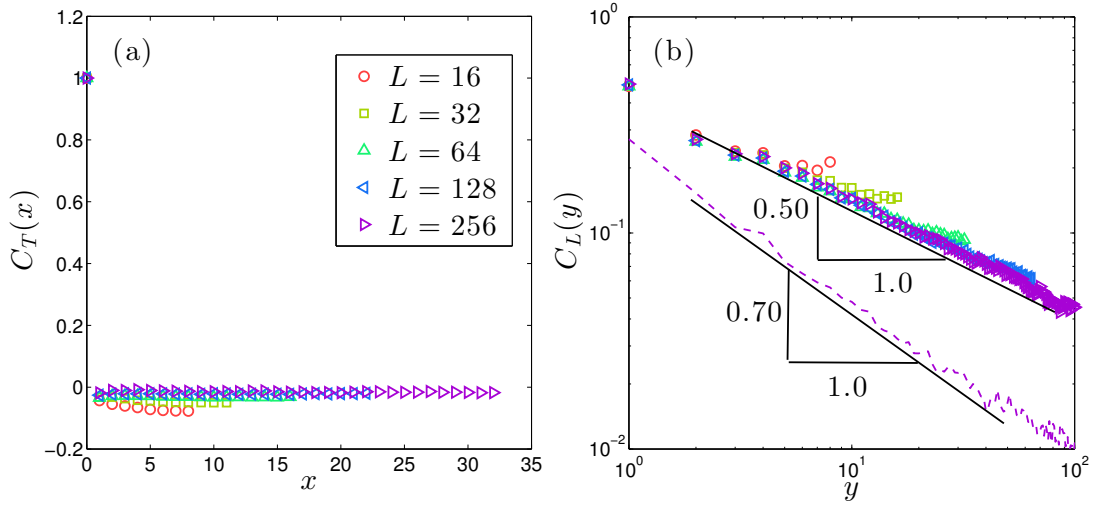


Figure 5.6: (a) Transverse current correlations C_T at θ_c and (b) longitudinal current correlation C_L at θ_c and at $\theta - \theta_c = 0.25$ for $L = 256$ (dashed line).

5.4 An Argument on the Scaling Relation

We now derive a relationship between the exponents β characterizing J and γ characterizing ρ_s . It holds true for both protocols, but is presented here in the “quenched” case. Near threshold, at any instant of time the density of moving particles is $J \ll n < 1$, thus most of the particles are trapped and will move only when a mobile particle passes by. As θ is decreased by some $\delta\theta$, a finite density of new traps $\delta m \sim \delta\theta$ is created. If these traps appear on the region of size ρ_s where mobile particles flow, they will reduce the fraction of mobile particle by $\delta J = \rho_s \delta m \sim \rho_s \delta\theta$, which implies:

$$\beta = \gamma + 1 \tag{5.6}$$

Eq.(5.6) shows that the result $\beta = 1$ is a direct consequence of the fact that in our model, all sites are explored by mobile particles for $\theta > \theta_c$, a result which is not obvious. In the dirty superconductor models of [98, 186], this is not the case and for the “equilibrated” protocol $\beta > 1$ was found. We argue that this difference comes from the dynamical rules chosen in [98, 186], according to which “rivers” forming the drainage pattern never split: their current grows in amplitude in the downhill direction, until it reaches unity. In these models the drainage pattern thus consists of rivers of unit current, avoiding each other, and separated by a typical distance of order $1/J$. Our model behaves completely differently because rivers can split, as emphasized in Fig. 5.4. This comes about because the direction taken by a particle can depend on the presence of a particle right above it, as illustrated in case A of Fig. 5.1. This effect is expected to occur in the erosion problem due to hydrodynamic interactions or direct contact between particles, and may also be

relevant for superconductors.

5.5 Mean-field Model on the Distribution of Local Currents

We now seek to quantify the effect of splitting. Its relevance is not obvious a priori, as splitting stems from particle interactions, and may thus become less important as the fraction of moving particles vanishes as $J \rightarrow 0$. To model this effect we consider that the current σ_i on a site i is decomposed in its two outlets as $\sigma_i = q\sigma_i + (1 - q)\sigma_i$, where q is a random variable of distribution $\eta(q)$. If there were no splitting then $\eta(q) = \frac{1}{2}\delta(q) + \frac{1}{2}\delta(1 - q)$. Here instead, we assume that $\eta(q) = \frac{1}{2}\delta(q - J) + \frac{1}{2}\delta(1 - J - q)$. This choice captures that the probability of splitting is increased if more moving particles are present, and can occur for example if two particles flow behind each other, as exemplified in case A of Fig. 5.1. Next, we make the mean field assumption that two adjacent sites i and j on the same row are uncorrelated, $P(\sigma_i, \sigma_j) = P(\sigma_i)P(\sigma_j)$. We then obtain the self-consistent equation that $P(\sigma)$ must be equal to:

$$\int dq_1 dq_2 d\sigma_1 d\sigma_2 \eta(q_1) \eta(q_2) P(\sigma_1) P(\sigma_2) \delta(q_1 \sigma_1 + q_2 \sigma_2 - \sigma) \quad (5.7)$$

This mean-field model belongs to the class of q -models introduced to study force propagation [184, 185]. It is easy to simulate, and some aspects of the solution can be computed. Numerical results are shown in Fig. 5.5(b). The result obtained for $P(\sigma)$ is very similar to Eq.(5.4) that describes our erosion model: $P(\sigma)$ is found

to be power-law distributed (although $\tau = 3/2$ instead of $\tau = 1$) where with an upper cutoff at $\sigma_{\max} \sim 1$, and $P(\sigma) \propto J$.

These results are of interest, as they explain why $P(\sigma)$ is very broad, and is not dominated by sites displaying no current at all (which would correspond to a delta function at zero) even as $J \rightarrow 0$, thus confirming that $\gamma = 0$. They can be explained by taking the Laplace transform \tilde{P} of Eq.(5.7). One then obtains a non-linear differential equation for \tilde{P} , from which it can be argued generically that $\tau = 3/2$ [185]. We have performed a Taylor expansion of \tilde{P} around zero, which leads to relationship between the different moments of the distribution $P(\sigma)$. From it, we can show that $P(\sigma) \propto J$ and $\sigma_{\max} \sim 1$. We also find that the cut-off of the divergence of $P(\sigma)$ at small argument follows $\sigma_{\min} \sim J^{1/(\tau-1)}$.

5.6 Potential Experimental Tests

We have introduced a novel model for over-damped interacting particles driven on a disordered substrate. It predicts a dynamical phase transition at some threshold forcing θ_c , and makes quantitative predictions for various quantities including the particle current and the drainage pattern, testable by tracking particles on the surface [86]. Our model includes the possibility that channels carrying most of the flow split, which may also be well-suited to describe plastic depinning phenomena including the pinning of vortices in dirty superconductors [97, 187] or driven colloidal systems [188, 189], which have never been received a proper analytical treatment ².

² In plastic depinning an exponent $\beta \geq 1.5$ is often reported, larger than our predicted $\beta = 1$. However we observe that large systems are required to measure β accurately, and that in smaller

Note that our model assumes that particles are over-damped, and that their inertia is negligible. We expect inertia to lead to hysteresis and make the transition first order, as observed on inertial granular flows down an inclined plane [190], although this effect may be small in practice [191]. We did not consider non-laminar flows, nor temperature (that can be relevant for colloids). Both effects should smooth the transition, and lead to creep even below θ_c .

systems β can appear significantly larger.

Chapter 6

Dynamics and Correlations among Soft Excitations in Marginally Stable Glasses

Marginal stability is the notion that stability is achieved, but only barely so. This property constrains the ensemble of configurations explored at low temperature in a variety of systems, including spin, electron and structural glasses. A key feature of marginal states is a (saturated) pseudo-gap in the distribution of soft excitations. We examine how such pseudo-gaps appear dynamically by studying the Sherrington-Kirkpatrick (SK) spin glass. After revisiting and correcting the multi-spin-flip criterion for local stability, we show that stationarity along the hysteresis loop requires soft spins to be frustrated among each other, with a correlation diverging as $C(\lambda) \sim 1/\lambda$, where λ is the stability of the more stable spin. We explain how this arises spontaneously in a marginal system and develop

an analogy between the spin dynamics in the SK model and random walks in two dimensions. We discuss analogous frustrations among soft excitations in short range glasses and how to detect them experimentally. We also show how these findings apply to hard sphere packings.

6.1 Introduction

In glassy materials with sufficiently long-range interactions, stability at low temperature imposes an upper bound on the density of soft excitations [101]. In electron glasses [102, 103, 192–195] stability towards hops of individual localized electrons requires that the density of states vanishes at the Fermi level, exhibiting a so-called Coulomb gap. Likewise, in mean-field spin glasses [11, 104–107, 196–198] stability towards flipping several “soft” spins implies that the distribution of local fields vanishes at least linearly. In hard sphere packings the distribution of forces between particles in contact must vanish analogously, preventing that collective motions of particles lead to denser packings [56, 108, 109]. Often, these stability bounds appear to be saturated [104, 109–111, 194, 198]. Such *marginal stability* can be proven for dynamical, out-of-equilibrium situations under slow driving at zero temperature [101] if the effective interactions do not decay with distance. This situation occurs in the Sherrington-Kirkpatrick (SK) model (see Eq. (6.1) below), but also in finite-dimensional hard sphere glasses, where elasticity induces non-decaying interactions [128]. Marginality is also found for the ground state or for slow thermal quenches by replica calculations for spin glass [105, 199] and hard sphere systems [115, 200], assuming infinite dimension.

The presence of pseudo-gaps strongly affects the physical properties of these glasses. The Coulomb gap alters transport properties in disordered insulators [102, 103], while its cousin in spin glasses suppresses the specific heat and susceptibility. It was recently proposed that the singular rheological properties of dense granular and suspension flows near jamming are controlled by the pseudo-gap exponents in these systems [201]. More generally, an argument of Ref. [101] shows that a pseudo-gap implies avalanche-type response to a slow external driving force, so-called crackling [202], for a range of applied forcing. Such behavior is indeed observed in these systems [104, 194, 203] and in the plasticity of crystals [204], and contrasts with depinning or random field Ising models where crackling occurs only at one specific value of forcing [9, 205, 206]. Despite the central role of pseudo-gaps, it has not been understood how they emerge dynamically, even though some important elements of the athermal dynamics of the SK spin glass have been pointed out in earlier works [106, 197].

In this Letter we identify a crucial ingredient that was neglected in previous dynamical approaches, and also in considerations of multi-spin stability: Soft spins are strongly frustrated among each other, a correlation that becomes nearly maximal for spins in the weakest fields. We expect analogous correlations in short range spin glasses, which can be probed experimentally. These correlations require revisiting earlier multi-spin stability arguments that assumed opposite correlations. We then argue, assuming stationarity along the hysteresis loop, that the correlation $C(\lambda)$ between the softest spins and spins in local fields of magnitude λ must follow $C(\lambda) \sim 1/\lambda^\gamma$, with $\gamma = 1$. Using this in a Fokker-Planck description of the dynamics we predict the statistics of the number of times a given spin flips in an avalanche.

6.2 Dynamics of Sherrington-Kirkpatrick Model

We consider the SK model with N Ising spins ($s_i = \pm 1$) in an external field h :

$$\mathcal{H} = -\frac{1}{2} \sum_{i \neq j} J_{ij} s_i s_j - h \sum_{i=1}^N s_i. \quad (6.1)$$

All spins are coupled to each other by a symmetric matrix J_{ij} , whose elements are *i.i.d.* Gaussian random variables with zero mean and variance $1/N$. The total magnetization is $M \equiv \sum_i s_i$. We define the local field h_i and the local stability λ_i of spin i by

$$h_i \equiv -\frac{\partial \mathcal{H}}{\partial s_i} = \sum_{j \neq i} J_{ij} s_j + h, \quad \lambda_i = h_i s_i. \quad (6.2)$$

The spin s_i is called stable when it aligns with the local field, i.e. if $\lambda_i > 0$, and unstable otherwise. The energy to flip the spin $s_i \rightarrow -s_i$ (and hence $\lambda_i \rightarrow -\lambda_i$) is:

$$\Delta \mathcal{H}_1(i) \equiv \mathcal{H}(-s_i) - \mathcal{H} = 2s_i \left(\sum_{j \neq i} J_{ij} s_j + h \right) = 2\lambda_i. \quad (6.3)$$

As in Ref. [104], we consider the hysteresis loop at zero temperature obtained by quasi-statically increasing the field, as shown in Fig. 6.1(a). When a spin turns unstable, we apply a greedy Glauber dynamics that relaxes the system in an avalanche-like process towards a new one-spin-flip stable state by sequentially flipping the most unstable spin. Such hysteretic field ramping has also been used to find approximate ground states [207, 208]. Those states empirically exhibit a pseudo-gap in the distribution of the λ_i [104, 197, 198],

$$\rho(\lambda) = A\lambda^\theta + O(N^{-\theta/(1+\theta)}), \quad (6.4)$$

with $\theta = 1$ for $\lambda \ll 1$, as shown in Fig. 6.1(b), but with a slope A significantly larger than in equilibrium [105, 106, 209]. The avalanche size is power-law distributed [104]:

$$D(n) = n^{-\tau} d(n/N^\sigma) / \Xi(N), \quad (6.5)$$

where n is the number of flips in an avalanche. The scaling function $d(x)$ vanishes for $x \gg 1$. N^σ is the finite size cutoff, and $\Xi(N)$ is a size dependent normalization if $\tau \leq 1$. Numerical studies of the dynamics of the SK model indicate that $\tau = \sigma = 1$ and $\Xi = \ln N$ [104, 198], as shown by the finite size collapse in Fig. 6.1(c). While one can argue that $\theta = 1$ along the hysteresis curve [101], the exponents τ and σ have not been derived theoretically for the dynamics (unlike for “equilibrium avalanches”, for which $\tau = 1$ has been obtained analytically [11, 107]).

Below we present a theoretical analysis of the dynamics. We assume that the average number of times a spin flips along the hysteresis loop diverges with N for any finite interval of applied field $[h, h + \Delta h]$ if $h = O(1)$. This assures that a stationary regime is reached rapidly. (For $\tau = 1$ this condition simply reads $\sigma + 1/(1 + \theta) > 1$)¹. We further rely on $\theta < \infty$. This implies a diverging number of avalanches in the hysteresis loop, each contributing a subextensive amount of dissipation¹. The latter rules out avalanches running into strongly unstable configurations, with an extensive number of spins with negative stability $|\lambda| = O(1)$. Thus, the lowest local stability encountered in an avalanche, λ_0 , must satisfy $\lambda_0 \rightarrow 0$ as $N \rightarrow \infty$, as we confirm numerically in Fig. 6.2(a).

¹The typical external field increment triggering an avalanche is $h_{\min} \sim \lambda_{\min} \sim N^{-1/(1+\theta)}$, so there are $N_{\text{av}} \sim 1/h_{\min} \sim N^{1/(1+\theta)}$ avalanches in a finite range of external field dh [101]. Each avalanche contains on average $N_{\text{flip}} \sim \int n D(n) dn \sim N^{(2-\tau)\sigma}$ flip events. The total number of flip events along the hysteresis curve is $N_{\text{av}} N_{\text{flip}} \sim N^{(2-\tau)\sigma + 1/(1+\theta)}$, which we assume to be $\gg N$.

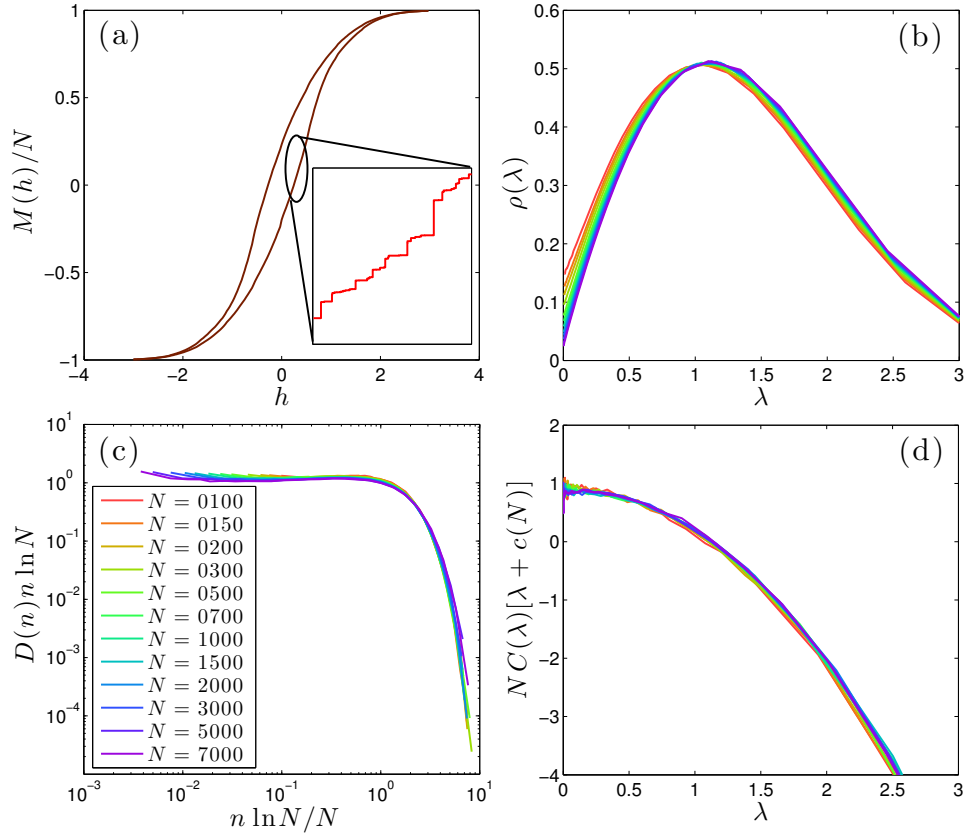


Figure 6.1: (a) Hysteresis loop: Magnetization M under a periodic quasi-static driving of the external field h . Inset: magnified segment of the hysteresis loop of a finite size system. (b) Distribution of local stabilities, $\rho(\lambda)$, in locally stable states along the hysteresis loops for different system sizes N . (c) Finite size scaling of the avalanche size distribution $D(n)$ confirms $\tau = \sigma = 1$ up to logarithmic corrections. (d) Correlation $C(\lambda)$ between the least stable spin and spins of stability λ in locally stable states along the hysteresis loop. The data for different system sizes collapses, implying $C(\lambda \ll 1) \sim 1/\lambda$ in the thermodynamic limit.

6.3 Multi-spin Stability Criterion

A static bound for the pseudogap exponent θ is obtained by considering two of the softest spins i, j (with stabilities $\lambda_{\min} \sim 1/N^{1/(1+\theta)}$) [101, 113, 114].

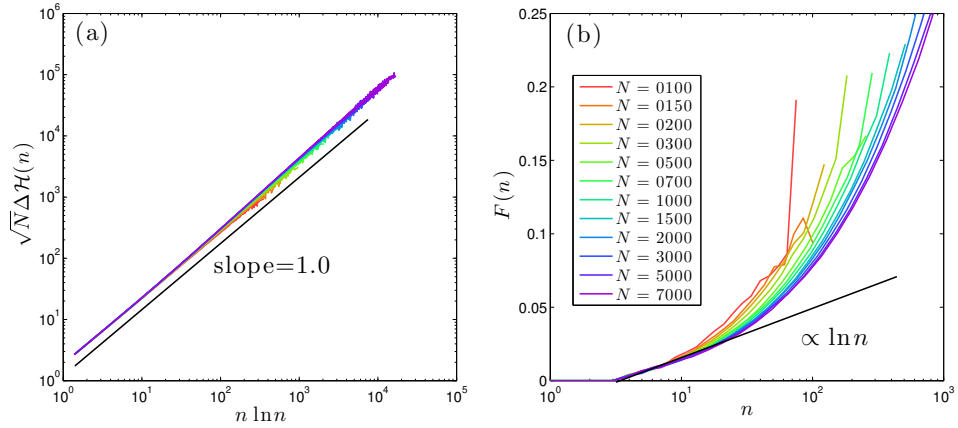


Figure 6.2: (a) The average dissipated energy $\Delta\mathcal{H}$ in avalanches of size n scales as $\Delta\mathcal{H} \sim n \ln n / \sqrt{N}$. $-\Delta\mathcal{H}/n$ is a measure of the typical value of the stability of most unstable spins, $\lambda_0(n)$. Thus, in the thermodynamic limit, $\lambda_0 \sim \ln n / \sqrt{N} \ll 1$ even for very large avalanches. (b) The average number of times, $F(n)$, spins active in avalanches of size n re-flip later on in the avalanche.

Their simultaneous flip costs an energy $2(\lambda_i + \lambda_j - 2s_i s_j J_{ij})$. The last term scales as $1/\sqrt{N}$ and is negative if the two spins are *unfrustrated*. If this occurs with finite probability, a strong enough pseudogap, $\theta \geq 1$, is necessary to prevent the last term from overwhelming the stabilizing terms. The extension of this argument to multi-spin stability reveals its subtle nature. Flipping a set \mathcal{F} of m spins in a one-spin flip stable state costs

$$\Delta\mathcal{H}(\mathcal{F}) = 2 \sum_{i \in \mathcal{F}} \lambda_i - 2 \sum_{i, j \in \mathcal{F}} J_{ij} s_i s_j. \quad (6.6)$$

The initial state is unstable to multi-flip excitations if $\Delta\mathcal{H} < 0$ for some \mathcal{F} . Refs. [113, 114] considered just the set of the m softest spins. Extremal statistics and the assumption of Eq. (6.4) implies the scaling of the maximal stabilities $\lambda(m) \sim (m/N)^{1/(1+\theta)}$, and thus $\sum_{i \leq m} \lambda_i \sim m\lambda(m)$. The term $\sum_{i \leq m} J_{ij} s_i s_j \sim$

$m(m/N)^{1/2}$ was erroneously argued to be positive *on average*, which yielded the bound $\theta \geq 1$ to guarantee $\Delta\mathcal{H}_m > 0$. However, numerically we find that on average $\sum_{i \leq m} J_{ij} s_i s_j$ is negative for soft spins. More precisely, the correlation $C(\lambda) = -2\langle J_{ss} \rangle$ between a spin of stability λ and the softest spin in the system is positive for small λ , as shown in Fig. 6.1(d). Postulating that:

$$C(\lambda) \sim \lambda^{-\gamma} N^{-\delta}, \quad (6.7)$$

it leads to $\langle -\sum_{i \leq m} J_{ij} s_i s_j \rangle \sim m^2 C(\lambda(m)) \sim m^{2-\gamma/(1+\theta)} N^{\gamma/(1+\theta)-\delta}$. A more complete characterization of correlations is given in the Appendix Secs. D.1, D.2.

It follows that the average r.h.s. of Eq. (6.6) is always positive. We argue that the stability condition nevertheless leads to a non-trivial constraint, because the last term of Eq. (6.6) can have large fluctuations. Indeed, consider all sets \mathcal{F} of m spins belonging to the $m' > m$ softest spins, and for definiteness we choose $m' = 2m$ here. To determine the probability that the optimal set leads to a negative $\Delta\mathcal{H}$ in Eq. (6.6), we use an approximate estimate akin to the random energy model [136]. The variance of the fluctuation $X \equiv \sum_{i,j \in \mathcal{F}} J_{ij} s_i s_j - \langle \sum_{i,j \in \mathcal{F}} J_{ij} s_i s_j \rangle$ is of order m/\sqrt{N} . Since there are 2^{2m} sets \mathcal{F} , the number density having fluctuation X follows $\mathcal{N}(X) \sim \exp[2m \ln(2) - X^2 N/m^2]$. The most negative fluctuation X_{\min} is determined by $\mathcal{N}(X_{\min}) \sim 1$, leading to $X_{\min} \sim -m^{3/2}/\sqrt{N}$. Correlations neglected by this argument should not affect the scaling. The associated energy change is thus, according to Eq. (6.6) and the subsequent estimates of each term:

$$\Delta\mathcal{H}(\mathcal{F}_{\min}) = m^{(2+\theta)/(1+\theta)} / N^{1/(1+\theta)} + m^{2-\gamma/(1+\theta)} N^{\gamma/(1+\theta)-\delta} - m^{3/2}/\sqrt{N}. \quad (6.8)$$

Multi-spin stability requires that for large N and fixed m this expression be positive. This yields the conditions:

$$\theta \geq 1, \quad \text{or} \quad \gamma/(1 + \theta) - \delta \geq -1/2. \quad (6.9)$$

However, the correlation in Eq. (6.7) cannot exceed the typical coupling among spins, $C \lesssim 1/\sqrt{N}$, which requires $\gamma/(1 + \theta) - \delta \leq -1/2$. Thus, if $\theta < 1$, stability imposes the equality $\gamma/(1 + \theta) - \delta = -1/2$, while the scaling with $m \gg 1$ additionally requires $2 - \gamma/(1 + \theta) \geq 3/2$; or in other words, $\gamma \leq (1 + \theta)/2 \leq 1$ and $\delta \leq 1$. In the relevant states, all three exponents θ , γ , and δ turn out to equal 1 and thus satisfy these constraints as exact equalities. We will now show how to understand this emergent marginal stability from a dynamical viewpoint.

6.4 Fokker-Planck Description of the Dynamics

Consider an elementary spin flip event in the greedy relaxation dynamics, cf. Fig. 6.3. The stability of the flipping spin 0 (red) changes from λ_0 to $-\lambda_0$ as the spin flips from s_0 to $-s_0$. Due to the coupling J_{0j} , the stability of all other spins j (green or blue) receives a kick, $\lambda_j \rightarrow \lambda'_j = \lambda_j - 2J_{0j}s_0s_j$. Using an expansion in $1/N$, we can describe the dynamics of the distribution of local stabilities $\rho(\lambda, t)$ by a Fokker-Planck equation, similarly as in Refs. [106, 197]:

$$\partial_t \rho(\lambda, t) = -\partial_\lambda [v(\lambda, t) - \partial_\lambda D(\lambda, t)] \rho(\lambda, t) - \delta(\lambda - \lambda_0(t)) + \delta(\lambda + \lambda_0(t)), \quad (6.10)$$

where t counts the number of *flips per spin*. The drift $v(\lambda, t) \equiv -2N\langle J_{0i}s_0s_i \rangle_{\lambda_i=\lambda} \equiv NC(\lambda, t)$ is the average positive kick received by a spin of stability λ . The diffusion constant $D(\lambda, t) \equiv 2N\langle J_{0i}^2 \rangle_{\lambda_i=\lambda} = 2$ is the mean square of those kicks, where we have assumed that the random parts of successive kicks are uncorrelated, as our numerics support. For the dynamics to have a non-trivial thermodynamic limit the scaling $\langle J_{0i}s_0s_i \rangle \sim 1/N$ must hold, i.e., $\delta = 1$ in Eq. (6.7). We further recall that $\lambda_0(t) \rightarrow 0$ as $N \rightarrow \infty$. We may thus replace the δ -functions in Eq. (6.10) by a reflecting boundary condition at $\lambda = 0$,

$$[v(\lambda, t) - \partial_\lambda D(\lambda, t)]\rho(\lambda, t)|_{\lambda=0} = 0. \quad (6.11)$$

Since we assume that spins flip many times along the hysteresis loop, finite intervals on the loop correspond to diverging times $\Delta t \rightarrow \infty$. At those large times a dynamical steady state (ss) must be reached. In such a state the flux of spins must vanish everywhere:

$$v_{\text{ss}}(\lambda) = D\partial_\lambda \rho_{\text{ss}}(\lambda)/\rho_{\text{ss}}(\lambda) \rightarrow 2\theta/\lambda, \quad (6.12)$$

where we assumed that ρ_{ss} follows Eq. (6.4). This result is tested in Fig. 1(d). A similar result was obtained in Ref. [106] following a quench.

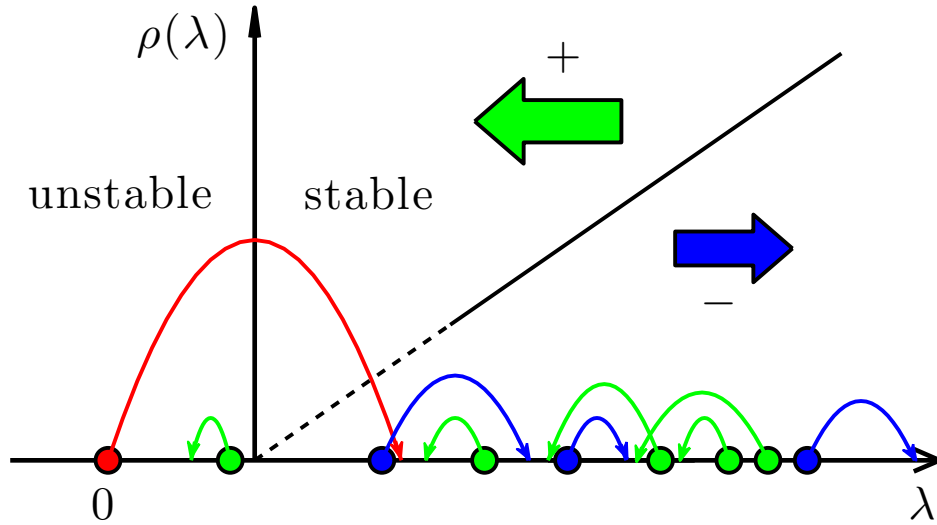


Figure 6.3: Illustration of a step in the dynamics, in the SK model and the random walker model. Circles on the λ -axis represent the spins or walkers. At each step, the most unstable spin (in red) is reflected to the stable side, while all others (in green or blue) receive a kick and move. The dashed and solid line outlines the density profile $\rho(\lambda) \sim \lambda$ for $\lambda > 1/\sqrt{N}$. The blue spins were initially frustrated with the flipping spin 0. They are stabilized and are now unfrustrated with 0. In contrast, green spins become frustrated with spin 0 and are softer now. Because of the motion of spins depends on their frustration with spin 0, a correlation builds up at small λ , leading to an overall frustration of “soft” spins among each other.

6.5 Emergence of Correlations

Equation (6.12) implies that $\gamma = 1$ in Eq. (6.7). Such singular correlations are unexplained⁰. We now argue that they naturally build up in the dynamics through the spin-flip induced motion of stabilities of frustrated and unfrustrated spins, as illustrated in Fig. 6.3. To quantify this effect we define respectively $C_f(\lambda)$

⁰ The approximation Eq. (21) in Horner yields an incorrect scaling behavior for $C(\lambda)$, assuming a pseudogap.

and $C'_f(\lambda)$ as the correlation between the flipping spin 0 and the spins at λ *before* and *after* a flip event. As s_0 flips, the stability of spin i increases by $x_i \equiv -2J_{0i}s_0s_i$, $\lambda'_i = \lambda_i + x_i$. The correlation $C'_f(\lambda)$ is an average over all spins which migrated to λ due to the flip:

$$C'_f(\lambda) = \frac{1}{\rho'(\lambda)} \int \rho(\lambda - x)(-x)f_{\lambda-x}(x)dx,$$

$$\rho'(\lambda) = \int \rho(\lambda - x)f_{\lambda-x}(x)dx.$$

$f_\lambda(x)$ is the Gaussian distribution of kicks x given to spins of stability λ : $f_\lambda(x) = \exp\left[-\frac{(x-C_f(\lambda))^2}{4D/N}\right] / \sqrt{4\pi D/N}$. In the integrands we expand $\rho(\lambda - x)$ and $C_f(\lambda - x)$ for small x and keep terms of order $1/N$, which yields

$$C'_f(\lambda) = -C_f(\lambda) + 2\frac{D}{N} \frac{\partial_\lambda \rho(\lambda)}{\rho(\lambda)}, \quad (6.13a)$$

$$\rho'(\lambda) = \rho(\lambda) - \partial_\lambda \left[C_f(\lambda)\rho(\lambda) - \frac{D}{N}\partial_\lambda \rho(\lambda) \right]. \quad (6.13b)$$

Thus, even if correlations are initially absent, $C_f(\lambda) = 0$, they arise spontaneously, $C'_f(\lambda) = 2D\partial_\lambda \rho(\lambda)/N\rho(\lambda)$.

In the steady state, $\rho'_{ss} = \rho_{ss}$, and Eq. (6.13b) implies the vanishing of the spin flux, that is, Eq. (6.12) with $v = NC_f$. Plugged into Eq. (6.13a), we obtain that the correlations are steady, too,

$$C'_f(\lambda) = C_f(\lambda) = \frac{v_{ss}(\lambda)}{N} = \frac{2\theta}{N\lambda}. \quad (6.14)$$

These correlations are expected once the quasi-statically driven dynamics reaches a statistically steady regime, and thus should be present both during avalanches

and in the locally stable states reached at their end.

Interestingly, Eq. (6.14) implies that all the bounds of Eq. (6.9) are saturated if the first one is, i.e., if $\theta = 1$. The latter value was previously derived from dynamical considerations in Ref. [101]. It is intriguing that the present Fokker-Planck description of the dynamics does not pin θ , as according to Eqs. (6.12, 6.14) any value of θ is acceptable for stationary states. However, additional considerations on the applicability of the Fokker-Planck description discard the cases $\theta > 1$ and $\theta < 1$, as discussed in the Appendix Sec. D.3.

Those are related to the interesting fact that that Eqs. (6.10, 6.11, 6.12) with $\theta = 1$ are equivalent to the Fokker-Planck equation for the radial component of unbiased diffusion in $d = 2$ (as derived in Appendix Sec. D.4), whose statistics is well known [210, 211]. We can use this analogy to predict $F(n)$, the number of times an initially soft spin flips in an avalanche of size n . Indeed, a discrete random walker starting at the origin will visit that point $\ln(t)$ times after t steps in two dimensions, and thus $F(n) \sim \ln(n)$, as supported by Fig. 6.2(b). Similarly we expect times between successive flips of a given spin to be distributed as $P(\delta t) \sim 1/(\delta t [\ln(\delta t)]^2)$.

Short range systems and experiments: In short range spin glasses we expect analogous frustrated correlations between pairs of directly interacting soft spins as in the SK model, except that the growth of correlations at small λ is cut off at the typical coupling between spins. This prediction can be tested in experiments akin to NMR protocols: First flip the spins of stability λ by a π -pulse of appropriate frequency. Then flip those of stability λ' and observe the resulting shift in the fluorescence spectrum around λ . From our findings we predict a systematic shift to higher frequencies.

6.6 Conclusion

We have studied the quasi-static dynamics in a marginally stable glass at zero temperature, focusing on a fully-connected spin glass as a model system. Our central result is that the pseudo-gap appears dynamically due to a strong frustration among the softest spins, characterized by a correlation function $C(\lambda)$ which scales inversely with the stability λ . We provided a Fokker-Planck description of the dynamics that explains the appearance of both the pseudo-gap and the singular correlation, and suggests a fruitful analogy between spin glass dynamics and random walks in two dimensions.

We expect our findings to apply to other marginally stable systems, in particular hard sphere packings that display a pseudo-gap with a non-trivial exponent: $P(f) \sim f^{\theta_e}$ [108, 109, 111, 115] where f is the contact force. Our analysis above suggests that a singular correlation function $C(f) \sim 1/f$ characterizes how contacts are affected by the opening of a contact of very weak force, the relevant excitations in packings [108, 109]. Contacts with small forces should on average be stabilized by $C(f)$ - a testable prediction. Our analysis also suggests a connection between sphere dynamics and random walks in dimension $1 + \theta_e$, which is interesting to explore further.

Chapter 7

Outlooks

7.1 Intermediate Phase

In *Chapter 3*, we have shown that the “rigidity window” picture at zero temperature is not robust in the presence of weak interactions. Mapping the intermediate phase in chalcogenides [43, 45, 46, 48, 49, 74, 77] to a “rigidity window” is thus unsound, as weak non-covalent interactions cannot be excluded in practical systems. Here, we propose an alternative idea to understand the intermediate phase.

We propose the coordination range near z_c , where the boson peak is ill-defined, as the intermediate phase. The boson peak becomes impossible to define as the density of states is filled at the low-frequency end in this range. We can rationalize experimental features of the intermediate phase from this consideration. In one set of the experiments on the elasticity of chalcogenides [46], experimentalists tested the pressure responses of the microscopic structures by measuring the

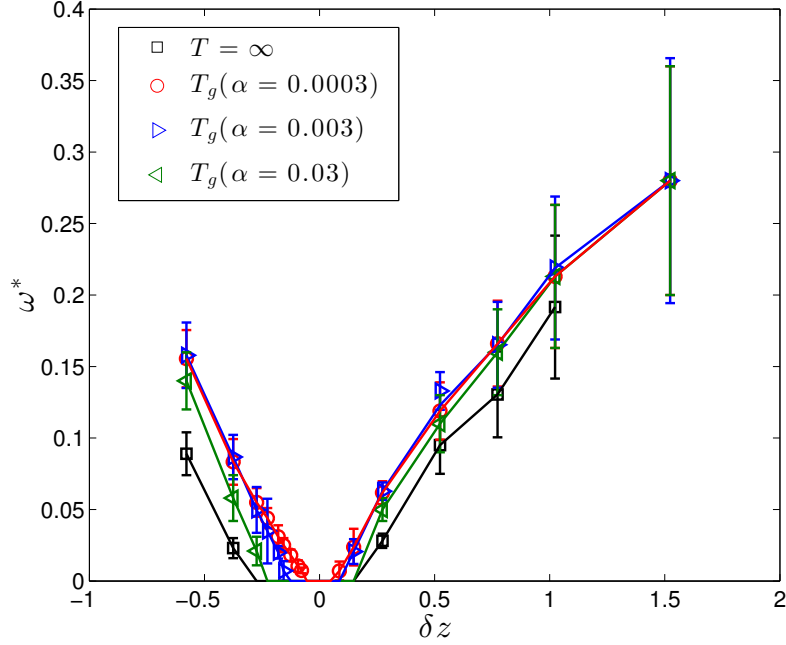


Figure 7.1: Boson peak frequency ω^* obtained from equilibrated configurations near T_g vs coordination number δz for different α .

phonon spectra, especially on the phonon line of corner-sharing tetrahedral units. The corner-sharing units in Ge-Se compounds are made of two Germanium atoms, which share two Selenium atoms connected by covalent bonds. The corresponding frequency in the density of states shifts due to nonlinear responses to the stresses on the units in the bulk. The pressure responses indicate an intermediate phase, in which the frequency begins to shift as soon as the pressure acts on, while out of which the frequency shifts only when the pressure is above a threshold. The intermediate phase defined in this way is consistent with the intermediate phase defined by non-reversal heat [46, 77] Indicated by Eq.(4.6), the elasticity of the covalent network is contributed mostly by the redundant constraints, i.e., self-stressed regions, and by the coupling with the network of weak forces through the

low-frequency modes, $\omega \lesssim \sqrt{\alpha}$. When a stress applies on the material, the structure responses are limited mostly to the corresponding modes. The self-stressed modes are very anisotropic, distortion along which thus does not effect the structure of most corner-sharing units. By contrast, the low-frequency modes are more extended, response of which extends in the bulk. In the vicinity of the rigidity transition, the structures are abundant in these extended low-frequency modes, the pressure easily causes the distortion homogeneously in the bulk and shift the corner-sharing spectral line [46, 160].

We define the range by probing the boson peak frequency ω^* for strong networks equilibrated at T_g in our model. In $D(\omega)/\omega^{d-1-\omega}$ plot, see for example Fig. 3.4(d), a peak becomes ill-defined in a finite range of coordination number near z_c when $\alpha > 0$, shown in Fig. 7.1. This range of boson peak frequency $\omega^* = 0$ is proposed as the intermediate phase. The width of intermediate phase depends on the glass transition temperature and thus on α , as shown in Fig. 7.1. For $\alpha = 0.03$ closest to the real strength of van der Waals interactions, the width of intermediate phase is $\Delta z \approx 0.4$, which is significantly larger than 0.06 obtained in the rigidity window [75, 160], and much closer to the experimental values (approximately $0.1z_c$ [212]). Moreover, this definition of the intermediate phase covers both the floppy and rigid side on the coordination number as empirical observations [212], while the rigidity window appears only on the floppy side [73].

The importance of large homogeneous isostatic clusters to the intermediate phase is similar in both our boson peak definition and the rigidity window picture. However, the rigidity window picture roots on a percolating isostatic cluster, which is fragile under the addition of weak forces and finite-temperature fluctuations. In

contrast, our boson peak picture bases on a mean-field jamming transition, where large isostatic clusters near z_c are induced by finite-temperature fluctuations, which is thus a more robust concept applicable to real glasses. Though isostatic clusters cannot be directly verified, some consequences can be empirically tested. The density of states in the intermediate phase may be measured through a Raman scattering experiment to check the abundance of the low-frequency vibrations; The width dependence on α of the intermediate phase may be studied by network glasses with different electronegativity or even patchy particle glasses [213], where the stiffness of the strong interactions is tunable.

7.2 Dynamical Transition at Finite Temperature

The dynamical phase transition studied in *Chapter 5* is not limited to the erosion. Similar models and simulations have been extensively studied in the context of Type-II superconductors [97, 98, 187, 214–218], where vortices, carrying magnetic flux quanta, play the roles of driven particles. In the system, vortices repelling each other are driven by the flow of current in a randomly pinning substrate of impurities and defects. When the current exceeds the critical value, the flow of vortices induces an electric field and an electric resistance that breaks the superconducting state [219]. Critical behaviors and spatial organizations, predicted in our erosion model, are under test in molecular dynamics simulations of these systems [187, 217]. In general, any system that consists of repulsive particles driven by a directed force on a glassy rough landscape can be modeled in the similar way, and its dynamical transition should fall in the same universality class.

However, in these microscopic systems, when the energy barrier becomes comparable to the temperature or Planck constant, thermal or quantum fluctuations are relevant. We need to include these fluctuations in the model to apply our theoretical framework to the dynamics in these systems. To incorporate the stochastic dynamics into the model, we introduce a control parameter probability p . At each time step, a particle may move to one of its two downhill sites with probability p , independent of the local heights if the target site is not occupied. If this stochastic movement is not executed, the particle will just follow the deterministic rule. The preliminary results from this simplest stochastic rule indicate that the sharp transition becomes a crossover from the force-driving dynamic state above θ_c to a fluctuation-induced creeping state below the threshold θ_c [220].

To further capture the temperature excitation or quantum tunneling in the model, a Monte Carlo dynamics can be introduced to replace the deterministic dynamics. At each time step, a particle randomly moves to any of its four neighbor sites, according to a probability proportional to $\exp[\frac{1}{T}(f_{i \rightarrow j})]$, where $f_{i \rightarrow j}$ is the force at site i to the direction on site j . In the creeping phase, the mean particle current is expected to be proportional to $\exp[-\frac{U_0}{T}(\theta_c/\theta)^\mu]$, where U_0 is a fitting parameter and μ is a critical exponent, in analogy to the creeping dynamics of elastic manifolds [88, 221]. Further numerical works should be done to check this creeping behavior and the universal power law exponent μ .

7.3 Universality of Critical Dynamics

The universal exponents of the critical dynamics in Sherrington-Kirkpatrick model studied in *Chapter 6* appear to be exact fractions. The exponents are defined in the power law distributions of the avalanche size and magnetization change,

$$D(n) = n^{-\tau}d(n/N^\sigma)/\Xi(N); P(S) = S^{-\rho}p(S/N^\beta)/Z(N). \quad (7.1)$$

where $\tau = \rho = 1$, $\sigma = 1$, $\beta = 1/2$, and $\Xi(N) = Z(N) = \ln N$ for greedy dynamics described in *Chapter 6* [104, 197], as well as random dynamics [197] where a random unstable spin is flipped at a step. We have also investigated a peculiar dynamics – reluctant dynamics [222]: at each step, the least unstable spin is chosen to flip. We have found $\tau = 4/3$, $\rho = 3/2$, $\beta = 1$, and $\sigma = 2$ for this dynamics, shown in Figs. 7.2 and 7.3.

We have argued in *Chapter 6*, dynamically, the pseudogap exponent $\theta = 1$. The typical external field increment to trigger an avalanche (to destabilize the least stable spin) is thus $\Delta h \sim \lambda_{\min} \sim N^{-1/(1+\theta)}$. Indicated by the continuous hysteresis loop, Fig. 6.1, the average magnetization changes by an amount proportional to the system size under a finite change of the external field. Therefore, the average magnetization jump in an avalanche is $\langle S \rangle \sim N/\Delta h \sim N^{\theta/(1+\theta)} = N^{1/2}$, which leads to a scaling relation,

$$\beta(2 - \rho) = \frac{1}{2}. \quad (7.2)$$

Due to the random couplings of spins, a spin does not necessarily align with the external field after flip. Assuming the sign is purely random, we find that the typical magnetization jump S for an avalanche of size n then scales as $S \sim n^{1/2}$,

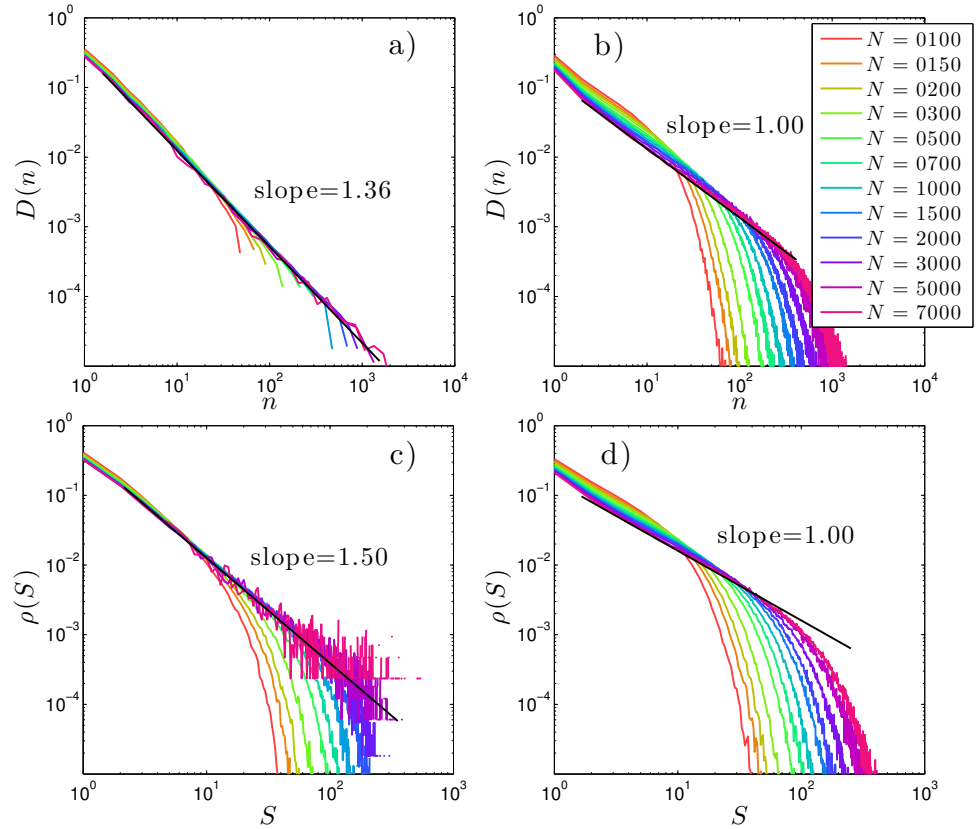


Figure 7.2: (a) (b) Avalanche size distribution $D(n)$; (c) (d) Magnetization jump distribution $\mathcal{P}(S)$. (a) (c) Reluctant dynamics; (b) (d) Greedy dynamics.

which indicates another scaling relation,

$$\beta = \sigma/2. \quad (7.3)$$

With the two scaling relations, four critical exponents are reduced to two independent ones, τ and σ .

To determine the two independent exponents, we assume that τ and σ are purely determined by the avalanche dynamics. We introduce the following dynamic model, based on the stochastic description of the dynamics developed in *Chapter*

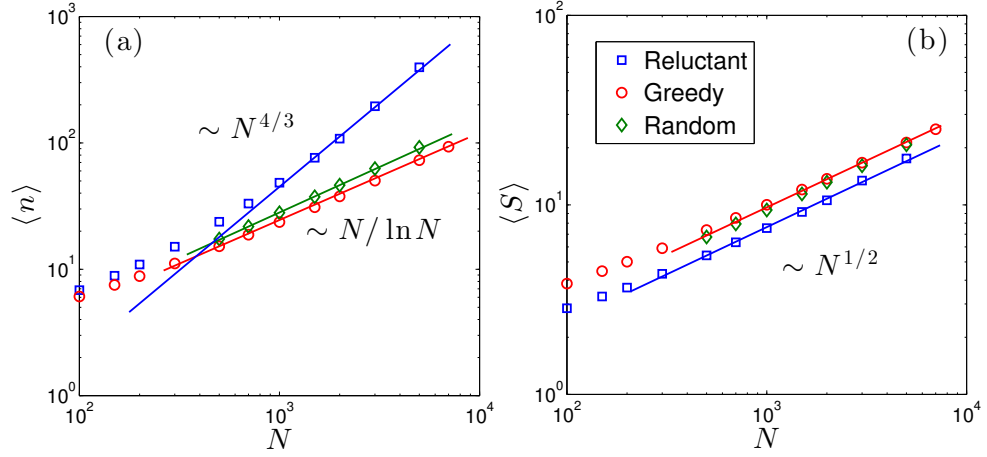


Figure 7.3: (a) Average avalanche size $\langle n \rangle$ (b) Average magnetization jump $\langle S \rangle$ of avalanches.

6. N random walkers in one dimension are characterized by a random variable X . A boundary B separates the axis into an unstable side $x < B$ and a stable side $x > B$. The system stops when unstable random walkers disappear. The boundary plays the role of the quasi-static external field: we retrigger avalanches by setting B to the place between the two least stable walkers after the dynamics stop. At each time step during an avalanche, an unstable walker at $x_0 < B$ leaps to the stable side at $(2B - x_0)$, mimicking the spin flip in SK model. All other walkers take random steps independently, as illustrated in Fig. 7.4,

$$x_i(t+1) - x_i(t) = \frac{1}{N} \left[\frac{2\alpha}{\max(x_i(t) - x_0(t), \epsilon/\sqrt{N})} - \beta x_i(t) + 2\sqrt{N}Z(x_i) - \gamma(t) \right] \quad (7.4)$$

for the walker i at x_i , where $x_0(t)$ is the position of the “flipping” walker at t , $Z(x) \sim \mathcal{N}(0, 1)$. The drift terms resemble the nontrivial correlations, Fig. 6.1(d), between the flipping spin and other spins. The term proportional to α corresponds

to the singular drift at the boundary, which is bounded by \sqrt{N} , and we set $\alpha = \theta = 1$ [120]. The β term limits the walkers from diffusing away but is a less relevant entry at small x . $\gamma(t)$ is a global constraint so that $\sum_{i \neq 0} (x_i(t+1) - x_i(t)) = 0$. We present the results of “flipping” the most unstable walker at each step with $\alpha = 1$, $\beta = 1.5$, and $\epsilon = 1$.

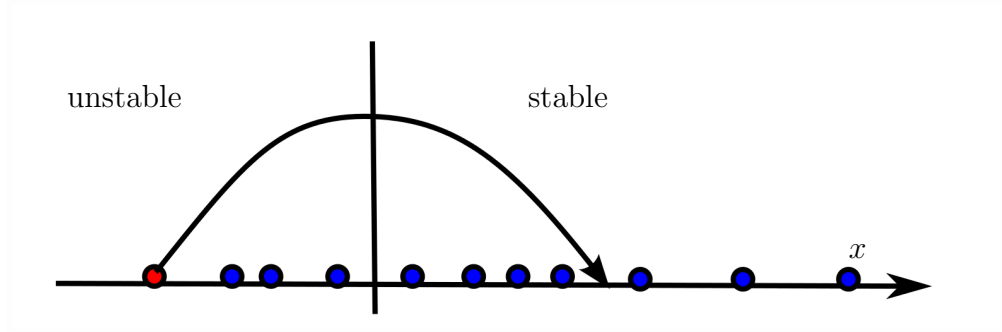


Figure 7.4: Illustration of the dynamic model. Circles on the axis represent the walkers. The leaping walker (in red) jumps to the stable side, and other walkers (in blue) move random steps according to Eq.(7.4).

The stochastic model without any magnetization details reproduces the greedy dynamics where the unstable spins stick close to the boundary. Moreover, the numerical results of the stochastic model indicate avalanches with critical exponents, $\tau = 1$ and $\sigma = 1$, the same as in the greedy dynamics, shown in Fig. 7.5.

The model opens up a possibility of solving for the exponents from a well defined stochastic problem [223]. In addition, pointed out in *Chapter 6*, the stochastic description with a non-trivial correlation among soft excitations applies to jammed packings and other glassy systems. It is then possible to be generalized to solve for the critical exponents of avalanches in different glassy systems by considering the corresponding correlations.

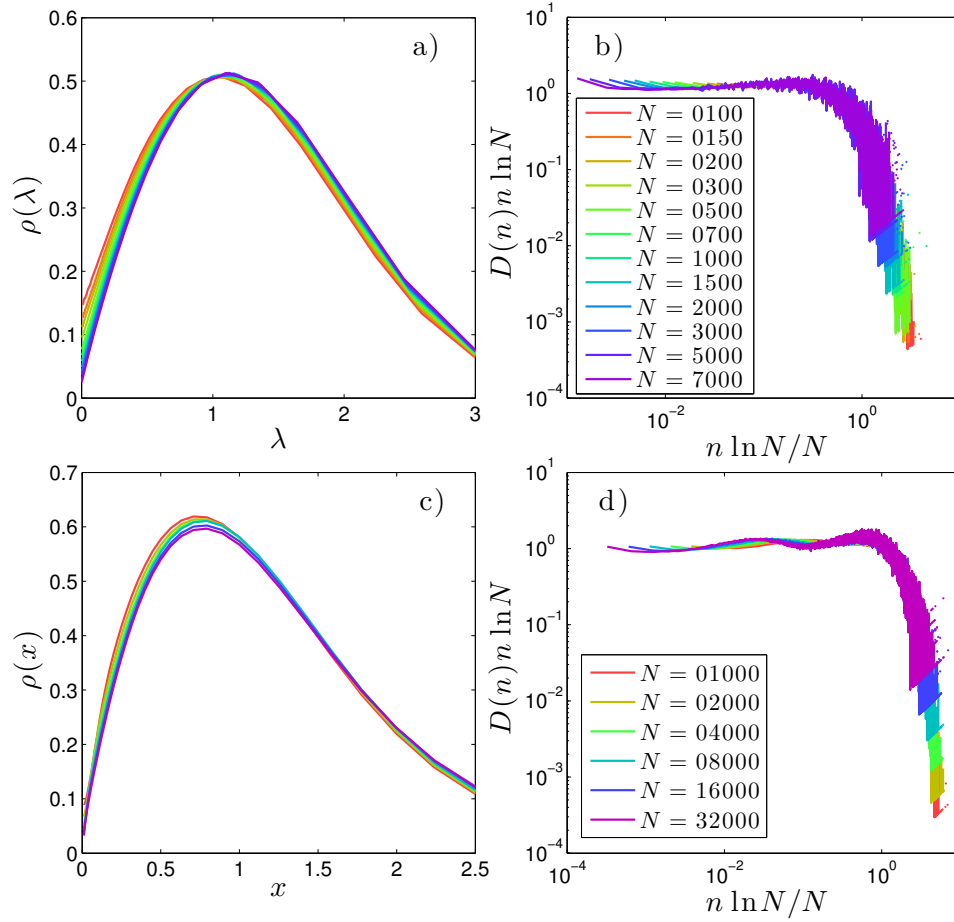


Figure 7.5: (a) (c) Distribution of local stability $\rho(\lambda)$ in stable states and (b) (d) Distribution of avalanche size $D(n)$ scaled by finite size N for (a) (b) SK model and (c) (d) random walker model. In the pseudo-gap near $\lambda = 0$, $\rho(\lambda) \propto \lambda$ in both (a) and (c). The collapses in (b) and (d) indicate the power law exponent $\tau = 1.0$, and $\sigma = 1$ with a logarithmic correction.

Chapter 8

Conclusion

In this dissertation, we have investigated several topics on the dynamics of glassy systems. The glass transition comes about as the dynamics rapidly slow down under cooling [1, 2]. We have proposed an explanation for the correlation between the rapidity of slowing-down of glasses and the elasticity of their microscopic structures, by introducing novel network-glass models. Next, at zero temperature, a frozen glassy system becomes dynamic under a strong-enough driving force. We have proposed a model incorporating the interplay between disorder and particle interaction to describe the erosion of the river bed, which shows a dynamical phase transition with testable predictions associated to a new universality class. Finally, many athermal glassy systems self-organize to show critical dynamics under quasi-static drives [7, 8]. The critical dynamics are results of a pseudogap of soft excitations in the systems with long-range effective interactions [101]. We have done a case study of a spin glass system and developed a general stochastic description of the dynamics where the correlation and the pseudogap emerge

spontaneously.

Self-organization plays a key role in all three topics. Network glasses self-organize at low temperature due to the existence of the weak constraints, which reduces the spatial fluctuations of covalent bonds, leading to mean-field like networks. As the result, the predictions of the thermodynamics and dynamics based on the frozen elastic networks obeying mean-field rigidity transition hold true near the glass transition even though the interaction networks are adaptive in real liquids. This result raises questions on the validity of mean-field approaches in other supercooled liquids at low temperature, which appear to apply in particular near the jamming transition.

In the erosion of river beds, self-organization appears in form of “armoring” of the surface, for which, the “holes” are filled up, leading to a subtle power-law distribution of the spatial organization of flux near the threshold. The results can be well generalized to other systems of short-range repelling particles driven by a external forcing on a random pinning substrate. Type-II superconductors are relevant examples, where magnetic quanta are driven by the electric current and pinned by impurities or defects in the substrate. Similar to the erosion, the “armoring” of the random pinning spots will end up with a spatial organization of flux of the magnetic quanta, which has also been overlooked in the relevant literature. Experimental works [83] are currently testing our views.

Finally, the other set of athermal glassy systems with long-range, frustrated interactions also self-organizes under a quasi-static drive, which leads to marginal states, with pseudogaps and crackling responses. We have explained these phenomena dynamically with a stochastic-kinetic description in the mean-

field spin glass. A challenge for the future is to generalize the description to other self-organizing systems, where the interactions are more practical ones, for example, power-law decaying, instead of fully-connected.

Appendices

Appendix A

Why glass elasticity affects the thermodynamics and fragility of super-cooled liquids?

A.1 Stiffness and Coupling matrices

Consider a network of N nodes connected by N_c springs. If an infinitesimal displacement field $|\delta\mathbf{R}\rangle$ is imposed on the nodes, the change of length of the springs can be written as a vector $|\delta r\rangle$ of dimension N_c . For small displacements this relation is approximately linear: $|\delta r\rangle = \mathcal{S}|\delta\mathbf{R}\rangle$, where \mathcal{S} is an $N_c \times Nd$ matrix. To simplify the notation, we write \mathcal{S} as an $N_c \times N$ matrix of components of dimensions d , which gives $\mathcal{S}_{\gamma,i} \equiv \partial r_\gamma / \partial \mathbf{R}_i = \delta_{\gamma,i} \mathbf{n}_\gamma$, where $\delta_{\gamma,i}$ is non-zero only if the contact γ includes the particle i , and \mathbf{n}_γ is the unit vector in the direction of the contact γ , pointing toward the node i . Using the bra-ket notation, we can

rewrite $\mathcal{S} = \sum_{\langle ij \rangle \equiv \gamma} |\gamma\rangle \mathbf{n}_\gamma (\langle i| - \langle j|)$, where the sum is over all the springs of the network. Note that the transpose \mathcal{S}^t of \mathcal{S} relates the set of contact forces $|f\rangle$ to the set $|\mathbf{F}\rangle$ of unbalanced forces on the nodes: $|\mathbf{F}\rangle = \mathcal{S}^t |f\rangle$, which simply follows from the fact that $\mathbf{F}_i = \sum_\gamma \delta_{\gamma,i} f_\gamma \mathbf{n}_\gamma = \sum_\gamma f_\gamma \mathcal{S}_{\gamma,i}$ [64].

The stiffness matrix $\tilde{\mathcal{M}}$ is a linear operator connecting external forces to the displacements: $\tilde{\mathcal{M}}|\delta\mathbf{R}\rangle = |\mathbf{F}\rangle$. Introducing the $N_c \times N_c$ diagonal matrix \mathcal{K} , whose components are the spring stiffnesses $\mathcal{K}_{\gamma\gamma} = k_\gamma$, we have for harmonic springs $|f\rangle = \mathcal{K}|\delta r\rangle$. Applying \mathcal{S}^t on each side of this equation, we get $|\mathbf{F}\rangle = \mathcal{S}^t |f\rangle = \mathcal{S}^t \mathcal{K} \mathcal{S} |\delta\mathbf{R}\rangle$, which thus implies [64]:

$$\tilde{\mathcal{M}} = \mathcal{S}^t \mathcal{K} \mathcal{S}.$$

Let us assume that starting from a configuration where all springs are at rest, the rest lengths of the springs are changed by some amount $|y\rangle$. This will generate an unbalanced force field $|\mathbf{F}\rangle = \mathcal{S}^t \mathcal{K} |y\rangle$ on the nodes, leading to a displacement $|\delta\mathbf{R}\rangle = \tilde{\mathcal{M}}^{-1} \mathcal{S}^t \mathcal{K} |y\rangle$. The elastic energy $\mathcal{E} = \frac{1}{2} \langle y - \delta r | \mathcal{K} | y - \delta r \rangle$ is minimal for this displacement and the corresponding energy $\tilde{\mathcal{H}}$ is:

$$\tilde{\mathcal{H}}(|y\rangle) = \frac{1}{2} \langle y | \mathcal{K} - \mathcal{K} \mathcal{S} \tilde{\mathcal{M}}^{-1} \mathcal{S}^t \mathcal{K} | y \rangle. \quad (\text{A.1})$$

In our model, $y_\gamma = 0$ for weak springs and $y_\gamma = \epsilon \sigma_\gamma$ for strong springs of stiffness k , implying that $\mathcal{K} |y\rangle = k |y\rangle$. Introducing the dimensionless stiffness matrix $\mathcal{M} \equiv \tilde{\mathcal{M}}/k$ and the restriction \mathcal{S}_s^t of the operator \mathcal{S}^t on the subspace of strong contacts

of dimension N_s , i.e. $\mathcal{S}_s^t|\sigma\rangle \equiv \mathcal{S}^t|y\rangle$, Eq.(A.1) yields:

$$\mathcal{H}(|\sigma\rangle) = \frac{1}{2}\langle\sigma|\mathcal{G}|\sigma\rangle \text{ where } \mathcal{G} = \mathcal{I} - \mathcal{S}_s\mathcal{M}^{-1}\mathcal{S}_s^t,$$

where \mathcal{I} is the identity matrix, and \mathcal{G} is the coupling matrix used in *Chapter 2*. Note that in our model the diagonal matrix \mathcal{K} contains only two types of coefficients k_w and k , corresponding to the stiffnesses of weak springs and stiff springs respectively. Then the dimensionless stiffness matrix can be written as $\mathcal{M} = \mathcal{S}_s^t\mathcal{S}_s + \frac{k_w}{k}\mathcal{S}_w^t\mathcal{S}_w$, where \mathcal{S}_w^t is the projection of the operator \mathcal{S}^t on the subspace of weak contacts.

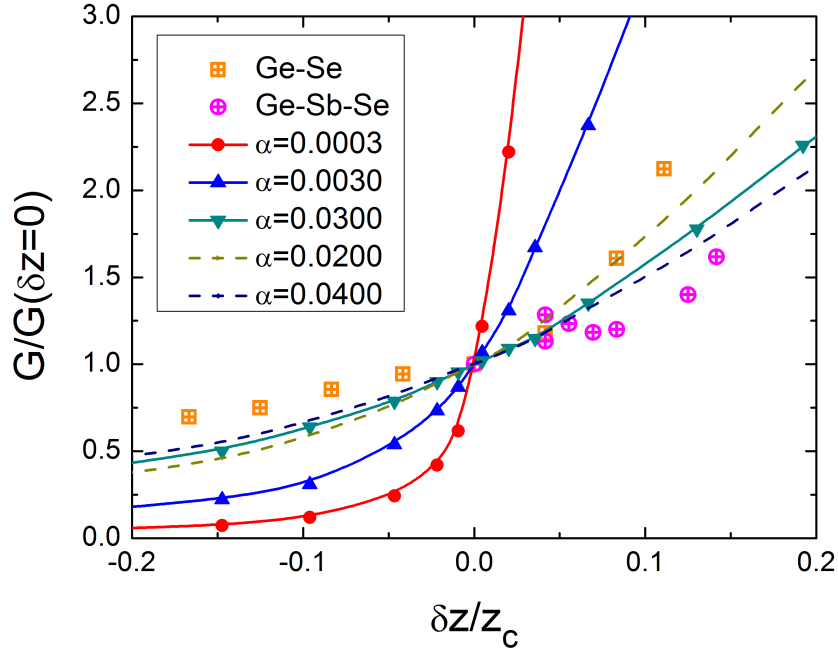


Figure A.1: Squares show the shear modulus G normalized by its value at the rigidity threshold for Ge-Se, taken from Ref. [36]. Circles show G for Ge-Sb-Se, taken from Ref. [37]. Lines display the shear modulus G for network models in $d = 3$ using different α , as indicated in the legend.

A.2 Shear modulus of the random elastic networks

An explicit expression for the shear modulus G of an elastic network can be found using linear response theory [65, 66]. In particular, let us consider the shear on the (x, y) plane. In the contact vector space, a shear strain can be written as $\delta|y^{sh}\rangle$ with $\delta \ll 1$ which represents the amplitude of the strain and $|y^{sh}\rangle$ corresponds to a unit shear strain. The components of $|y^{sh}\rangle$ are given by $y_\gamma^{sh} = \frac{\Delta x_\gamma \Delta y_\gamma}{l_\gamma}$, where l_γ is the rest length of the spring γ , and Δx_γ and Δy_γ are its projections along the x and y directions. From the last section (A), we can obtain the total energy induced by a shear strain $\tilde{\mathcal{H}}(|y^{sh}\rangle)\delta^2$; hence the shear modulus $G = 2\tilde{\mathcal{H}}(|y^{sh}\rangle)/V$.

To estimate the value of α , we consider the dependence of the shear modulus with coordination or valence in the vicinity of the rigidity transition, which is smooth for large α and sudden for small α in our networks, see Fig. A.1. Comparing networks and real chalcogenide glasses we find that the cross-over in the elastic modulus is qualitatively reproduced for $\alpha \in [0.01, 0.05]$.

A.3 Finite size effects on fragility

To estimate the role of finite size effects on the dynamics, we use two different system sizes $N = 64$ and $N = 256$. As shown in Fig. 2.2, the Angell plot for the relaxation time, and therefore our estimation of the fragility, appears to be nearly independent of the system size. Note, however, that the correlation function

$C(t)$ shows some finite size effects very close to the isostatic point ($z = z_c, \alpha = 0$), but that it does not affect our measure of τ significantly. In particular we find that near isostaticity, the distribution of relaxation time is broad for small systems, and becomes less and less so when the system size increases. We noticed that this effect also disappears if a two-spin flips Monte-Carlo is used, instead of the one-spin flip algorithm we perform.

A.4 Fragility in experimental dynamical range

The value of fragility depends on the definition of glass transition, in particular on the dynamical range. In super-cooled liquids the glass transition occurs when the relaxation time is about 10^{16} larger than the relaxation time at high temperature. Thus the dynamical range in experiments (which corresponds to the fragility of a perfectly Arrhenius liquid) is $R = 16$. In our simulation, the same quantity is $R = 5$. It is possible however to rescale our values of fragility to compare with experimental data, if we extrapolate the dynamics. We shall assume a Vogel-Fulcher-Tammann (VFT) relation at low temperature,

$$\log_{10} \frac{\tau(T)}{\tau_0} = \frac{A}{T - T_0},$$

We define the dynamical range as:

$$R = \log_{10} \frac{\tau(T_g)}{\tau_0} = \frac{A}{T_g - T_0}.$$

Thus we can express the fragility as:

$$m_R = \left. \frac{\partial \log_{10} \tau(T)/\tau_0}{\partial T_g/T} \right|_{T=T_g} = R + R^2 \frac{T_0}{A}. \quad (\text{A.2})$$

T_0 and A are assumed to be independent of dynamical range. Using the notation $m = m_5$ and $m_{sc} = m_{16}$ we get from Eq.(A.2):

$$m_{sc} = 16 + \frac{16^2}{5^2}(m - 5) = 10.24m - 35.2$$

The amplitude of fragility we find turn out to be comparable to experiments when $\alpha = 0.03$, in particular for $z \geq z_c$. For the smallest coordination explored our results underestimate somewhat the fragility, slightly above 50 in our model and about 80 experimentally. This is not surprising considering that our model is phenomenological, and the extrapolation we made to compare different dynamical ranges.

A.5 Theory in appearance of weak springs

In the case where $\alpha \neq 0$, the annealed free energy can be easily calculated under the assumption that $|\delta r_p\rangle$ and $|\delta r_\omega\rangle$ are random Gaussian vectors. The Hamiltonian in Eq.(2.10) can be rewritten as:

$$\mathcal{H} = \frac{1}{2} \sum_{p=1 \dots \delta z N/2} X_p^2 + \frac{1}{2} \sum_{\omega>0} \frac{\alpha}{\alpha + \omega^2} X_\omega^2,$$

where $X_p = \langle \delta r_p | \sigma \rangle$ and $X_\omega = \langle \delta r_\omega | \sigma \rangle$ represent independent random variables for each configuration $|\sigma\rangle$. In the thermodynamic limit the random variables X_p

and X_ω are Gaussian distributed with zero mean and unit variance. The averaged partition function is given by:

$$\begin{aligned}\bar{Z} &= 2^{N_s} \int e^{-\mathcal{H}/T} \prod_p \frac{e^{-\frac{x_p^2}{2}}}{\sqrt{2\pi}} dX_p \prod_\omega \frac{e^{-\frac{x_\omega^2}{2}}}{\sqrt{2\pi}} dX_\omega \\ &= 2^{N_s} \prod_{p=1}^{\delta z N/2} \left(1 + \frac{1}{T}\right)^{-1/2} \prod_{\omega>0} \left(1 + \frac{\alpha/T}{\alpha + \omega^2}\right)^{-1/2}.\end{aligned}$$

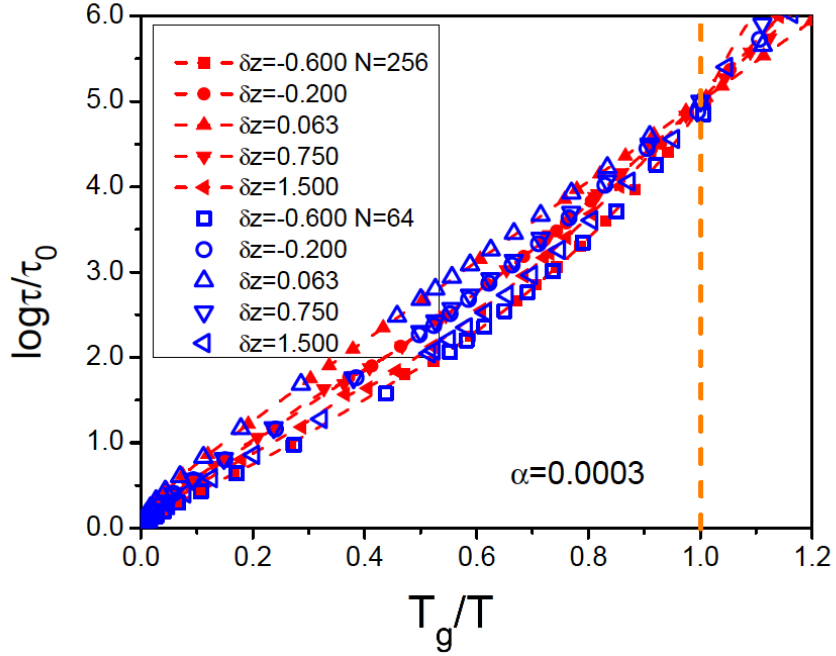


Figure A.2: Angell plot representing $\log \tau$ *v.s.* inverse temperature T_g/T for different δz and two system sizes $N = 64$ and $N = 256$, $\alpha = 0.0003$.

From the average partition function the density of free energy per spring $f(T)$ and any other thermodynamic quantities are readily computed. In particular, the energy density $\varepsilon(T)$, the specific heat $c(T)$ and the entropy density $s(T)$ write:

$$\begin{aligned}
f(T) &= \frac{T}{2N_s} \left[\sum_{p=1}^{\delta z N/2} \ln \left(1 + \frac{1}{T} \right) + \sum_{\omega>0} \ln \left(1 + \frac{\alpha/T}{\alpha + \omega^2} \right) \right] - T \ln 2 \\
\varepsilon(T) &= \frac{1}{2N_s} \left[\sum_{p=1}^{\delta z N/2} \frac{T}{1+T} + \sum_{\omega>0} \frac{\alpha T}{\alpha + (\omega^2 + \alpha)T} \right] \\
c(T) &= \frac{1}{2N_s} \left[\sum_{p=1}^{\delta z N/2} \frac{1}{(1+T)^2} + \sum_{\omega>0} \left(\frac{\alpha}{\alpha + (\omega^2 + \alpha)T} \right)^2 \right] \\
s(T) &= \ln 2 - \frac{1}{2N_s} \sum_{p=1}^{\delta z N/2} \left[\ln \left(1 + \frac{1}{T} \right) - \frac{1}{1+T} \right] \\
&\quad - \frac{1}{2N_s} \sum_{\omega>0} \left[\ln \left(1 + \frac{\alpha/T}{\alpha + \omega^2} \right) - \frac{\alpha}{\alpha + (\omega^2 + \alpha)T} \right].
\end{aligned} \tag{A.3}$$

In the limit $\alpha \rightarrow 0$, for any finite temperature T , the sum over the vibration modes ($\omega > 0$) vanishes, and we recover the expressions in the absence of weak springs for pure rigid networks. Note that Eq.(A.3) corresponds to Eq.(2.11) in the article.

A.6 Continuous density of states limit: Analytical results

In the thermodynamic limit $N \rightarrow \infty$, we can replace the sum over frequencies by an integral: $\sum_{\omega>0} \rightarrow N_s \int d\omega D(\omega)$ for $\delta z \leq 0$, and $\sum_{\omega>0} \rightarrow Nd \int d\omega D(\omega)$ for $\delta z > 0$. The density of states $D(\omega)$ is the distribution of vibrational modes of random elastic networks, which has been computed theoretically [78, 127, 132].

There are two frequency scales in the random network : $\omega^* \sim |\delta z|$ above which a plateau of soft modes exist, and a cut-off frequency $\omega_c \sim 1$. Below ω^* , rigid networks show plane wave modes [127, 130, 132] with a characteristic Debye regime $D(\omega) \sim \omega^2$, unlike floppy networks, which show no modes in this gap [78].

It turns out that the Debye regime contribution to the integrals is negligible near the jamming threshold. To capture the scaling behavior near jamming, we approximate $D(\omega)$ by a square function. This simplified description allows further analytical progress while preserving the same qualitative behavior. Since the Debye regime can be neglected, we choose:

$$D(\omega) = \begin{cases} \frac{1}{\omega_c - \omega^*} & \omega^* \leq \omega \leq \omega_c \quad \delta z \leq 0 \\ \frac{1}{\omega_c} & 0 \leq \omega \leq \omega_c \quad \delta z > 0. \end{cases}$$

Considering $\omega^* = \frac{|\delta z|}{z_c} \omega_c$, the cut-off frequency $\omega_c \sim 1$ is the only fitting parameter of the simplified continuum model. Rescaling as $\alpha \rightarrow \alpha \omega_c^2$, we obtain that all the thermodynamic functions depend uniquely on $\alpha = \frac{z_w k_w}{dk \omega_c^2}$, T and δz . In particular, the specific heat is:

$$c(T, \delta z, \alpha) = \begin{cases} \frac{z_c \sqrt{\alpha(1+1/T)}}{4z(1+T)^2} \left[\arctan\left(\frac{1}{\sqrt{\alpha(1+1/T)}}\right) \right. \\ \quad \left. + \frac{\sqrt{\alpha(1+1/T)}}{1+\alpha(1+1/T)} + \arctan\left(\frac{\delta z/z_c}{\sqrt{\alpha(1+1/T)}}\right) \right. \\ \quad \left. + \frac{\delta z}{z_c} \frac{\sqrt{\alpha(1+1/T)}}{\delta z^2/z_c^2 + \alpha(1+1/T)} \right] & \delta z \leq 0 \\ \\ \frac{z_c \sqrt{\alpha(1+1/T)}}{4z(1+T)^2} \left[\arctan\left(\frac{1}{\sqrt{\alpha(1+1/T)}}\right) \right. \\ \quad \left. + \frac{\sqrt{\alpha(1+1/T)}}{1+\alpha(1+1/T)} \right] + \frac{\delta z}{2z} \frac{1}{(1+T)^2} & \delta z > 0. \end{cases}$$

We compute the jump of specific heat at the Kautzman temperature, where the entropy vanishes $s(T_K, \delta z, \alpha) = 0$. In the continuous limit, the equations for T_K can be approximated by:

$$\ln 2 \approx \frac{z_c}{2z} \left[\ln\left(1 + \frac{\alpha}{T_K}\right) + 2\sqrt{\frac{\alpha}{T_K}} \arctan \sqrt{\frac{T_K}{\alpha}} \right] - \frac{\delta z}{2z} \theta(\delta z) \ln T_K,$$

where the conditions $\delta z \ll z_c$ and $\alpha \sim k_w/k \ll 1$ have been used. There is no simple analytical expression for T_K , however, one can observe the existence of two asymptotic regimes: $T_K \sim \alpha$ for $\delta z \ll |1/\ln \alpha|$ and $T_K \sim 2^{-2z/\delta z}$ for $\delta z \gg |1/\ln \alpha|$. Then the specific heat at the transition temperature is given by:

$$c(T_K, \delta z, \alpha) \sim \begin{cases} \frac{z_c \pi}{4z} & \delta z \ll |1/\ln \alpha| \\ \\ \frac{\delta z}{2z} & \delta z \gg |1/\ln \alpha|. \end{cases}$$

From these asymptotic behaviors one gets that the specific heat display a non-

monotonous behavior with coordination, with a minimum whose position scales as
 $\delta z \sim |1/\ln \alpha|$.

Appendix B

Evolution of covalent networks under cooling

B.1 Periodic distortion of triangular lattice.

In our model, we introduce a slight distortion of the lattice to remove the straight lines that occur in a triangular lattice, in the spirit of [63]. Such straight lines would lead to unphysical localized floppy modes orthogonal to the lines. In [63] random disorder is introduced to achieve this goal. Instead, we seek to distort the lines while avoiding frozen disorder (the only disorder we use corresponds to the polydispersity of the spring rest length, but it does not break translational symmetry because springs can move). We group nodes by four, labeled as A B C D in Fig. B.1. One group forms a cell of our crystalline lattice. Each cell is distorted identically as follows: node A stays in place, while nodes B, C, and D move by some distance δ : B along the direction perpendicular to BC, C along the

direction perpendicular to CD, and D along the direction perpendicular to DB, as illustrated in the figure. δ is set to 0.2.

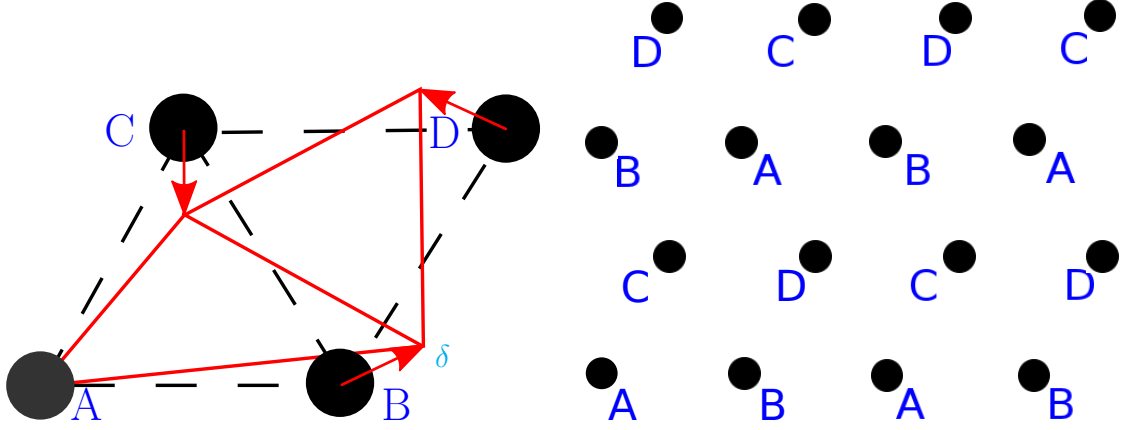


Figure B.1: Illustration of distortion of the triangular lattice, performed to remove straight lines.

B.2 Numerical computation of the elastic energy.

The energy $H(\Gamma)$ of a given spring configuration $\Gamma \equiv \{\gamma \leftrightarrow \langle i, j \rangle\}$ is defined in Eq.(3.1) in *Chapter 3* as a minimization on the positions of the nodes. This minimum can be calculated using conjugate gradient methods. However for small mismatches ϵ , it is more efficient to use linear algebra [116], as we now recall. Consider a displacement field $\delta\vec{R}_i \equiv \vec{R}_i - \vec{R}_{i0}$, where \vec{R}_{i0} is the position of the node i in the crystal described in the previous section. We define the distance $\|\vec{R}_{i0} - \vec{R}_{j0}\| \equiv r_{\langle i, j \rangle}$. At first order in $\delta\vec{R}_i$, the distance among neighboring nodes

can be written as:

$$\|\vec{R}_i - \vec{R}_j\| = r_{\langle i,j \rangle} + \sum_k \mathcal{S}_{\langle i,j \rangle, k} \delta \vec{R}_k + o(\delta \vec{R}^2) \quad (\text{B.1})$$

Where \mathcal{S} is the structure matrix, which gives the linear relation between displacements and changes of distances, as indicated in Eq.(B.1). Minimizing Eq.(3.1) in *Chapter 3* leads to [116]:

$$H(\Gamma) = \frac{k}{2} \sum_{\gamma, \rho} \epsilon_\gamma \mathcal{G}_{\gamma, \rho} \epsilon_\rho + o(\epsilon^3) \quad (\text{B.2})$$

where $\mathcal{G} = \mathcal{S}(\mathcal{S}^t \mathcal{S} + \alpha \mathcal{I})^{-1} \mathcal{S}^t$, and \bullet^t is our notation for the transpose of a matrix. In practice, we solve Eq.(B.2) for every configuration Γ our Monte Carlo considers. One issue with Eq.(B.2) is that the inverse in the expression for \mathcal{G} is ill-defined when $\alpha = 0$ if floppy modes are present in the network. To study the case $\alpha = 0$, we implement the Pebble Game algorithm [63, 163] to distinguish stressed, hyperstatic clusters from floppy or isostatic regions. Since only the stressed regions can contribute to the energy, we reduce the matrix \mathcal{S} to this associated subspace, and solve Eq.(B.2) in this subspace. We have compared this method and a direct minimization via conjugate gradients; the two results coincide within 1% as long as $\epsilon \lesssim 0.01$. In *Chapter 3*, our results are based on Eq.(B.2), and thus hold as long as ϵ is small enough. In this case the choice of ϵ only affects the energy scale.

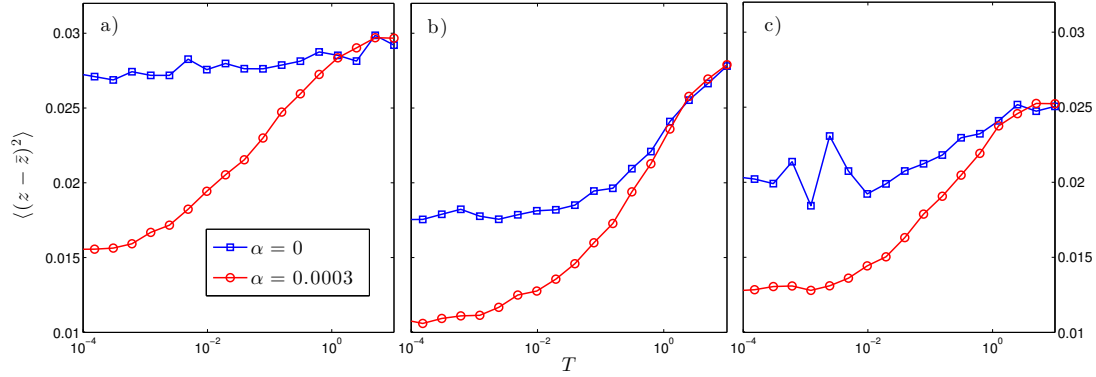


Figure B.2: Fluctuations of coordination $\langle (z - \bar{z})^2 \rangle$ vs temperature T for different α as indicated in legend. The network size is $N = 256$ and the block size is $N^* = 64$. Mean coordination number corresponds to a) $\bar{z} - z_c = -0.383$, b) $\bar{z} - z_c = -0.055$, c) $\bar{z} - z_c = 0.523$.

B.3 Removal of fluctuations under cooling: numerical evidence

The mean coordination number of the whole network is fixed in our model; in this section we denote it as \bar{z} . To characterize spatial fluctuations of coordination, we divide the network into four identical blocks of size $N^* = N/4$ sites. We then measure the coordination number z in each block, and in many configurations equilibrated at some temperature T . We then compute the variance $\langle (z - \bar{z})^2 \rangle$, where the average is over all blocks and configurations. Fig. B.2 shows this quantity versus temperature for three choices of excess coordination $\delta z = \bar{z} - z_c$, corresponding to a) below c) above and b) near the rigidity transition. For all these choices we find that the amplitude of fluctuations does not vary for low temperatures when $\alpha = 0$. By contrast when $\alpha > 0$, fluctuations of coordination are smaller at low

temperature, where they continue to decay under cooling.

B.4 Effect of frozen-in fluctuations of coordination at T_g

To study the role of frozen-in spatial fluctuations of coordination, we increase T_g in our model, which can be achieved by increasing the strength of weak interactions α . We can equilibrate our system up to temperatures of order $T = \alpha$, and in what follows we fix these two parameters to be equal. We then study the vibrational properties of the network of strong springs by computing the boson peak frequency ω^* , defined as in *Chapter 3* as the maximum of $D(\omega)/\omega^{d-1}$. If we observe no maximum in this quantity we posit that $\omega^* = 0$. Results are shown in Fig. B.3. The key point is that as T_g increases, a broader region appears in the vicinity of z_c where mean-field predictions do not apply. Instead one finds that for a range of coordination, $\omega^* \approx 0$, consistent with the presence of fractons.

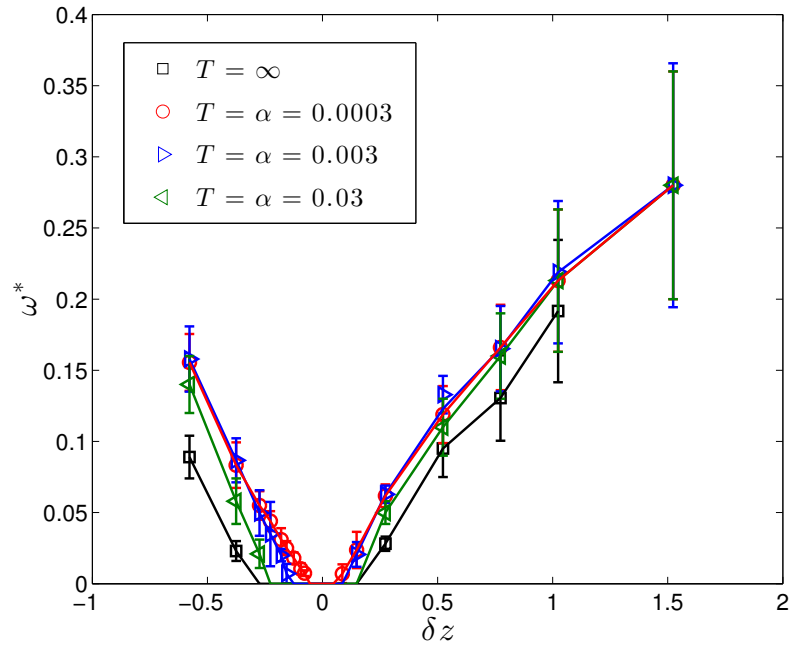


Figure B.3: Boson peak frequency ω^* as a function of excess coordination $\delta z = z - z_c$ for different α as indicated in legend, at temperatures $T = \alpha$. $\omega^* = 0$ indicates that no maximum was observed in $D(\omega)/\omega^{d-1}$, consistent with the presence of fractons at very low frequency.

Appendix C

Adaptive elastic networks as a model for supercooled liquids

C.1 Formalism of elastic energy

The energy $H(\Gamma)$ of a given spring configuration $\Gamma \equiv \{\gamma \leftrightarrow \langle i, j \rangle\}$ is defined in Eq.(4.1) in *Chapter 4* as a minimization on the positions of the nodes. This minimum can be calculated using conjugate gradient methods. However for small mismatches ϵ , it is more efficient to use linear algebra [116], as we now recall. Consider a displacement field $\delta\vec{R}_i \equiv \vec{R}_i - \vec{R}_{i0}$, where \vec{R}_{i0} is the position of the node i in the crystal described in the previous section. We define the distance $\|\vec{R}_{i0} - \vec{R}_{j0}\| \equiv r_{\langle i, j \rangle}$. At first order in $\delta\vec{R}_i$, the distance among neighboring nodes can be written as:

$$\|\vec{R}_i - \vec{R}_j\| = r_{\langle i, j \rangle} + \sum_k \mathcal{S}_{\langle i, j \rangle, k} \delta\vec{R}_k + o(\delta\vec{R}^2) \quad (\text{C.1})$$

Where \mathcal{S} is the structure matrix, which gives the linear relation between displacements and changes of distances, as indicated in Eq.(C.1). Minimizing Eq.(4.1) in *Chapter 4*, one gets:

$$H(\Gamma) = \min_{\{\delta\vec{R}_i\}} \left\{ \frac{k}{2} \sum_{\gamma} \left(\sum_i \mathcal{S}_{\gamma,i} \delta\vec{R}_i + \epsilon_{\gamma} \right)^2 + \frac{k}{2} \sum_{\sigma} \frac{k_w}{k} \left(\sum_i \mathcal{S}_{w,\sigma,i} \delta\vec{R}_i \right)^2 + o(\delta\vec{R}^3) \right\}$$

$$= \min_{\{\delta\vec{R}_i\}} \frac{k}{2} \left[\langle \epsilon | \mathcal{P} | \epsilon \rangle + 2 \langle \epsilon | \mathcal{S} | \delta\vec{R} \rangle + \langle \delta\vec{R} | \mathcal{M} | \delta\vec{R} \rangle \right] \quad (\text{C.2})$$

where we use bra-ket notations to indicate summation over edges or nodes, \mathcal{P} projects the edge space to the subspace occupied by springs, $\mathcal{M} \equiv \mathcal{S}^t \mathcal{S} + \frac{k_w}{k} \mathcal{S}_w^t \mathcal{S}_w$ is the stiff matrix connecting the responding forces and displacements of nodes in an elastic network [64], and \bullet^t is our notation for the transpose of a matrix. Solving Eq.(C.2), one finds the linear response,

$$|\delta\vec{R}\rangle = -\mathcal{M}^{-1} \mathcal{S}^t |\epsilon\rangle \quad (\text{C.3})$$

which for a given mismatch field $|\epsilon\rangle$ minimizes the elastic energy in Eq.(4.1). Inserting Eq.(C.3) back into the linear approximation Eq.(C.2), we have [116]:

$$H(\Gamma) = \frac{k}{2} \langle \epsilon | \mathcal{P} - \mathcal{S} \mathcal{M}^{-1} \mathcal{S}^t | \epsilon \rangle = \frac{k}{2} \sum_{\Gamma} \epsilon_{\langle i,j \rangle} \mathcal{G}_{\langle i,j \rangle, \langle l,m \rangle} \epsilon_{\langle l,m \rangle} \quad (\text{C.4})$$

with $\mathcal{G} = \mathcal{P} - \mathcal{S}(\mathcal{S}^t \mathcal{S} + \frac{k_w}{k} \mathcal{S}_w^t \mathcal{S}_w)^{-1} \mathcal{S}^t$, and $\epsilon_{\langle i,j \rangle} = \epsilon_{\gamma}$ for $\Gamma = \{\gamma \leftrightarrow \langle i, j \rangle\}$.

C.2 Density of states

We have shown the density of states converges to the one of mean-field networks [117]. Cooling strongly suppresses low frequency vibrational modes, as seen in Fig. C.1. This temperature effect on the density of states is primarily induced by the weak interactions: the density of states changes little under cooling when $\alpha = 0$, as appeared in comparing (a) and (b) of Fig. C.2. The slight change indicates that density of states depends on the presence of redundant constraints. However, when $\alpha > 0$, the low temperature density of states strongly differs from its high temperature counterpart, as shown in Fig. C.2(a) and (c).

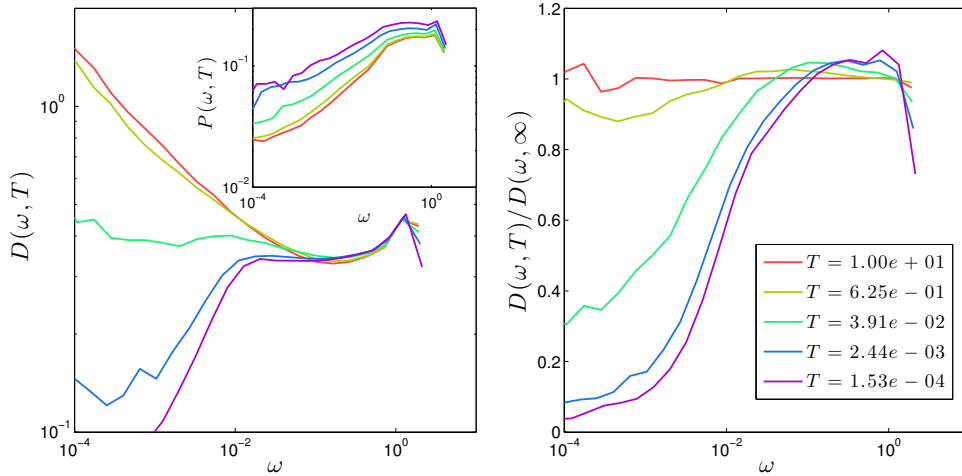


Figure C.1: Variation of density of states $D(\omega, T)$ with temperature for the same $z = -0.055$, $\alpha = 0.0003$. Left: density of states in log-log scale. Right: density of states normalized by its $T = \infty$ value, emphasizing its difference under cooling. Inset: participation ratio $P(\omega, T)$ variation under cooling.

The modes that rarely under cooling are localized vibrations. The participation ratio, $P(\omega) \equiv \frac{1}{Nd}(\sum_i \Psi_{\omega i}^2)^2 / \sum_i \Psi_{\omega i}^4$, quantifies the extensity of char-

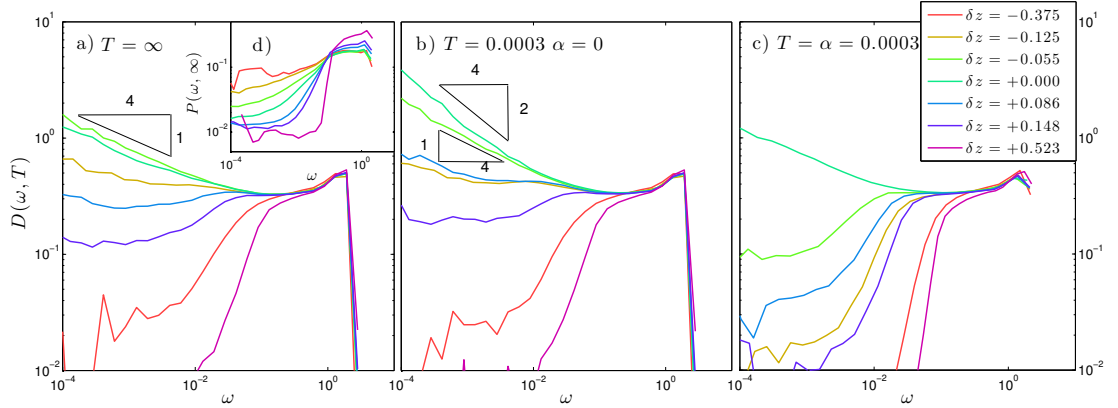


Figure C.2: Density of states $D(\omega, T)$ for adaptive networks with different z . (a) Random diluted networks $T = \infty$; a power law $D(\omega) \sim \omega^{-0.25}$ is shown in low frequency range for networks near z_{cen} . (b) Adaptive networks without weak constraints ($\alpha = 0$) at $T = 0.0003$; power laws with different exponents are shown for networks in the rigidity window: $D(\omega) \sim \omega^{-0.25}$ for $\delta z = -0.055$, $D(\omega) \sim \omega^{-0.5}$ for $\delta z = 0.0$. (c) Adaptive networks with weak constraints ($\alpha = 0.0003$) at $T \approx \alpha$; away from isostatic, density of states are gapped between zero frequency and Boson peak, where $D(\omega) \sim \omega^0$. Inset (d) Participation ratio $P(\omega, T)$ at $T = \infty$, see text for definition.

characteristic modes: $P \rightarrow 0$ corresponds to a localized mode, while $P \rightarrow 1$ means that the mode extends over the system. Both the low and high frequency ends of the density of states are reduced under cooling, but the modes in the middle are enhanced, as shown in the right panel of Fig. C.1. This agrees with the small participation ratio of modes with low and high frequencies, see Fig. C.2(d). In fact, all modes become extended – the participation ratio increases over the whole spectrum – when the temperature decreases, as shown in the inset of Fig. C.1.

In addition to localization, another prominent feature of reduced low frequency modes is the power law diverging density of states $D(\omega) \sim \omega^{\tilde{d}-1}$, see Fig. C.2. The abundance of low frequency localized modes appearing with a power

low density of states signals the “fractons” that appear near the rigidity percolation [68, 159, 224]. The exponent of the diverging tail, in Fig. C.2(a), implies the fracton dimension $\tilde{d} \approx 0.75$, which is consistent with 0.78 observed for the rigidity percolation [158, 159]. Different fracton dimensions \tilde{d} are observed for different coordination number in the case of rigidity window shown in Fig. C.2(b), although more work would be needed to establish this fact empirically.

We discuss when the temperature affects the mode with frequency ω in Section C and show illustrations of “fractons” in Section D.

C.3 Adaptation effects on density of states

When $\alpha > 0$, following Eq.(4.6), we see the typical elastic energy corresponding to a mode of frequency ω scales as $\alpha/(\omega^2 + \alpha)$, which is proportional to α for $\omega \sim 1$, while proportional to 1 when $\omega \ll \sqrt{\alpha}$. This implies that the elastic energy in the degrees of freedom corresponding to the modes of low frequency is of the same magnitude as the one in the redundant constraints. Similar to the redundant constraints, these low frequency modes are reduced under cooling.

From Eq.(4.12b), $T^*(\omega, \alpha) \sim \alpha/(\omega^2 + \alpha)$ gives an estimate on the temperature scale the mode ω begins to be reduced. The adaptation effect at this temperature scale can be seen in the right panel of Fig. C.1. For example, the green line at $T \approx 0.04 \ll 1$ shows a density of states with frequencies $\omega \lesssim \sqrt{\alpha} \approx 0.01$ strongly suppressed, while the shape of density of states with $\omega \approx 0.1$ and above is almost unchanged. The purple line, $T \approx 10^{-4} \sim \alpha$, shows a density of states whose highest frequency $\omega \sim 1$ is also significantly reduced.

C.4 Fractons

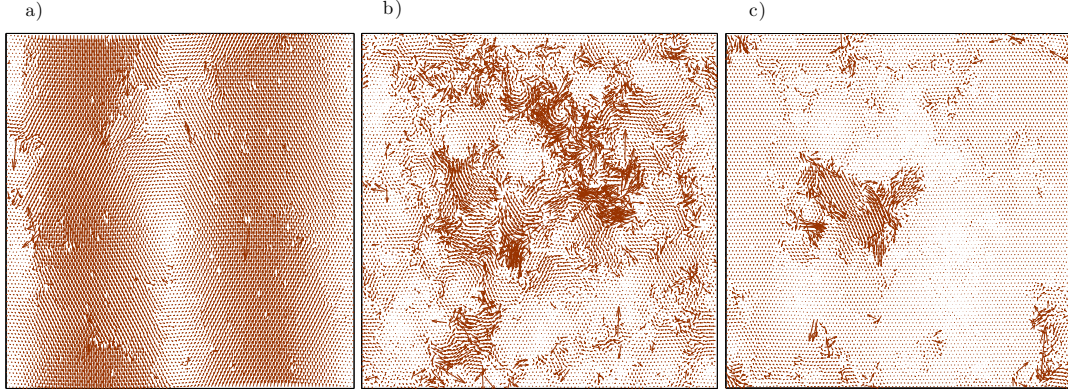


Figure C.3: Vector plots of vibrational modes in randomly diluted networks, $N = 100 \times 100$. (a) A typical Debye mode, $\delta z = 0.501$, $\omega = 0.017$. (b) A typical anomalous mode on boson peak, $\delta z = -0.049$, $\omega = 0.011$. (c) A typical fracton, $\delta z = -0.049$, $\omega = 0.0007$.

“Fractons” are different from either the low frequency Debye modes or the anomalous modes on the boson peak, as shown in Fig. C.3. They (Fig. C.3(c)) are localized and random compared to the Debye modes (Fig. C.3(a)), and concentrated on a fractal sets with sharp boundaries, unlike the extended anomalous modes (Fig. C.3(b)). The “fractons” are associated with the collective motion of large isostatic or nearly isostatic regions as shown in Fig. D.2.

C.5 Vibrational entropy contribution

The structure the elastic potential evolve with temperature in the liquid phase of the adaptive network model. Freezing into a glass phase eliminates this variability and leads to a contribution to the jump of specific heat [149]. Our model

currently ignore the vibrational part of the specific heat, which incorporates that the shape of the inherent structure evolve with temperature - not only its bottom energy. We estimate this contribution from vibrations in this subsection, and argue that it is not significant for the models we consider.

The vibrational entropy includes both linear $\omega > 0$ and floppy $\omega = 0$ vibration modes [149]:

$$s_{vib}(T) = [1 - n_r(T)] \int d\omega D(\omega, T) \ln \frac{eT}{\hbar\omega} + f(T) \ln \Lambda \quad (\text{C.5})$$

Λ sets a cutoff volume for floppy modes, which is approximately the atomic spacing measured in the Lindemann's length: $\Lambda \approx (1/0.15)^d$, of order 10^3 in 3D [180]. f is the floppy mode density, dual to the number of redundant constraints density $f(T) = -\delta z/z + n_r(T)$ and thus $\partial f(T)/\partial T = \partial n_r(T)/\partial T$. The jump of specific heat follows:

$$\begin{aligned} \Delta c_{vib} = T_g \frac{\partial n_r(T)}{\partial T} \Big|_{T_g} & \left[\ln \Lambda - \int d\omega D_{T_g}(\omega) \ln \frac{eT_g}{\hbar\omega} \right] \\ & + [1 - n_r(T_g)] \int d\omega T_g \frac{\partial D_T(\omega)}{\partial T} \Big|_{T_g} \ln \frac{eT_g}{\hbar\omega} \quad (\text{C.6}) \end{aligned}$$

The derivatives on $\ln T$ in Eq.(C.5), continuous at the glass transition, have been subtracted.

We estimate the upper limit of the vibrational contribution. ① The first term in Eq.(C.6): Debye frequency ω_D sets the upper limit of the integral in the bracket, $-\ln(eT_g/\hbar\omega_D)$. As the glass transition temperature T_g and Debye temperature $\theta_D = \hbar\omega_D/k_B$ are usually of the same order, the bracket in the first

term is dominated by $\ln \Lambda$. From Eqs.(4.11), we have $\partial n_r / \partial \ln T|_{T_g} \approx \frac{1}{2} n_{ex}(T_g) \lesssim \frac{1}{2} n_0 \sqrt{T_g} \lesssim 0.02 \sqrt{\alpha}$, and $\ln \Lambda \approx 5$ in 2D. Compared to the specific heat values, which are of order one shown in Fig. 4.7, and the scalings of the minima $-0.1 / \ln \alpha$ given in [116], the contribution, $0.1 \sqrt{\alpha}$, is insignificant if $0 < \alpha < 0.1$.

② The second term in Eq.(C.6): The upper limit of the bracket is 1. Replacing $\ln(eT/\hbar\omega)$ with its upper limit $\ln \Lambda$, we simplify the integral to $\int d\omega T \partial D / \partial T$. We can estimate the upper limit of the derivative in the integral approximately by $\Delta n_T / \Delta \ln T$, where Δn_T is the number density of the modes reduced under cooling. $\Delta n_T \approx 0.2 \int_0^{0.01} \omega^{-0.25} d\omega \approx 0.01$, roughly the number fraction of “fractons” suppressed under cooling. Together, the upper limit of the contribution of the second term is $\Delta n_T / \ln 10 \times \ln \Lambda \approx 0.03$, which is moderate compared to the values of order one.

Therefore, the vibrational entropy contributes mildly to the jump of specific heat, and does not change the qualitative behavior of Δc in our model of network glasses.

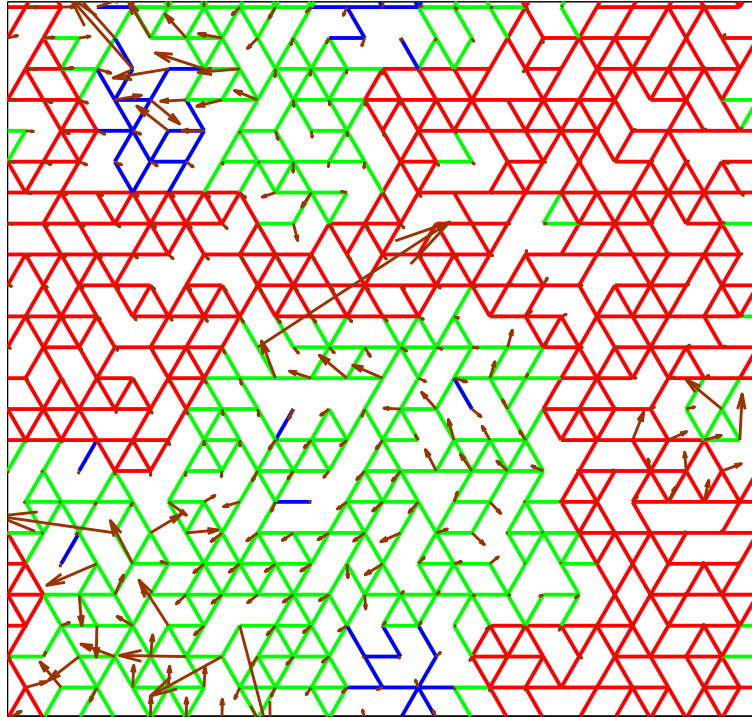


Figure C.4: Correlation between a low frequency fractal mode and isostatic clusters. A network configuration ($\delta z = -0.042$) is shown with its springs in the over-constrained regions colored in red, in the isostatic regions colored in green, and in the floppy regions colored in blue. A typical fracton ($\omega = 5 \times 10^{-4}$) specified in this configuration is plotted on top.

Appendix D

Dynamics and correlations among soft excitations in marginally stable glasses

D.1 Stability criterion

Consider flipping m spins selected from the set of the m' ($m' > m$) least stable spins. We make the approximation that the exchange energy of such multi-flip excitations is a random Gaussian variable when m is large, as supported by Fig. D.1. The mean and the variance of $\Delta\mathcal{H}$ are:

$$\mu \equiv \langle \Delta\mathcal{H} \rangle = 2m (\langle \lambda \rangle_{m'} - m \langle Jss \rangle_{m'}), \quad (\text{D.1a})$$

$$\sigma^2 \equiv \langle \Delta\mathcal{H}^2 \rangle - \langle \Delta\mathcal{H} \rangle^2 = 8m^2/N, \quad (\text{D.1b})$$

where we have neglected the contribution from the non-diagonal terms of $\langle \sum J_{ss} \sum J_{ss} \rangle$. We also omitted the fluctuations of the sum $\sum_i \lambda_i$, since that sum is anyhow always positive, and at large m its fluctuations are smaller than its expectation value. The maximal stability in the set of m' spins is

$$m' = N \int_0^{\lambda_{m'}} \rho(\lambda) d\lambda,$$

and the mean values of the local stability, $\langle \lambda \rangle_{m'}$, and the correlation $\langle J_{ss} \rangle_{m'}$ are by definition,

$$\begin{aligned} \langle \lambda \rangle_{m'} &\equiv \int_0^{\lambda_{m'}} \rho(\lambda) \lambda d\lambda / \int_0^{\lambda_{m'}} \rho(\lambda) d\lambda, \\ \langle J_{ss} \rangle_{m'} &\equiv -\frac{1}{2} \int_0^{\lambda_{m'}} d\lambda \int_0^{\lambda_{m'}} d\lambda' C(\lambda, \lambda') / \lambda_{m'}^2. \end{aligned}$$

Here $C(\lambda, \lambda')$ is the correlation between the spins at the finite local stabilities $\lambda > 0$ and $\lambda' > 0$, defined as

$$\begin{aligned} C(\lambda, \lambda') &\equiv -2 \langle J_{ij} s_i s_j \rangle |_{\lambda_i = \lambda, \lambda_j = \lambda'} \\ &\equiv \frac{1}{N^2 \rho(\lambda) \rho(\lambda')} \sum_{i,j} \delta(\lambda_i - \lambda) \delta(\lambda_j - \lambda') (-2 J_{ij} s_i s_j). \end{aligned} \quad (\text{D.2})$$

In the above $\rho(\lambda) = \sum_i \delta(\lambda_i - \lambda) / N$ is the density of stabilities.

$C(\lambda, \lambda')$ is a symmetric function, and continuous except for the singular point $\lambda = \lambda' = 0$. Defining the correlation $C(\lambda) \equiv C(\lambda, \lambda' = 0)$ between a stable ($\lambda > 0$) and a soft spin ($\lambda' = 0$), we find that it behaves as a power-law, described by Eq.(6.7) in *Chapter 6*. As far as scaling is concerned we thus expect $C(\lambda, \lambda') \sim C(\max[\lambda, \lambda'])$. In Section B we find numerically that $C(\lambda, \lambda') \approx C(\sqrt{\lambda^2 + \lambda'^2})$.

Assuming the pseudo-gap distribution of Eq.(6.4) together with Eq.(6.7)

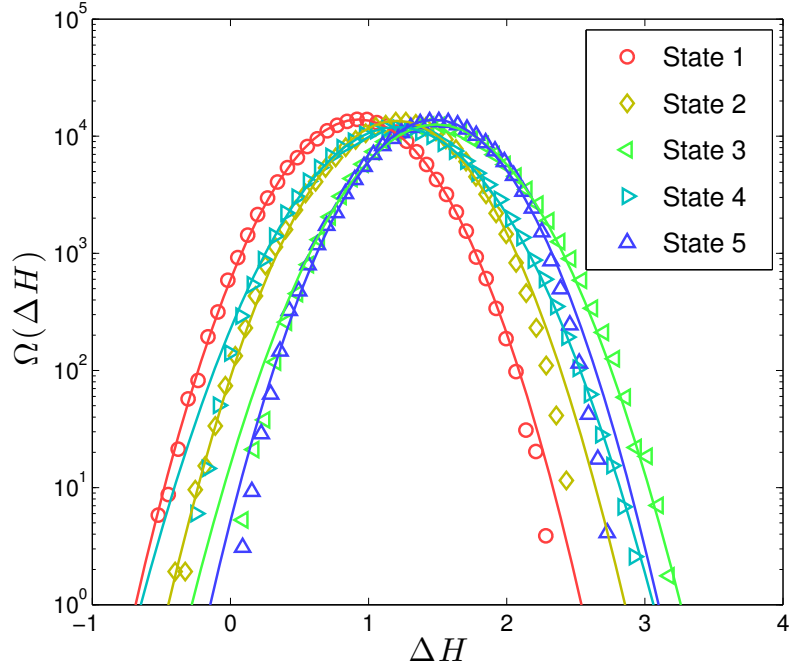


Figure D.1: Histogram of excitations with given energy change ΔH for different metastable states along the hysteresis curve, $m = 8$, $m' = 16$, and $N = 3000$.

of *Chapter 6*, one finds for $1 \ll m < m' \ll N$:

$$\mu = \frac{2m^{3/2}}{N^{1/(1+\theta)}} \left(a^{1/2} \frac{m'^{1/(1+\theta)}}{m^{1/2}} + \frac{b^{1/2}}{N^{\delta-(1+\gamma)/(1+\theta)}} \frac{m^{1/2}}{m'^{\gamma/(1+\theta)}} \right),$$

where a and b are numerical prefactors. Note that the variation of μ from states to state in Fig. D.1 is presumably a consequence of the small values of m, m' used there.

Among all excitations of m out of m' spins, the number of sets that lower the total energy, $\Delta \mathcal{H} < 0$, is

$$\Omega(m, m') = \binom{m'}{m} \Phi \left(\frac{\mu}{\sqrt{2\sigma}} \right) \approx \frac{m'!}{m!(m'-m)!} \exp \left(-\frac{\mu^2}{2\sigma^2} \right),$$

where Φ is the complementary error function.

We define a free energy as the logarithm of Ω ,

$$f(r) \equiv -\frac{1}{m} \ln \Omega \sim -r \ln r + (r-1) \ln(r-1) \quad (\text{D.3})$$

$$+ \frac{a}{4} r^{2/(1+\theta)} \left(\frac{m}{N}\right)^{\frac{1-\theta}{1+\theta}} + \frac{b}{4} r^{-2\gamma/(1+\theta)} \frac{m^{1-2\gamma/(1+\theta)}}{N^{2\delta-1-2\gamma/(1+\theta)}},$$

where $r \equiv m'/m$. The cross term ($\sim \langle \lambda \rangle_{m'} \langle Jss \rangle_{m'}$) in μ^2 has been neglected, as it cannot diverge faster than the terms in the second line of Eq. (D.3). A positive $f(r)$ implies no unstable excitations of the initial state in the limit $m \gg 1$. Stability is thus achieved if either term in the second line of Eq. (D.3) diverges as $m \rightarrow \infty$. This requires that either $\theta \geq 1$, or $\gamma \leq 1$ and $\delta \leq 1$, as explained in *Chapter 6*.

In the marginal case, $\theta = \gamma = \delta = 1$, the free energy becomes:

$$f(r) \approx -r \ln r + (r-1) \ln(r-1) + \frac{ar^2 + b + 2\sqrt{abr}}{4r}. \quad (\text{D.4})$$

An interesting finding is that $f(r)$ is minimized by a finite ratio r^* , independently of the set size m . r^* is an estimate of the optimal volume $m'^* = r^*m$ for finding energy lowering subsets of size m .

The fact that stability is controlled by the ratio r instead of the absolute values of m or m' is consistent with the observation that the dynamics proceeds via power-law avalanches with no scales (a fact implied by the argument of Ref. [101]). Indeed in the marginal case multi-flip excitations can be slightly unstable (as illustrated in Fig. D.1), and can be triggered as the magnetic field is increased. Marginality is apparent when analyzing these avalanches: We find that the energy

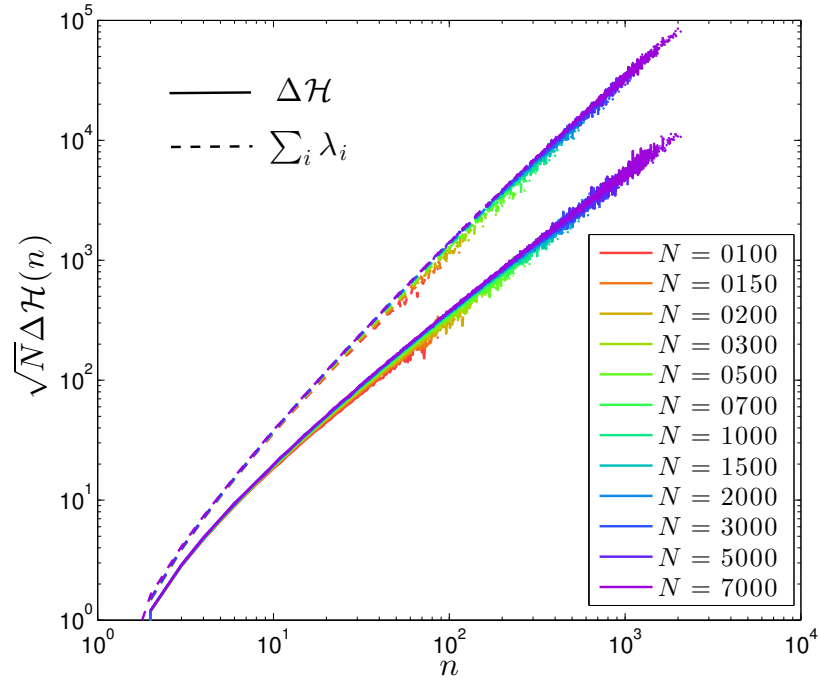


Figure D.2: The lower data set in solid lines is the total energy $\Delta\mathcal{H}(n)$ dissipated in avalanches of size n . The upper data set in dashed lines is the sum of local stabilities (before the avalanche) of spins that are going to flip in the avalanche, $\sum_{i \text{ flip}} \lambda_i$. This shows that the dissipated energy is vanishingly small as compared to the naïve sum over local stabilities, as $n \rightarrow \infty$, since the two curves scale as different power laws with n .

dissipated in avalanches is much smaller than the naïve estimate which sums all local stabilities of spins that are going to flip in the avalanche, $\sum_{i \text{ flip}} \lambda_i$. This reflects the fact that the total energy change in the avalanche, $\Delta\mathcal{H}$, is a result of a near cancellation of several terms, as discussed in *Chapter 6*, verified in Fig. D.2.

D.2 Two-point correlation

We numerically measured the two-point correlation, and found $NC(\lambda, \lambda') = D/\sqrt{[\lambda + c(N)]^2 + [\lambda' + c(N)]^2}$ as long as $\lambda, \lambda' \ll 1$. Here, $c(N) = 1.1\sqrt{\ln N/N}$ is a finite size correction which vanishes in the thermodynamic limit. This result is illustrated in Fig. D.3. When finite size effects are negligible this implies that $C(\lambda, \lambda') \approx C(\sqrt{\lambda^2 + \lambda'^2})$.

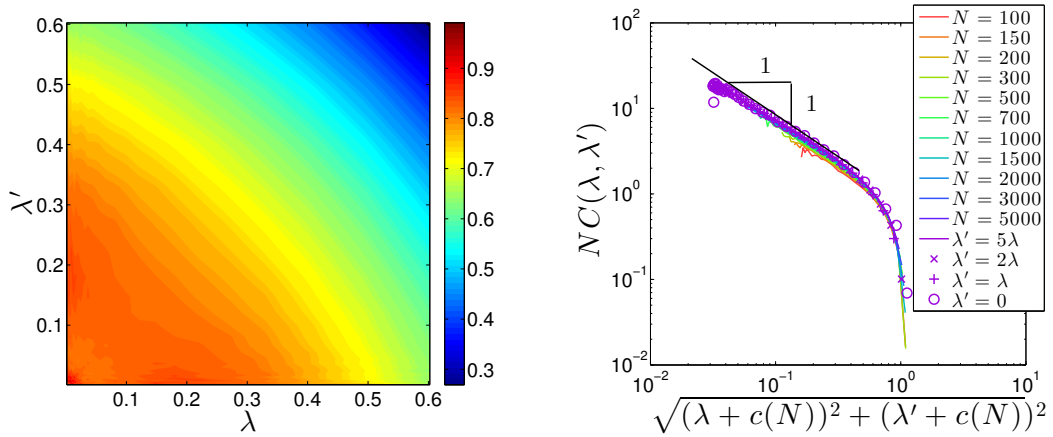


Figure D.3: Left: the quantity $NC(\lambda, \lambda')\sqrt{(\lambda + c(N))^2 + (\lambda' + c(N))^2}$ is numerically computed for various λ and λ' , and behaves nearly as a constant (as the color code indicates, this quantity only changes by a factor 3 in the entire range considered). Right: Correlation $C(\lambda, \lambda')$, for $\lambda' = 5\lambda$ with different system sizes N and for different directions $\lambda' = a\lambda$, $a = 0, 1, 2, 5$ with $N = 5000$.

D.3 Dynamical Constraints on θ

In *Chapter 6*, we argue that the density of local stabilities $\rho(\lambda)$ satisfies a Fokker-Planck (FP) equation of the type:

$$\partial_t \rho(\lambda, t) = -\partial_\lambda [v(\lambda, t) - \partial_\lambda D(\lambda, t)] \rho(\lambda, t), \quad (\text{D.5})$$

with a reflecting boundary at $\lambda = 0$. In addition, we show that correlations emerge dynamically, which in the steady state take the form:

$$C(\lambda)N = v_{\text{ss}}(\lambda) = D\partial_\lambda \rho_{\text{ss}}(\lambda)/\rho_{\text{ss}}(\lambda). \quad (\text{D.6})$$

These results seem to imply that the fact that correlations are necessary to obtain a steady state, is not constraining the latter in any way. Indeed, any function $\rho_{\text{ss}}(\lambda)$ could in principle appear as a steady state, as long as the correlations satisfy Eq. (D.6). This is true in particular for any scaling function $\rho_{\text{ss}}(\lambda) \sim \lambda^\theta$, whatever the value of θ . However, we now argue that only the case $\theta = 1$ is a viable solution in SK model.

Excluding $\theta < 1$: Our FP description only applies beyond the discretization scale of the kicks due to flipping spins, which are of order $J \sim 1/\sqrt{N}$. In particular, from its definition, $C(\lambda)$ must be bounded by $1/\sqrt{N}$. Taking this into account, Eq. (D.6) should be modified to:

$$v_{\text{ss}}(\lambda) \approx \min\{D\partial_\lambda \rho_{\text{ss}}(\lambda)/\rho_{\text{ss}}(\lambda) \sim 1/\lambda, \sqrt{N}\}. \quad (\text{D.7})$$

This modification has no effect when $\theta \geq 1$, since in that case $\lambda_{\min} \sim N^{-1/(1+\theta)} \geq 1/\sqrt{N}$. In contrast, pseudo-gaps with $\theta < 1$ have $\lambda_{\min} \ll 1/\sqrt{N}$. To maintain such a pseudo-gap in a stationary state, one would require correlations much larger than what the discreteness of the model allows. Pseudo-gaps with $\theta < 1$ are thus not admissible solutions of Eqs. (D.5, D.7).

Excluding $\theta > 1$: In this case, $\lambda_{\min} \gg 1/\sqrt{N} \sim J$. Thus when one spin flips, the second least stable spin will not flip in general, and avalanches are typically of size unity [101]. It can easily be shown that in that case, our assumption (ii) in *Chapter 6* is violated: the number of flips per spin along the loop would be small (in fact it would even vanish in the thermodynamic limit, which is clearly impossible). In terms of our FP description, the motion of the spin stabilities due to other flips would be small in comparison with the motion of the stabilities inbetween avalanches, due to changes of the magnetic field. Making the crude assumption that the magnetization is random for any λ , the change of external magnetic field leads to an additional diffusion term in the Fokker-Planck equation:

$$\partial_t \rho(\lambda, t) = -\partial_\lambda (v - D\partial_\lambda) \rho(\lambda, t) + D_h \partial_\lambda^2 \rho(\lambda, t), \quad (\text{D.8})$$

where the term D_h is related to the typical field increment $h_{\min} \sim \lambda_{\min}$ required to trigger an avalanche. Indeed $D_h \sim N h_{\min}^2 \sim N^{(\theta-1)/(\theta+1)} \gg D \sim 1$. Under these circumstances, Eq. (D.6) does not hold. The dynamics would be a simple diffusion with reflecting boundary, whose only stationary solution corresponds to $\theta = 0$, violating our hypothesis $\theta > 1$.

D.4 Analogy to a d dimensional random walk

Consider a non-biased random walk in d dimension,

$$\vec{x}(t + dt) = \vec{x}(t) + \sqrt{2Ddt}\vec{\eta}(t), \quad (\text{D.9})$$

where D is the diffusion constant, and $\vec{\eta}$ is a random Gaussian vector. Then the probability density $P(\vec{x}, t)$ satisfies the Fokker-Planck equation [225],

$$\partial_t P(\vec{x}, t) = D\nabla^2 P(\vec{x}, t).$$

The process is angle-independent, so $P(\vec{x}, t)$ satisfies,

$$\partial_t P(r, t) = D\partial_r^2 P(r, t) + D\frac{d-1}{r}\partial_r P(r, t), \quad (\text{D.10})$$

where $r = |\vec{x}|$. However, $P(r, t)$ is not a probability density with respect to r . Including the Jacobian of the change of variables, the probability density, $\rho(r, t) \equiv \Omega_d r^{d-1} P(r, t)$, satisfies the corresponding Fokker-Planck equation,

$$\partial_t \rho(r, t) = -\partial_r \left(D\frac{d-1}{r} - D\partial_r \right) \rho(r, t), \quad (\text{D.11})$$

with Ω_d the solid angle in d dimensions. This Fokker-Planck equation for the radial component of a d -dimensional unbiased random walk is exactly the same as the diffusion equation, Eq.(6.10), with reflecting boundary at $\lambda = 0$ and diverging drift $v(\lambda) = \theta/\lambda$ at small λ . The case of pseudo-gap exponent $\theta = 1$ in the spin model thus maps to a two-dimensional random walk.

Bibliography

- [1] M. D. Ediger, C. A. Angell, and S. R. Nagel. “Supercooled liquids and glasses”. In: *J. Phys. Chem.* 100 (1996), p. 13200.
- [2] Pablo G. Debenedetti and Frank H. Stillinger. “Supercooled liquids and the glass transition”. In: *Nature* 410.6825 (Mar. 2001), pp. 259–267. URL: <http://dx.doi.org/10.1038/35065704>.
- [3] Ronald Walter Douglas and Susan Frank. *A history of glass making*. GT Foulis & co., 1972.
- [4] Roland Böhmer and C. Austen Angell. “Correlations of the nonexponentiality and state dependence of mechanical relaxations with bond connectivity in Ge-As-Se supercooled liquids”. In: *Phys. Rev. B* 45 (17 1992), pp. 10091–10094. DOI: 10.1103/PhysRevB.45.10091. URL: <http://link.aps.org/doi/10.1103/PhysRevB.45.10091>.
- [5] Li-Min Wang, C. Austen Angell, and Ranko Richert. “Fragility and thermodynamics in nonpolymeric glass-forming liquids”. In: *The Journal of Chemical Physics* 125.7, 074505 (2006), pp. –. DOI: <http://dx.doi.org/10.1063/1.2244551>. URL: <http://scitation.aip.org/content/aip/journal/jcp/125/7/10.1063/1.2244551>.

- [6] R. A. Bagnold. *The Physics of Sediment Transport by Wind and Water: A Collection of Hallmark Papers by RA Bagnold*. 231. 1966.
- [7] Gary Parker et al. “Physical basis for quasi-universal relations describing bankfull hydraulic geometry of single-thread gravel bed rivers”. In: *Journal of Geophysical Research: Earth Surface* 112.F4 (2007), n/a–n/a. ISSN: 2156-2202. DOI: 10.1029/2006JF000549. URL: <http://dx.doi.org/10.1029/2006JF000549>.
- [8] Per Bak. *How nature works: the science of self-organized criticality*. Springer Science & Business Media, 2013.
- [9] Olga Perkovi ć, Karin Dahmen, and James P. Sethna. “Avalanches, Barkhausen Noise, and Plain Old Criticality”. In: *Phys. Rev. Lett.* 75 (24 1995), pp. 4528–4531. DOI: 10.1103/PhysRevLett.75.4528. URL: <http://link.aps.org/doi/10.1103/PhysRevLett.75.4528>.
- [10] Stefano Zapperi et al. “Dynamics of a ferromagnetic domain wall: Avalanches, depinning transition, and the Barkhausen effect”. In: *Physical Review B* 58.10 (1998), p. 6353.
- [11] P. Le Doussal, M. Müller, and K. J. Wiese. “Avalanches in mean-field models and the Barkhausen noise in spin-glasses”. In: *EPL (Europhysics Letters)* 91.5 (2010), p. 57004. URL: <http://stacks.iop.org/0295-5075/91/i=5/a=57004>.
- [12] P. M. Chaikin and T. C. Lubensky. *Principles of Condensed Matter Physics*. Cambridge, U.K.: Cambridge University Press, Oct. 2000. ISBN: 9780521794503.
- [13] John Cardy. *Scaling and renormalization in statistical physics*. Vol. 5. Cambridge university press, 1996.

- [14] P. C. Hohenberg and B. I. Halperin. “Theory of dynamic critical phenomena”. In: *Rev. Mod. Phys.* 49 (3 1977), pp. 435–479. DOI: 10.1103/RevModPhys.49.435. URL: <http://link.aps.org/doi/10.1103/RevModPhys.49.435>.
- [15] E. Leutheusser. “Dynamical model of the liquid-glass transition”. In: *Phys. Rev. A* 29 (5 1984), pp. 2765–2773. DOI: 10.1103/PhysRevA.29.2765. URL: <http://link.aps.org/doi/10.1103/PhysRevA.29.2765>.
- [16] Jean-Philippe Bouchaud et al. “Mode-coupling approximations, glass theory and disordered systems”. In: *Physica A: Statistical Mechanics and its Applications* 226.3 (1996), pp. 243–273.
- [17] G. Biroli and J. P. Bouchaud. In: *Europhys. Lett.* 67 (2004), pp. 21–27.
- [18] Giulio Biroli et al. “Inhomogeneous Mode-Coupling Theory and Growing Dynamic Length in Supercooled Liquids”. In: *Phys. Rev. Lett.* 97 (2006), p. 195701.
- [19] C. Dalle-Ferrier et al. “Spatial correlations in the dynamics of glassforming liquids: Experimental determination of their temperature dependence”. In: *Phys. Rev. E* 76 (2007), p. 041510.
- [20] Sharon C Glotzer. “Spatially heterogeneous dynamics in liquids: insights from simulation”. In: *Journal of Non-Crystalline Solids* 274.1 (2000), pp. 342–355.
- [21] Jean-Philippe Bouchaud and Giulio Biroli. “On the Adam-Gibbs-Kirkpatrick-Thirumalai-Wolynes scenario for the viscosity increase in glasses”. In: *The Journal of Chemical Physics* 121.15 (2004), pp. 7347–7354. DOI: [http :](http://)

[//dx.doi.org/10.1063/1.1796231](http://dx.doi.org/10.1063/1.1796231). URL: <http://scitation.aip.org/content/aip/journal/jcp/121/15/10.1063/1.1796231>.

- [22] L. Berthier et al. “Direct Experimental Evidence of a Growing Length Scale Accompanying the Glass Transition”. In: *Science* 310.5755 (2005), pp. 1797–1800. DOI: 10.1126/science.1120714. eprint: <http://www.sciencemag.org/content/310/5755/1797.full.pdf>.
- [23] Jorge Kurchan and Dov Levine. “Correlation length for amorphous systems”. In: *arXiv preprint arXiv:0904.4850* (2009).
- [24] H. Vogel. “Das temperature-abhängigketsygesetz der viskosität von flüssigkeiten”. In: *Phys. Z.* 22 (1921), p. 645646.
- [25] Gordon S Fulcher. “Analysis of recent measurements of the viscosity of glasses”. In: *Journal of the American Ceramic Society* 8.6 (1925), pp. 339–355.
- [26] G. Tammann and W. Hesse. “Die Abhängigkeit der Viskosität von der Temperatur bei unterkühlten Flüssigkeiten”. In: *Z. Anorg. Allg. Chem.* 156 (1926), pp. 245–257.
- [27] L.-M. Martinez and C. A. Angell. “A thermodynamic connection to the fragility of glass-forming liquids”. In: *Nature* 410 (6829 2001), pp. 663–667. DOI: <http://dx.doi.org/10.1038/35070517>.
- [28] T. R. Kirkpatrick, D. Thirumalai, and P. G. Wolynes. “Scaling concepts for the dynamics of viscous liquids near an ideal glassy state”. In: *Phys. Rev. A* 40 (2 1989), pp. 1045–1054. DOI: 10.1103/PhysRevA.40.1045. URL: <http://link.aps.org/doi/10.1103/PhysRevA.40.1045>.

- [29] Vassiliy Lubchenko and Peter G. Wolynes. “Theory of Structural Glasses and Supercooled Liquids”. In: *Annual Review of Physical Chemistry* 58.1 (2007), pp. 235–266. DOI: 10.1146/annurev.physchem.58.032806.104653.
- [30] Giulio Biroli and Jean-Philippe Bouchaud. “The random first-order transition theory of glasses: a critical assessment”. In: *Structural Glasses and Supercooled Liquids: Theory, Experiment, and Applications* (2012), pp. 31–113.
- [31] Randall W. Hall and Peter G. Wolynes. “Microscopic Theory of Network Glasses”. In: *Phys. Rev. Lett.* 90 (8 2003), p. 085505. DOI: 10.1103/PhysRevLett.90.085505. URL: <http://link.aps.org/doi/10.1103/PhysRevLett.90.085505>.
- [32] Dmytro Bevzenko and Vassiliy Lubchenko. “Stress distribution and the fragility of supercooled melts”. In: *The Journal of Physical Chemistry B* 113.51 (2009), pp. 16337–16345.
- [33] KL Ngai, A Sokolov, and W Steffen. “Correlations between boson peak strength and characteristics of local segmental relaxation in polymers”. In: *Journal of Chemical Physics* 107.13 (1997), pp. 5268–5272.
- [34] V. N. Novikov, Y. Ding, and A. P. Sokolov. “Correlation of fragility of supercooled liquids with elastic properties of glasses”. In: *Phys. Rev. E* 71 (2005), p. 061501.
- [35] M. Tatsumisago et al. “Fragility of Ge-As-Se glass-forming liquids in relation to rigidity percolation, and the Kauzmann paradox”. In: *Phys. Rev. Lett.*

- 64 (13 1990), pp. 1549–1552. DOI: 10.1103/PhysRevLett.64.1549. URL: <http://link.aps.org/doi/10.1103/PhysRevLett.64.1549>.
- [36] R Ota et al. “Elastic properties of Ge-Se glass under pressure”. In: *Journal of Non-Crystalline Solids* 29.1 (1978), pp. 67–76.
- [37] Sudha Mahadevan, A Giridhar, and AK Singh. “Elastic properties of Ge-Sb-Se glasses”. In: *Journal of non-crystalline solids* 57.3 (1983), pp. 423–430.
- [38] A.N. Sreeram, A.K. Varshneya, and D.R. Swiler. “Molar volume and elastic properties of multicomponent chalcogenide glasses”. In: *Journal of Non-Crystalline Solids* 128.3 (1991), pp. 294 –309. ISSN: 0022-3093. DOI: [http://dx.doi.org/10.1016/0022-3093\(91\)90467-K](http://dx.doi.org/10.1016/0022-3093(91)90467-K). URL: <http://www.sciencedirect.com/science/article/pii/002230939190467K>.
- [39] J.C. Maxwell. “On the calculation of the equilibrium and stiffness of frames”. In: *Philos. Mag.* 27.5755 (1864), pp. 294–299.
- [40] J.C. Phillips. “Topology of covalent non-crystalline solids I: Short-range order in chalcogenide alloys”. In: *Journal of Non-Crystalline Solids* 34.2 (1979), pp. 153 –181. ISSN: 0022-3093. DOI: [http://dx.doi.org/10.1016/0022-3093\(79\)90033-4](http://dx.doi.org/10.1016/0022-3093(79)90033-4). URL: <http://www.sciencedirect.com/science/article/pii/0022309379900334>.
- [41] J. C. Phillips and M. F. Thorpe. “Constraint theory, vector percolation and glass-formation”. In: *Sol. State Comm.* 53 (1985), pp. 699–702.
- [42] D Selvanathan et al. “Thermally reversing window and stiffness transitions in chalcogenide glasses”. In: *Solid State Communications* 111.11 (1999), pp. 619 –624. ISSN: 0038-1098. DOI: <http://dx.doi.org/10.1016/S0038->

- 1098(99)00248-3. URL: <http://www.sciencedirect.com/science/article/pii/S0038109899002483>.
- [43] D. G. Georgiev, P. Boolchand, and M. Micoulaut. “Rigidity transitions and molecular structure of $\text{As}_x\text{Se}_{1-x}$ glasses”. In: *Phys. Rev. B* 62 (14 2000), R9228–R9231. DOI: 10.1103/PhysRevB.62.R9228. URL: <http://link.aps.org/doi/10.1103/PhysRevB.62.R9228>.
- [44] Y. Wang, P. Boolchand, and M. Micoulaut. “Glass structure, rigidity transitions and the intermediate phase in the Ge-As-Se ternary”. In: *EPL (Europhysics Letters)* 52.6 (2000), p. 633. URL: <http://stacks.iop.org/0295-5075/52/i=6/a=633>.
- [45] S Chakravarty et al. “Ageing, fragility and the reversibility window in bulk alloy glasses”. In: *Journal of Physics: Condensed Matter* 17.1 (2005), p. L1. URL: <http://stacks.iop.org/0953-8984/17/i=1/a=L01>.
- [46] Fei Wang et al. “Pressure Raman effects and internal stress in network glasses”. In: *Phys. Rev. B* 71 (17 2005), p. 174201. DOI: 10.1103/PhysRevB.71.174201. URL: <http://link.aps.org/doi/10.1103/PhysRevB.71.174201>.
- [47] Ping Chen et al. “Intermediate phase, network demixing, boson and floppy modes, and compositional trends in glass transition temperatures of binary $\text{As}_x\text{S}_{1-x}$ system”. In: *Phys. Rev. B* 78 (22 2008), p. 224208. DOI: 10.1103/PhysRevB.78.224208. URL: <http://link.aps.org/doi/10.1103/PhysRevB.78.224208>.
- [48] S. Bhosle et al. “Melt Homogenization and Self-Organization in Chalcogenides - Part II”. In: *International Journal of Applied Glass Science* 3.3

- (2012), pp. 205–220. ISSN: 2041-1294. DOI: 10.1111/j.2041-1294.2012.00092.x. URL: <http://dx.doi.org/10.1111/j.2041-1294.2012.00092.x>.
- [49] S. Bhosle et al. “Melt Homogenization and Self-Organization in Chalcogenides - Part I”. In: *International Journal of Applied Glass Science* 3.3 (2012), pp. 189–204. ISSN: 2041-1294. DOI: 10.1111/j.2041-1294.2012.00093.x. URL: <http://dx.doi.org/10.1111/j.2041-1294.2012.00093.x>.
- [50] Kostya O Trachenko et al. “Dynamics of silica glass: two-level tunnelling states and low-energy floppy modes”. In: *Journal of Physics: Condensed Matter* 12.37 (2000), p. 8041.
- [51] Corey S. O’Hern et al. “Jamming at zero temperature and zero applied stress: The epitome of disorder”. In: *Phys. Rev. E* 68.1 (2003), pp. 011306–011324. DOI: 10.1103/PhysRevE.68.011306.
- [52] Ke Chen et al. “Low-frequency vibrations of soft colloidal glasses”. In: *Physical review letters* 105.2 (2010), p. 025501.
- [53] Antina Ghosh et al. “Density of states of colloidal glasses”. In: *Physical review letters* 104.24 (2010), p. 248305.
- [54] Matthieu Wyart et al. “Effects of compression on the vibrational modes of marginally jammed solids”. In: *Physical Review E* 72.5 (2005), p. 051306.
- [55] Carolina Brito and Matthieu Wyart. “Geometric interpretation of previtrification in hard sphere liquids”. In: *The Journal of Chemical Physics* 131.2, 024504 (2009), pp. 024504–024518. DOI: 10.1063/1.3157261.

- [56] Eric DeGiuli et al. “Force distribution affects vibrational properties in hard-sphere glasses”. In: *Proceedings of the National Academy of Sciences* 111.48 (2014), pp. 17054–17059.
- [57] E DeGiuli, E Lerner, and M Wyart. “Theory of the jamming transition at finite temperature”. In: *The Journal of chemical physics* 142.16 (2015), p. 164503.
- [58] S. Franz et al. “Universal Spectrum of Normal Modes in Low-Temperature Glasses: an Exact Solution”. In: *ArXiv e-prints* (2015). arXiv:1506.01997 [cond-mat.dis-nn].
- [59] A. J. Liu and S. R. Nagel. “Nonlinear dynamics: Jamming is not just cool any more”. In: *Nature* 396 (1998), pp. 21–22.
- [60] Andrea J. Liu et al. “The jamming scenario: an introduction and outlook”. In: *Dynamical heterogeneities in glasses, colloids, and granular media*. Ed. by L. Berthier et al. Oxford: Oxford University Press, 2010.
- [61] Andrea J. Liu and Sidney R. Nagel. “The Jamming Transition and the Marginally Jammed Solid”. In: *Annual Review of Condensed Matter Physics* 1.1 (2010), pp. 347–369. DOI: 10.1146/annurev-conmatphys-070909-104045.
- [62] G. Laman. “On graphs and rigidity of plane skeletal structures”. English. In: *Journal of Engineering Mathematics* 4.4 (1970), pp. 331–340. ISSN: 0022-0833. DOI: 10.1007/BF01534980. URL: <http://dx.doi.org/10.1007/BF01534980>.

- [63] D. J. Jacobs and M. F. Thorpe. “Generic Rigidity Percolation: The Pebble Game”. In: *Phys. Rev. Lett.* 75 (22 1995), pp. 4051–4054. DOI: 10.1103/PhysRevLett.75.4051. URL: <http://link.aps.org/doi/10.1103/PhysRevLett.75.4051>.
- [64] C.R. Calladine. “Buckminster Fuller’s “Tensegrity” structures and Clerk Maxwell’s rules for the construction of stiff frames”. In: *International Journal of Solids and Structures* 14.2 (1978), pp. 161–172. ISSN: 0020-7683. DOI: 10.1016/0020-7683(78)90052-5. URL: <http://www.sciencedirect.com/science/article/pii/0020768378900525>.
- [65] JF Lutsko. “Generalized expressions for the calculation of elastic constants by computer simulation”. In: *Journal of applied physics* 65.8 (1989), pp. 2991–2997.
- [66] Smarajit Karmakar, Edan Lerner, and Itamar Procaccia. “Athermal non-linear elastic constants of amorphous solids”. In: *Physical Review E* 82.2 (2010), p. 026105.
- [67] David C. Lay. *Linear Algebra and its Applications*. 4th. Addison-Wesley, 2011.
- [68] Shechao Feng and Pabitra N. Sen. “Percolation on Elastic Networks: New Exponent and Threshold”. In: *Phys. Rev. Lett.* 52 (3 1984), pp. 216–219. DOI: 10.1103/PhysRevLett.52.216. URL: <http://link.aps.org/doi/10.1103/PhysRevLett.52.216>.
- [69] Shechao Feng, M. F. Thorpe, and E. Garboczi. “Effective-medium theory of percolation on central-force elastic networks”. In: *Phys. Rev. B* 31 (1 1985),

- pp. 276–280. DOI: 10.1103/PhysRevB.31.276. URL: <http://link.aps.org/doi/10.1103/PhysRevB.31.276>.
- [70] E. J. Garboczi and M. F. Thorpe. “Effective-medium theory of percolation on central-force elastic networks .2. further results”. In: *Phys. Rev. B* 31 (1985), p. 7276.
- [71] Sepehr Arbabi and Muhammad Sahimi. “Mechanics of disordered solids. I. Percolation on elastic networks with central forces”. In: *Phys. Rev. B* 47 (2 1993), pp. 695–702. DOI: 10.1103/PhysRevB.47.695. URL: <http://link.aps.org/doi/10.1103/PhysRevB.47.695>.
- [72] C. Moukarzel and P. M. Duxbury. “Stressed Backbone and Elasticity of Random Central-Force Systems”. In: *Phys. Rev. Lett.* 75 (22 1995), pp. 4055–4058. DOI: 10.1103/PhysRevLett.75.4055. URL: <http://link.aps.org/doi/10.1103/PhysRevLett.75.4055>.
- [73] M.F Thorpe et al. “Self-organization in network glasses”. In: *Journal of Non-Crystalline Solids* 266-269, Part 2.0 (2000), pp. 859 –866. ISSN: 0022-3093. DOI: [http://dx.doi.org/10.1016/S0022-3093\(99\)00856-X](http://dx.doi.org/10.1016/S0022-3093(99)00856-X). URL: <http://www.sciencedirect.com/science/article/pii/S002230939900856X>.
- [74] M.F. Thorpe et al. “Non-Randomness in Network Glasses and Rigidity”. English. In: *Glass Physics and Chemistry* 27.2 (2001), pp. 160–166. ISSN: 1087-6596. DOI: 10.1023/A:1011336511583. URL: <http://dx.doi.org/10.1023/A%3A1011336511583>.
- [75] M. V. Chubynsky, M.-A. Brière, and Normand Mousseau. “Self-organization with equilibration: A model for the intermediate phase in rigidity percola-

- tion”. In: *Phys. Rev. E* 74 (1 2006), p. 016116. DOI: 10.1103/PhysRevE.74.016116. URL: <http://link.aps.org/doi/10.1103/PhysRevE.74.016116>.
- [76] M. F. Thorpe and M. V. Chubynsky. *Rigidity and self-organization of network glasses and the intermediate phase*. Ed. by M. F. Thorpe and P. M. Duxbury. Vol. Properties and Applications of Amorphous Materials. NATO Science Series. Plenum/Kluwer, 2001, pp. 61–96.
- [77] P. Boolchand et al. “Self-organization and the physics of glassy networks”. In: *Philosophical Magazine* 85.32 (2005), pp. 3823–3838. DOI: 10.1080/14786430500256425.
- [78] Gustavo Düring, Edan Lerner, and Matthieu Wyart. “Phonon gap and localization lengths in floppy materials”. In: *Soft Matter* 9.1 (2013), pp. 146–154.
- [79] David Leighton and Andreas Acrivos. “Viscous resuspension”. In: *Chemical Engineering Science* 41.6 (1986), pp. 1377–1384. ISSN: 0009-2509. DOI: [http://dx.doi.org/10.1016/0009-2509\(86\)85225-3](http://dx.doi.org/10.1016/0009-2509(86)85225-3). URL: <http://www.sciencedirect.com/science/article/pii/0009250986852253>.
- [80] David Leighton and Andreas Acrivos. “The shear-induced migration of particles in concentrated suspensions”. In: *Journal of Fluid Mechanics* 181 (1987), pp. 415–439.
- [81] Malika Ouriemi, Pascale Aussillous, and Élisabeth Guazzelli. “Sediment dynamics. Part 1. Bed-load transport by laminar shearing flows”. In: *Journal of Fluid Mechanics* 636 (Oct. 2009), pp. 295–319. ISSN: 1469-7645. DOI: 10.1017/S0022112009007915. URL: http://journals.cambridge.org/article_S0022112009007915.

- [82] Pascale Aussillous et al. “Investigation of the mobile granular layer in bedload transport by laminar shearing flows”. In: *Journal of Fluid Mechanics* 736 (Dec. 2013), pp. 594–615. ISSN: 1469-7645. DOI: 10.1017/jfm.2013.546. URL: http://journals.cambridge.org/article_S0022112013005466.
- [83] Haizhen Zou, Pascale Aussillous, and Elisabeth Guazzelli. personal communication. 2015.
- [84] A. Shields. “Anwendung der Aehnlichkeitsmechanik und der Turbulenzforschung auf die Geschiebebewegung”. In: *Mitt. Preuss. Vers. Anst. Wasserb. u. Schiffb., Berlin, Heft* (1936), p. 26.
- [85] S. J. White. “Plane Bed Thresholds of Fine Grained Sediments”. In: *Nature* 228.5267 (Oct. 1970), pp. 152–153. URL: <http://dx.doi.org/10.1038/228152a0>.
- [86] F. Charru, H. Mouilleron, and O. Eiff. “Erosion and deposition of particles on a bed sheared by a viscous flow”. In: *Journal of Fluid Mechanics* 519 (Nov. 2004), pp. 55–80. ISSN: 1469-7645. DOI: 10.1017/S0022112004001028.
- [87] Alexander E. Lobkovsky et al. “Erosion of a granular bed driven by laminar fluid flow”. In: *Journal of Fluid Mechanics* 605 (June 2008), pp. 47–58. ISSN: 1469-7645. DOI: 10.1017/S0022112008001389. URL: http://journals.cambridge.org/article_S0022112008001389.
- [88] Morgane Houssais et al. “Onset of sediment transport is a continuous transition driven by fluid shear and granular creep”. In: *Nat Commun* 6 (Mar. 2015). URL: <http://dx.doi.org/10.1038/ncomms7527>.

- [89] E Lajeunesse, L Malverti, and F Charru. “Bed load transport in turbulent flow at the grain scale: Experiments and modeling”. In: *Journal of Geophysical Research: Earth Surface (2003–2012)* 115.F4 (2010).
- [90] Orencio Durán, Bruno Andreotti, and Philippe Claudin. “Turbulent and viscous sediment transport—a numerical study”. In: *Advances in Geosciences* 37.37 (2014), pp. 73–80.
- [91] Abram H Clark et al. “Onset and cessation of motion in hydrodynamically sheared granular beds”. In: *arXiv preprint arXiv:1504.03403* (2015).
- [92] Filippo Chiodi, Philippe Claudin, and Bruno Andreotti. “A two-phase flow model of sediment transport: transition from bedload to suspended load”. In: *Journal of Fluid Mechanics* 755 (2014), pp. 561–581.
- [93] A. E. Scheidegger. “A STOCHASTIC MODEL FOR DRAINAGE PATTERNS INTO AN INTRAMONTANE TRENCH”. In: *International Association of Scientific Hydrology. Bulletin* 12.1 (1967), pp. 15–20. DOI: 10.1080/02626666709493507. URL: <http://dx.doi.org/10.1080/02626666709493507>.
- [94] Hideki Takayasu, Ikuko Nishikawa, and Hal Tasaki. “Power-law mass distribution of aggregation systems with injection”. In: *Phys. Rev. A* 37 (8 1988), pp. 3110–3117. DOI: 10.1103/PhysRevA.37.3110. URL: <http://link.aps.org/doi/10.1103/PhysRevA.37.3110>.
- [95] Deepak Dhar. “Theoretical studies of self-organized criticality”. In: *Physica A: Statistical Mechanics and its Applications* 369.1 (2006), pp. 29–70.
- [96] Andrea Rinaldo et al. “Evolution and selection of river networks: Statics, dynamics, and complexity”. In: *Proceedings of the National Academy of*

- Sciences* 111.7 (2014), pp. 2417–2424. DOI: 10.1073/pnas.1322700111.
URL: <http://www.pnas.org/content/111/7/2417.abstract>.
- [97] Joe Watson and Daniel S. Fisher. “Collective particle flow through random media”. In: *Phys. Rev. B* 54 (2 1996), pp. 938–954. DOI: 10.1103/PhysRevB.54.938. URL: <http://link.aps.org/doi/10.1103/PhysRevB.54.938>.
- [98] Joe Watson and Daniel S. Fisher. “Dynamic critical phenomena in channel flow of driven particles in random media”. In: *Phys. Rev. B* 55 (22 1997), pp. 14909–14924. DOI: 10.1103/PhysRevB.55.14909. URL: <http://link.aps.org/doi/10.1103/PhysRevB.55.14909>.
- [99] Per Bak, Chao Tang, and Kurt Wiesenfeld. “Self-organized criticality: An explanation of the $1/f$ noise”. In: *Phys. Rev. Lett.* 59 (4 1987), pp. 381–384. DOI: 10.1103/PhysRevLett.59.381. URL: <http://link.aps.org/doi/10.1103/PhysRevLett.59.381>.
- [100] Maya Paczuski, Sergei Maslov, and Per Bak. “Avalanche dynamics in evolution, growth, and depinning models”. In: *Phys. Rev. E* 53 (1 1996), pp. 414–443. DOI: 10.1103/PhysRevE.53.414. URL: <http://link.aps.org/doi/10.1103/PhysRevE.53.414>.
- [101] Markus Müller and Matthieu Wyart. “Marginal Stability in Structural, Spin, and Electron Glasses”. In: *Annual Review of Condensed Matter Physics* 6.1 (2015), pp. 177–200. DOI: 10.1146/annurev-conmatphys-031214-014614.
- [102] A L Efros and B I Shklovskii. “Coulomb gap and low temperature conductivity of disordered systems”. In: *Journal of Physics C: Solid State Physics*

- 8.4 (1975), p. L49. URL: <http://stacks.iop.org/0022-3719/8/i=4/a=003>.
- [103] M. Pollak, M. Ortuno, and A. Frydman. *The Electron Glass*. Cambridge University Press, 2013.
- [104] Ferenc Pázmándi, Gergely Zaránd, and Gergely T. Zimányi. “Self-Organized Criticality in the Hysteresis of the Sherrington-Kirkpatrick Model”. In: *Phys. Rev. Lett.* 83 (5 1999), pp. 1034–1037. DOI: 10.1103/PhysRevLett.83.1034. URL: <http://link.aps.org/doi/10.1103/PhysRevLett.83.1034>.
- [105] Sergey Pankov. “Low-Temperature Solution of the Sherrington-Kirkpatrick Model”. In: *Phys. Rev. Lett.* 96 (19 2006), p. 197204. DOI: 10.1103/PhysRevLett.96.197204. URL: <http://link.aps.org/doi/10.1103/PhysRevLett.96.197204>.
- [106] H. Horner. “Time dependent local field distribution and metastable states in the SK-spin-glass”. In: *Eur. Phys. Jour. B* 60 (4 2007), pp. 413–422. URL: <http://dx.doi.org/10.1140/epjb/e2008-00017-1>.
- [107] Pierre Le Doussal, Markus Müller, and Kay Jörg Wiese. “Equilibrium avalanches in spin glasses”. In: *Phys. Rev. B* 85 (21 2012), p. 214402. DOI: 10.1103/PhysRevB.85.214402. URL: <http://link.aps.org/doi/10.1103/PhysRevB.85.214402>.
- [108] Matthieu Wyart. “Marginal Stability Constrains Force and Pair Distributions at Random Close Packing”. In: *Phys. Rev. Lett.* 109 (12 2012), p. 125502. DOI: 10.1103/PhysRevLett.109.125502.

- [109] Edan Lerner, Gustavo During, and Matthieu Wyart. “Low-energy non-linear excitations in sphere packings”. In: *Soft Matter* 9 (34 2013), pp. 8252–8263. DOI: 10.1039/C3SM50515D.
- [110] E. Lerner, G. Düring, and M. Wyart. “Toward a microscopic description of flow near the jamming threshold”. In: *EPL (Europhysics Letters)* 99.5 (2012), p. 58003.
- [111] Patrick Charbonneau et al. “Jamming Criticality Revealed by Removing Localized Buckling Excitations”. In: *Physical Review Letters* 114.12 (2015), p. 125504.
- [112] J. Massey and Mark Lee. “Direct Observation of the Coulomb Correlation Gap in a Nonmetallic Semiconductor, Si: B”. In: *Phys. Rev. Lett.* 75 (23 1995), pp. 4266–4269. DOI: 10.1103/PhysRevLett.75.4266. URL: <http://link.aps.org/doi/10.1103/PhysRevLett.75.4266>.
- [113] R G Palmer and C M Pond. “Internal field distributions in model spin glasses”. In: *Journal of Physics F: Metal Physics* 9.7 (1979), p. 1451. URL: <http://stacks.iop.org/0305-4608/9/i=7/a=024>.
- [114] P. W. Anderson. *Ill-Condensed Matter*. Ed. by R. Balian, R. Maynard, and G. Toulouse. p. 159. North-Holland, Amsterdam, 1979.
- [115] Patrick Charbonneau et al. “Fractal free energy landscapes in structural glasses”. In: *Nature communications* 5.3725 (2014).
- [116] Le Yan, Gustavo Düring, and Matthieu Wyart. “Why glass elasticity affects the thermodynamics and fragility of supercooled liquids”. In: *Proceedings of the National Academy of Sciences* 110.16 (2013), pp. 6307–6312.

- [117] Le Yan and Matthieu Wyart. “Evolution of Covalent Networks under Cooling: Contrasting the Rigidity Window and Jamming Scenarios”. In: *Phys. Rev. Lett.* 113 (21 2014), p. 215504. DOI: [10.1103/PhysRevLett.113.215504](https://doi.org/10.1103/PhysRevLett.113.215504). URL: <http://link.aps.org/doi/10.1103/PhysRevLett.113.215504>.
- [118] Le Yan and Matthieu Wyart. “Adaptive Elastic Networks as models of supercooled liquids”. In: *arXiv: 1506.04848* (2015).
- [119] Le Yan, Antoine Barizien, and Matthieu Wyart. “A model for the erosion onset of a granular bed sheared by a viscous fluid”. In: *arXiv:1505.03029* (2015).
- [120] Le Yan et al. “Dynamics and Correlations among Soft Excitations in Marginally Stable Glasses”. In: *arXiv preprint arXiv:1501.03017* (2015).
- [121] Gerold Adam and Julian H. Gibbs. “On the Temperature Dependence of Cooperative Relaxation Properties in Glass-Forming Liquids”. In: *The Journal of Chemical Physics* 43.1 (1965), pp. 139–146. DOI: <http://dx.doi.org/10.1063/1.1696442>. URL: <http://scitation.aip.org/content/aip/journal/jcp/43/1/10.1063/1.1696442>.
- [122] Hiroshi Shintani and Hajime Tanaka. “Universal link between the boson peak and transverse phonons in glass”. In: *Nat Mater* 7 (11 2008), pp. 870–877. DOI: <http://dx.doi.org/10.1038/nmat2293>. URL: http://www.nature.com/nmat/journal/v7/n11/supinfo/nmat2293_S1.html.
- [123] A.C. Anderson. *Amorphous Solids: Low Temperature Properties*. Ed. by W. A. Phillips. Vol. 24. Topics in Current Physics. Springer, Berlin, 1981.

- [124] Kaori Ito, Cornelius Moynihan, and C. Austen Angell. “Thermodynamic determination of fragility in liquids and a fragile-to-strong liquid transition in water”. In: *Nature* 398 (1999), p. 492.
- [125] W. A. Kamitakahara et al. “Vibrational densities of states and network rigidity in chalcogenide glasses”. In: *Phys. Rev. B* 44 (1 1991), pp. 94–100. DOI: 10.1103/PhysRevB.44.94. URL: <http://link.aps.org/doi/10.1103/PhysRevB.44.94>.
- [126] Carolina Brito et al. “Elementary excitation modes in a granular glass above jamming”. In: *Soft Matter* 6.13 (2010), pp. 3013–3022.
- [127] M Wyart, SR Nagel, and TA Witten. “Geometric origin of excess low-frequency vibrational modes in weakly connected amorphous solids”. In: *EPL (Europhysics Letters)* 72.3 (2005), pp. 486–492.
- [128] M. Wyart. “On the Rigidity of Amorphous Solids”. In: *Annales de Phys* 30.3 (2005), pp. 1–113.
- [129] Ning Xu et al. “Excess vibrational modes and the boson peak in model glasses”. In: *Physical review letters* 98.17 (2007), p. 175502.
- [130] M. Wyart et al. “Elasticity of Floppy and Stiff Random Networks”. In: *Phys. Rev. Lett.* 101 (2008), p. 215501.
- [131] W. G. Ellenbroek et al. “Non-affine response: Jammed packings vs. spring networks”. In: *EPL* 87 (3 2009), p. 34004. DOI: 10.1209/0295-5075/87/34004.
- [132] Matthieu Wyart. “Scaling of phononic transport with connectivity in amorphous solids”. In: *EPL (Europhysics Letters)* 89.6 (2010), p. 64001.

- [133] John J Hopfield. “Neural networks and physical systems with emergent collective computational abilities”. In: *Proceedings of the national academy of sciences* 79.8 (1982), pp. 2554–2558.
- [134] Brian Hayes. “Computing science: The easiest hard problem”. In: *American Scientist* (2002), pp. 113–117.
- [135] Stephan Mertens. “A physicist’s approach to number partitioning”. In: *Theoretical Computer Science* 265.1 (2001), pp. 79–108.
- [136] Bernard Derrida. “Random-energy model: An exactly solvable model of disordered systems”. In: *Phys. Rev. B* 24 (5 1981), pp. 2613–2626. DOI: 10.1103/PhysRevB.24.2613. URL: <http://link.aps.org/doi/10.1103/PhysRevB.24.2613>.
- [137] R. Cherrier, D. S. Dean, and A. Lefèvre. “Role of the interaction matrix in mean-field spin glass models”. In: *Phys. Rev. E* 67 (4 2003), p. 046112. DOI: 10.1103/PhysRevE.67.046112. URL: <http://link.aps.org/doi/10.1103/PhysRevE.67.046112>.
- [138] F. Caltagirone et al. “Critical Slowing Down Exponents of Mode Coupling Theory”. In: *Phys. Rev. Lett.* 108 (8 2012), p. 085702. DOI: 10.1103/PhysRevLett.108.085702. URL: <http://link.aps.org/doi/10.1103/PhysRevLett.108.085702>.
- [139] Ludovic Berthier and Gilles Tarjus. “Nonperturbative Effect of Attractive Forces in Viscous Liquids”. In: *Phys. Rev. Lett.* 103 (17 2009), p. 170601. DOI: 10.1103/PhysRevLett.103.170601. URL: <http://link.aps.org/doi/10.1103/PhysRevLett.103.170601>.

- [140] Chiara Cammarota et al. “On the fragility of the mean-field scenario of structural glasses for finite-dimensional disordered spin models”. In: *arXiv preprint arXiv:1210.2941* (2012).
- [141] Asaph Widmer-Cooper et al. “Irreversible reorganization in a supercooled liquid originates from localized soft modes”. In: *Nature Physics* 4.9 (2008), pp. 711–715.
- [142] A.S Argon. “Plastic deformation in metallic glasses”. In: *Acta Metallurgica* 27.1 (1979), pp. 47–58. ISSN: 0001-6160. DOI: 10.1016/0001-6160(79)90055-5. URL: <http://www.sciencedirect.com/science/article/pii/0001616079900555>.
- [143] M. L. Falk and J. S. Langer. “Dynamics of viscoplastic deformation in amorphous solids”. In: *Phys. Rev. E* 57 (1998), p. 7192.
- [144] H.M. Jaeger, S.R. Nagel, and R.P. Behringer. “Granular solids, liquids, and gases”. In: *Rev. Mod. Phys.* 68 (1996), pp. 1259–73.
- [145] Fabien Leonforte et al. “Inhomogeneous elastic response of silica glass”. In: *Physical review letters* 97.5 (2006), p. 055501.
- [146] Edan Lerner et al. “Breakdown of continuum elasticity in amorphous solids”. In: *Soft Matter* 10 (2014), pp. 5085–5092.
- [147] Wouter G Ellenbroek, Martin van Hecke, and Wim van Saarloos. “Jammed frictionless disks: Connecting local and global response”. In: *Physical Review E* 80.6 (2009), p. 061307.
- [148] L. E. Silbert, A. J. Liu, and S. R. Nagel. “Vibrations and Diverging Length Scales Near the Unjamming Transition”. In: *Phys. Rev. Lett.* 95 (2005), p. 098301.

- [149] Matthieu Wyart. “Correlations between Vibrational Entropy and Dynamics in Liquids”. In: *Phys. Rev. Lett.* 104 (2010), p. 095901.
- [150] Eric DeGiuli et al. “Effects of coordination and pressure on sound attenuation, boson peak and elasticity in amorphous solids”. In: *Soft Matter* 10.30 (2014), pp. 5628–5644.
- [151] Jorge Kurchan et al. “Exact theory of dense amorphous hard spheres in high dimension. II. The high density regime and the Gardner transition”. In: *The Journal of Physical Chemistry B* 117.42 (2013), pp. 12979–12994.
- [152] M.F. Thorpe. “Rigidity percolation in glassy structures”. In: *Journal of Non-Crystalline Solids* 76.1 (1985), pp. 109 –116. ISSN: 0022-3093. DOI: [http://dx.doi.org/10.1016/0022-3093\(85\)90056-0](http://dx.doi.org/10.1016/0022-3093(85)90056-0).
- [153] M. Bauchy and M. Micoulaut. “Transport Anomalies and Adaptive Pressure-Dependent Topological Constraints in Tetrahedral Liquids: Evidence for a Reversibility Window Analogue”. In: *Phys. Rev. Lett.* 110 (9 2013), p. 095501. DOI: 10.1103/PhysRevLett.110.095501. URL: <http://link.aps.org/doi/10.1103/PhysRevLett.110.095501>.
- [154] Matthieu Micoulaut and Mathieu Bauchy. “Anomalies of the first sharp diffraction peak in network glasses: Evidence for correlations with dynamic and rigidity properties”. In: *physica status solidi (b)* 250.5 (2013), pp. 976–982. ISSN: 1521-3951. DOI: 10.1002/pssb.201248512. URL: <http://dx.doi.org/10.1002/pssb.201248512>.
- [155] Cristian F. Moukarzel. “Two rigidity-percolation transitions on binary Bethe networks and the intermediate phase in glass”. In: *Phys. Rev. E* 88 (6 2013),

- p. 062121. DOI: 10.1103/PhysRevE.88.062121. URL: <http://link.aps.org/doi/10.1103/PhysRevE.88.062121>.
- [156] D. J. Jacobs and M. F. Thorpe. “Comment on “Infinite-Cluster Geometry in Central-Force Networks””. In: *Phys. Rev. Lett.* 80 (24 1998), pp. 5451–5451. DOI: 10.1103/PhysRevLett.80.5451. URL: <http://link.aps.org/doi/10.1103/PhysRevLett.80.5451>.
- [157] P. M. Duxbury et al. “Floppy modes and the free energy: Rigidity and connectivity percolation on Bethe lattices”. In: *Phys. Rev. E* 59 (2 1999), pp. 2084–2092. DOI: 10.1103/PhysRevE.59.2084. URL: <http://link.aps.org/doi/10.1103/PhysRevE.59.2084>.
- [158] Shechao Feng. “Crossover in spectral dimensionality of elastic percolation systems”. In: *Phys. Rev. B* 32 (9 1985), pp. 5793–5797. DOI: 10.1103/PhysRevB.32.5793. URL: <http://link.aps.org/doi/10.1103/PhysRevB.32.5793>.
- [159] Tsuneyoshi Nakayama, Kousuke Yakubo, and Raymond L. Orbach. “Dynamical properties of fractal networks: Scaling, numerical simulations, and physical realizations”. In: *Rev. Mod. Phys.* 66 (2 1994), pp. 381–443. DOI: 10.1103/RevModPhys.66.381. URL: <http://link.aps.org/doi/10.1103/RevModPhys.66.381>.
- [160] M.-A. Brière, M. V. Chubynsky, and Normand Mousseau. “Self-organized criticality in the intermediate phase of rigidity percolation”. In: *Phys. Rev. E* 75 (5 2007), p. 056108. DOI: 10.1103/PhysRevE.75.056108. URL: <http://link.aps.org/doi/10.1103/PhysRevE.75.056108>.

- [161] Matthieu Micoulaut and James C. Phillips. “Rings and rigidity transitions in network glasses”. In: *Phys. Rev. B* 67 (10 2003), p. 104204. DOI: 10.1103/PhysRevB.67.104204. URL: <http://link.aps.org/doi/10.1103/PhysRevB.67.104204>.
- [162] J. Barré et al. “Adaptability and “Intermediate Phase” in Randomly Connected Networks”. In: *Phys. Rev. Lett.* 94 (20 2005), p. 208701. DOI: 10.1103/PhysRevLett.94.208701. URL: <http://link.aps.org/doi/10.1103/PhysRevLett.94.208701>.
- [163] Donald J. Jacobs and Bruce Hendrickson. “An Algorithm for Two-Dimensional Rigidity Percolation: The Pebble Game”. In: *Journal of Computational Physics* 137.2 (1997), pp. 346–365. ISSN: 0021-9991. DOI: <http://dx.doi.org/10.1006/jcph.1997.5809>. URL: <http://www.sciencedirect.com/science/article/pii/S0021999197958095>.
- [164] Ed by John L. Cardy. *Theory of Finite-Size Scaling*. Ed. by H. Rubenstein. Vol. 2 Finite Size Scaling. Current Physics - Sources and Comments. Elsevier Science Publishers B.V., 1988, pp. 1–182.
- [165] D. J. Jacobs and M. F. Thorpe. “Generic rigidity percolation in two dimensions”. In: *Phys. Rev. E* 53 (4 1996), pp. 3682–3693. DOI: 10.1103/PhysRevE.53.3682. URL: <http://link.aps.org/doi/10.1103/PhysRevE.53.3682>.
- [166] Chase P. Broedersz et al. “Criticality and isostaticity in fibre networks”. In: *Nat Phys* 7 (12 2011), pp. 983–988. URL: <http://dx.doi.org/10.1038/nphys2127>.

- [167] M. V. Chubynsky. “Rigidity and self-organization of random networks”. In: *Thesis* (2003).
- [168] M. V. Chubynsky and M. F. Thorpe. “Algorithms for three-dimensional rigidity analysis and a first-order percolation transition”. In: *Phys. Rev. E* 76 (4 2007), p. 041135. DOI: 10.1103/PhysRevE.76.041135. URL: <http://link.aps.org/doi/10.1103/PhysRevE.76.041135>.
- [169] Frank H Stillinger and Thomas A Weber. “Packing structures and transitions in liquids and solids”. In: *Science(Washington, DC)* 225.4666 (1984), pp. 983–9.
- [170] R. V. Chamberlin. “Mesoscopic Mean-Field Theory for Supercooled Liquids and the Glass Transition”. In: *Phys. Rev. Lett.* 82 (12 1999), pp. 2520–2523. DOI: 10.1103/PhysRevLett.82.2520. URL: <http://link.aps.org/doi/10.1103/PhysRevLett.82.2520>.
- [171] Jeppe C Dyre. “Colloquium: The glass transition and elastic models of glass-forming liquids”. In: *Reviews of modern physics* 78.3 (2006), pp. 953–972.
- [172] David Chandler and Juan P. Garrahan. “Dynamics on the Way to Forming Glass: Bubbles in Space-Time”. In: *Annual Review of Physical Chemistry* 61.1 (2010). PMID: 20055676, pp. 191–217. DOI: 10.1146/annurev.physchem.040808.090405. eprint: <http://dx.doi.org/10.1146/annurev.physchem.040808.090405>. URL: <http://dx.doi.org/10.1146/annurev.physchem.040808.090405>.

- [173] Vanessa K. de Souza and Peter Harrowell. “Rigidity percolation and the spatial heterogeneity of soft modes in disordered materials”. In: *Proceedings of the National Academy of Sciences* 106.36 (2009), pp. 15136–15141.
- [174] Pyotr Rabochiy and Vassiliy Lubchenko. “Microscopic calculation of the free energy cost for activated transport in glass-forming liquids”. In: *The Journal of chemical physics* 138.12 (2013), 12A534.
- [175] M. Micoulaut and P. Boolchand. “Comment on “Microscopic Theory of Network Glasses””. In: *Phys. Rev. Lett.* 91 (15 2003), p. 159601. DOI: 10.1103/PhysRevLett.91.159601. URL: <http://link.aps.org/doi/10.1103/PhysRevLett.91.159601>.
- [176] Vanessa K. de Souza and Peter Harrowell. “Unconstrained motions, dynamic heterogeneities, and relaxation in disordered solids”. In: *Phys. Rev. E* 80 (4 2009), p. 041503. DOI: 10.1103/PhysRevE.80.041503. URL: <http://link.aps.org/doi/10.1103/PhysRevE.80.041503>.
- [177] Wouter G. Ellenbroek et al. “Rigidity Loss in Disordered Systems: Three Scenarios”. In: *Phys. Rev. Lett.* 114 (13 2015), p. 135501. DOI: 10.1103/PhysRevLett.114.135501. URL: <http://link.aps.org/doi/10.1103/PhysRevLett.114.135501>.
- [178] J. Barré. “Hierarchical models of rigidity percolation”. In: *Phys. Rev. E* 80 (6 2009), p. 061108. DOI: 10.1103/PhysRevE.80.061108. URL: <http://link.aps.org/doi/10.1103/PhysRevE.80.061108>.
- [179] Tomás S. Grigera and Giorgio Parisi. “Fast Monte Carlo algorithm for supercooled soft spheres”. In: *Phys. Rev. E* 63 (4 2001), p. 045102. DOI:

- 10.1103/PhysRevE.63.045102. URL: <http://link.aps.org/doi/10.1103/PhysRevE.63.045102>.
- [180] FA Lindemann. In: *Z. Phys.* 11 (1910), p. 609.
- [181] David R Nelson. *Defects and geometry in condensed matter physics*. Cambridge University Press, 2002.
- [182] Marc and Mézard. *Information, Physics and Computation*. Oxford University press, 2009.
- [183] François Charru, Bruno Andreotti, and Philippe Claudin. “Sand ripples and dunes”. In: *Annual Review of Fluid Mechanics* 45 (2013), pp. 469–493.
- [184] C. h. Liu et al. “Force Fluctuations in Bead Packs”. In: *Science* 269.5223 (1995), pp. 513–515. DOI: 10.1126/science.269.5223.513. URL: <http://www.sciencemag.org/content/269/5223/513.abstract>.
- [185] S. N. Coppersmith et al. “Model for force fluctuations in bead packs”. In: *Phys. Rev. E* 53 (5 1996), pp. 4673–4685. DOI: 10.1103/PhysRevE.53.4673. URL: <http://link.aps.org/doi/10.1103/PhysRevE.53.4673>.
- [186] Onuttom Narayan and Daniel S. Fisher. “Nonlinear fluid flow in random media: Critical phenomena near threshold”. In: *Phys. Rev. B* 49 (14 1994), pp. 9469–9502. DOI: 10.1103/PhysRevB.49.9469. URL: <http://link.aps.org/doi/10.1103/PhysRevB.49.9469>.
- [187] Alejandro B. Kolton, Daniel Domínguez, and Niels Grønbech-Jensen. “Hall Noise and Transverse Freezing in Driven Vortex Lattices”. In: *Phys. Rev. Lett.* 83 (15 1999), pp. 3061–3064. DOI: 10.1103/PhysRevLett.83.3061. URL: <http://link.aps.org/doi/10.1103/PhysRevLett.83.3061>.

- [188] C Reichhardt and CJ Olson. “Colloidal dynamics on disordered substrates”. In: *Physical review letters* 89.7 (2002), p. 078301.
- [189] Alexandros Pertsinidis and Xinsheng Sean Ling. “Statics and dynamics of 2D colloidal crystals in a random pinning potential”. In: *Physical review letters* 100.2 (2008), p. 028303.
- [190] Bruno Andreotti, Yoël Forterre, and Olivier Pouliquen. *Granular media: between fluid and solid*. Cambridge University Press, 2013.
- [191] Malika Ouriemi et al. “Determination of the critical Shields number for particle erosion in laminar flow”. In: *Physics of Fluids* 19.6 (2007), pp. 61706–63100.
- [192] M. Müller and L. Ioffe. “Glass Transition and the Coulomb Gap in Electron Glasses”. In: *Phys. Rev. Lett.* 93 (25 2004), p. 256403. DOI: 10.1103/PhysRevLett.93.256403. URL: <http://link.aps.org/doi/10.1103/PhysRevLett.93.256403>.
- [193] M. Müller and S. Pankov. “Mean-field theory for the three-dimensional Coulomb glass”. In: *Phys. Rev. B* 75 (14 2007), p. 144201. DOI: 10.1103/PhysRevB.75.144201. URL: <http://link.aps.org/doi/10.1103/PhysRevB.75.144201>.
- [194] Matteo Palassini and Martin Goethe. “Elementary excitations and avalanches in the Coulomb glass”. In: *Journal of Physics: Conference Series* 376.1 (2012), p. 012009. URL: <http://stacks.iop.org/1742-6596/376/i=1/a=012009>.
- [195] Juan Carlos Andresen et al. “Charge avalanches in the Coulomb glass: the role of long-range interactions”. In: *arXiv: 1309.2887* (2013).

- [196] DJ Thouless, PW Anderson, and RG Palmer. “SOLUTION OF SOLVABLE MODEL OF A SPIN GLASS”. In: *Philo. Mag.* 35 (3 1977), pp. 593–601. DOI: 10.1080/14786437708235992. URL: <http://link.aps.org/doi/10.1103/PhysRevLett.59.381>.
- [197] P. R. Eastham et al. “Mechanism for the failure of the Edwards hypothesis in the Sherrington-Kirkpatrick spin glass”. In: *Phys. Rev. B* 74 (2 2006), p. 020406. DOI: 10.1103/PhysRevB.74.020406. URL: <http://link.aps.org/doi/10.1103/PhysRevB.74.020406>.
- [198] Juan Andresen et al. “Self-Organized Criticality in Glassy Spin Systems Requires a Diverging Number of Neighbors”. In: *Phys. Rev. Lett.* 111 (9 2013), p. 097203. DOI: 10.1103/PhysRevLett.111.097203. URL: <http://link.aps.org/doi/10.1103/PhysRevLett.111.097203>.
- [199] M. Mezard, G. Parisi, and M. A. Virasoro. *Spin glass theory and beyond*. World Scientific, 1987.
- [200] Patrick Charbonneau et al. “Exact theory of dense amorphous hard spheres in high dimension. III. The full replica symmetry breaking solution”. In: *Journal of Statistical Mechanics: Theory and Experiment* 2014.10 (2014), p. 10009.
- [201] E DeGiuli et al. “Unified Theory of Inertial Granular Flows and Non-Brownian Suspensions”. In: *arXiv preprint arXiv:1410.3535* (2014).
- [202] JP Sethna, KA Dahmen, and CR Myers. “Crackling noise”. In: *Nature* 410 (2001), pp. 242–250.

- [203] Gaël Combe and Jean-Noël Roux. “Strain versus stress in a model granular material: a Devil’s staircase”. In: *Physical Review Letters* 85.17 (2000), p. 3628.
- [204] Péter Dusán Ispánovity et al. “Avalanches in 2D Dislocation Systems: Plastic Yielding Is Not Depinning”. In: *Physical review letters* 112.23 (2014), p. 235501.
- [205] Deepak Dhar, Prabodh Shukla, and James P Sethna. “Zero-temperature hysteresis in the random-field Ising model on a Bethe lattice”. In: *Journal of Physics A: Mathematical and General* 30.15 (1997), p. 5259. URL: <http://stacks.iop.org/0305-4470/30/i=15/a=013>.
- [206] Sanjib Sabhapandit, Deepak Dhar, and Prabodh Shukla. “Hysteresis in the Random-Field Ising Model and Bootstrap Percolation”. In: *Phys. Rev. Lett.* 88 (19 2002), p. 197202. DOI: 10.1103/PhysRevLett.88.197202. URL: <http://link.aps.org/doi/10.1103/PhysRevLett.88.197202>.
- [207] S. Boettcher. “Extremal optimization for Sherrington-Kirkpatrick spin glasses”. In: *Eur. Phys. J. B* 46.4 (2005), pp. 501–505. DOI: 10.1140/epjb/e2005-00280-6. URL: <http://dx.doi.org/10.1140/epjb/e2005-00280-6>.
- [208] Károly F. Pál. “Hysteretic optimization for the Sherrington–Kirkpatrick spin glass”. In: *Physica A: Statistical Mechanics and its Applications* 367 (2006), pp. 261–268.
- [209] Giorgio Parisi. “On the origin of the boson peak”. In: *Journal of Physics: Condensed Matter* 15.11 (2003), S765.
- [210] Sidney Redner. *A Guide to First-Passage Processes*. Cambridge University Press, 2001.

- [211] Alan J. Bray, Satya N. Majumdar, and Grégory Schehr. “Persistence and first-passage properties in nonequilibrium systems”. In: *Advances in Physics* 62.3 (2013), pp. 225–361. DOI: 10.1080/00018732.2013.803819.
- [212] P Boolchand, DG Georgiev, and B Goodman. “Discovery of the intermediate phase in chalcogenide glasses”. In: *Journal of Optoelectronics and Advanced Materials* 3.3 (2001), pp. 703–720.
- [213] Yufeng Wang et al. “Colloids with valence and specific directional bonding”. In: *Nature* 491.7422 (2012), pp. 51–55.
- [214] AA Abrikosov. “Nobel Lecture: Type-II superconductors and the vortex lattice”. In: *Reviews of modern physics* 76.3 (2004), p. 975.
- [215] Niels Grønbech-Jensen, A. R. Bishop, and Daniel Domínguez. “Metastable Filamentary Vortex Flow in Thin Film Superconductors”. In: *Phys. Rev. Lett.* 76 (16 1996), pp. 2985–2988. DOI: 10.1103/PhysRevLett.76.2985. URL: <http://link.aps.org/doi/10.1103/PhysRevLett.76.2985>.
- [216] Daniel Domínguez. “Dynamic Transition in Vortex Flow in Strongly Disordered Josephson Junction Arrays and Superconducting Thin Films”. In: *Phys. Rev. Lett.* 82 (1 1999), pp. 181–184. DOI: 10.1103/PhysRevLett.82.181. URL: <http://link.aps.org/doi/10.1103/PhysRevLett.82.181>.
- [217] Alejandro B. Kolton and Daniel Domínguez. “Nonequilibrium Structures and Dynamic Transitions in Driven Vortex Lattices with Disorder”. In: *AIP Conference Proceedings* 658.1 (2003), pp. 383–391. DOI: <http://dx.doi.org/10.1063/1.1566665>. URL: <http://scitation.aip.org/content/aip/proceeding/aipcp/10.1063/1.1566665>.

- [218] E. Olive and J. C. Soret. “Chaotic Dynamics of Superconductor Vortices in the Plastic Phase”. In: *Phys. Rev. Lett.* 96 (2 2006), p. 027002. DOI: 10.1103/PhysRevLett.96.027002. URL: <http://link.aps.org/doi/10.1103/PhysRevLett.96.027002>.
- [219] A. E. Koshelev and V. M. Vinokur. “Dynamic Melting of the Vortex Lattice”. In: *Phys. Rev. Lett.* 73 (26 1994), pp. 3580–3583. DOI: 10.1103/PhysRevLett.73.3580. URL: <http://link.aps.org/doi/10.1103/PhysRevLett.73.3580>.
- [220] Antoine Barizien and Matthieu Wyart. “Études du comportement d’un lit de sédiment soumis à l’action d’un fluide”. MA thesis. École Polytechnique, 2014.
- [221] Alejandro B. Kolton et al. “Creep dynamics of elastic manifolds via exact transition pathways”. In: *Phys. Rev. B* 79 (18 2009), p. 184207. DOI: 10.1103/PhysRevB.79.184207. URL: <http://link.aps.org/doi/10.1103/PhysRevB.79.184207>.
- [222] Pierluigi Contucci et al. “Interpolating greedy and reluctant algorithms”. In: *Optimization Methods and Software* 20.4-5 (2005), pp. 509–514.
- [223] EA Jagla. “Avalanche size distributions in mean field plastic yielding models”. In: *arXiv preprint arXiv:1506.01005* (2015).
- [224] S. Alexander and R. Orbach. “Density of states on fractals: $\zeta(\nu)$ ”. In: *J. Phys. (Paris) Lett.* 43 (17 1982), pp. 625–631. DOI: 10.1051/jphyslet:019820043017062500. URL: <http://dx.doi.org/10.1051/jphyslet:019820043017062500>.

- [225] H. Risken, ed. *The Fokker-Planck equation: Methods of solution and applications*. Springer, 1996.